Investigations of Structural, Optical, Electronic, and Magnetic Properties of Rare-earth Orthoferrites

Ph.D. Thesis

By

Mohammed Kamal Warshi

DISCIPLINE OF PHYSICS

INDIAN INSTITUTE OF TECHNOLOGY INDORE

December 2018

Investigations of Structural, Optical, Electronic, and Magnetic Properties of Rare-earth Orthoferrites

A THESIS

Submitted in partial fulfillment of the
requirements for the award of the degree
of
DOCTOR OF PHILOSOPHY

by
Mohammed Kamal Warshi

DISCIPLINE OF PHYSICS
INDIAN INSTITUTE OF TECHNOLOGY INDORE
December 2018

INDIAN INSTITUTE OF TECHNOLOGY INDORE

CANDIDATE’S DECLARATION

I hereby certify that the work which is being presented in the thesis entitled **Investigations of Structural, Optical, Electronic, and Magnetic Properties of Rare-earth Orthoferrites** in the partial fulfillment of the requirements for the award of the degree of **Doctor of Philosophy** and submitted in the **Discipline of Physics, Indian Institute of Technology Indore**, is an authentic record of my own work carried out during the time period from July 2014 to December 2018 under the supervision of Dr. Pankaj R. Sagdeo, Associate Professor, Indian Institute of Technology Indore and Dr. Rajesh Kumar, Associate Professor, Designation, Indian Institute of Technology Indore.

The matter presented in this thesis has not been submitted by me for the award of any other degree of this or any other institute.

Signature of the student with date
(Mohammed Kamal Warshi)

This is to certify that the above statement made by the candidate is correct to the best of my/our knowledge.

Signature of Thesis Supervisor #1 with date	Signature of Thesis Supervisor #2 with date
(Dr. Pankaj R Sagdeo)	**(Dr. Rajesh Kumar)**

Mohammed Kamal Warshi has successfully given his/her Ph.D. Oral Examination held on **10th April 2019**.

Signature of Chairperson (OEB) Date:	Signature of External Examiner Date:	Signature(s) of Thesis Supervisor(s) Date:
Signature of PSPC Member #1 Date:	Signature of PSPC Member #2 Date:	Signature of Convener, DPGC Date:
Signature of Head of Discipline Date:		

Acknowledgments

During the last four and a half years, I am privileged to have had many people who helped in the research providing academic, teaching, and moral support to make this thesis possible. I hereby thank all of them.

I would like to express my deepest gratitude to my supervisor Dr. Pankaj R Sagdeo for giving me the possibility to perform this work under his guidance and learning opportunities during this work. His constant scientific and personal guidance, support and motivation were essential for the success of this thesis. I will be forever grateful to him for helping me to achieve this goal.

Thanking Dr. Rajesh Kumar cannot be enough. His fantastic co-supervision was a keystone for this work. His constructive input, patience, availability for discussions were of great importance and help to me.

I would sincerely like to thank Dr. Sudeshna Chattopadhyay and Dr. Satya S. Bulusu for being a member of the progress evaluation committee (PSPC). Their evaluation, comments, and suggestion help me a lot to improve my research work.

I would like to express my gratitude to Prof. Pradeep Mathur. He always goes out of the way to help students of IIT Indore. His energy and enthusiasm for research always motivated me.

I was fortunate to collaborate with various external groups during the research work. I would like to express my deepest thank to

- *Dr. Vinayak Mishra, Computational Analysis Division, Bhabha Atomic Research Centre, Visakhapatnam, India, for providing an opportunity to spent time his laboratory and learn first principle calculation from the very initial stage. I highly appreciate the help with theoretical calculations and data analysis with WIEN2k package and discussion with him.*
- *Dr. Archna Sagdeo, Indus Synchrotron Utilization Division, Raja Ramanna Centre for Advanced Technology Indore, India for her*

help during synchrotron x-ray diffraction measurements on beamline 12 and for continuous and fruitful discussion x-ray diffraction overall time of the thesis work.

I would like to thank all members of the Discipline of Physics, particularly the entire group of Materials Research Laboratory for making their assistance during work and making the duration of my PhD such a great experience. I am very grateful to Mr. Vikash Mishra, Mr. Anil Kumar, and Miss Aanchal Sati for making environment working friendly in the lab.

I sincerely thank Sophisticated Instrumentation Center, IIT Indore, most specifically Mr. Nitin Upadhya and Mr. Kinny Pandey for their support during XRD and SEM measurements respectively.

I would like to thank Mr. Yogendra for providing technical support required during installation of WIEN2k package.

I sincerely want to thank all staff members of IIT Indore for providing all comfort and convenience.

Besides this, I would like to thank several people who have knowingly and unknowingly helped me in the successful completion of my thesis.

I would like to thank sincerely my elder brother Mohammed Jamal Warsi for his constant motivation and support throughout the thesis work.

Last but not least, I would like to thank my parents for their constant support and all the sacrifices they have made until the submission of the thesis.

I grateful for financial support from IIT Indore and Ministry of Human Resources Development, Government of India.

Mohammed Kamal Warshi

List of Publications

List of publications from Ph. D. thesis work

1. **M. Kamal Warshi,** V. Mishra, A. Sagdeo, V. Mishra, R. Kumar, P.R. Sagdeo; *Structural, optical and electronic properties of RFeO3,* **Ceramics International**, 44 (2018) 8344-8349. (**Impact Factor: 3.057**)
2. **M. Kamal Warshi,** V. Mishra, V. Mishra, R. Kumar, P.R. Sagdeo; *Possible origin of ferromagnetism in antiferromagnetic orthorhombic-YFeO3: A first-principles study*, **Ceramics International**, 44 (2018) 13507-13512. (**Impact Factor: 3.057**)
3. **M. Kamal Warshi,** V. Mishra, A. Sagdeo, V. Mishra, R. Kumar, P.R. Sagdeo; *Synthesis and characterization of RFeO3: experimental results and theoretical prediction*, **Advances in Materials and Processing Technologies**, (2018) 1-15. (**Impact Factor: Not available**)
4. ***M Kamal Warshi et al.,*** Possible Origin of d-d Transitions in RFeO$_3$ (3d^5) Systems: Experiments and Theory. **(Under Review)**
5. ***M Kamal Warshi et al.,*** Design and Development of a Low-Cost and fully Automated Experimental Setup for Temperature dependent Magneto-dielectric Measurements. **(Under Review)**

List of other publications during Ph. D.

6. A Kumar, **M. Kamal Warshi,** V. Mishra, S.K. Saxena, R. Kumar, P.R. Sagdeo; *Strain control of Urbach energy in Cr-doped PrFeO$_3$*, **Applied Physics A**, 123 (2017) 576. (**Impact Factor: 1.604**)
7. V. Mishra, **M. Kamal Warshi**, Aanchal Sati, Anil Kumar, V. Mishra, Archna Sagdeo, R. Kumar, and P. R. Sagdeo; *Diffuse Reflectance Spectroscopy: An Effective Tool to Probe the Defect States in Wide Bandgap Semiconducting Materials;* **Mater. Sci. Semicond. Process**, 86 (2018), 151-156. (**Impact Factor: 2.593**)

8. V. Mishra, **M. Kamal Warshi,** R. Kumar, and P.R. Sagdeo, *Design and Development of In-Situ Temperature Dependent Diffuse Reflectance Spectroscopy setup*; **J. Inst., 13(2018), T11003.** (**Impact Factor: 1.258**)
9. H. M. Rai, P. Singh, S. K. Saxena, V. Mishra, **M. Kamal Warshi**, R. Kumar, P. Rajput, A. Sagdeo, I. Choudhuri, B. Pathak, P.R. Sagdeo; *Room-Temperature Magneto-dielectric Effect in* $LaGa_{0.7}Fe_{0.3}O_{3+\gamma}$*; Origin and Impact of Excess Oxygen*, ***Inorganic Chemistry***, 56 (2017) 3809-3819. (**Impact Factor: 4.7**)
10. V. Mishra, A. Sagdeo, V. Kumar, **M. Kamal Warshi**, H.M. Rai, S.K. Saxena, D. R. Roy, V. Mishra, R. Kumar, P. R. Sagdeo; *Electronic and optical properties of* $BaTiO_3$ *across tetragonal to cubic phase transition: An experimental and theoretical investigation*, **Journal of Applied Physics**, 122 (2017) 065105. (**Impact Factor: 2.17**)
11. V. Vikash, S. Aanchal, **M. Kamal Warshi**, B. P. Ambadas, D. Sanjay, V.N. Bhoraskar, G. Harnath, S. Archna, M. Vinayak, K. Rajesh, P.R. Sagdeo; *Effect of electron irradiation on the optical properties of SrTiO 3 : An experimental and theoretical investigations*, **Materials Research Express**, 5 (2018) 036210. (**Impact Factor: 1.15**)

Table of Contents

Chapter 1: Introduction

Chapter 2: Experimental Techniques and Theoretical Background

Chapter 3: Synthesis, Structural, and Thermal Properties of Rare-earth Orthoferrites

Chapter 4: Optical and Electronic Properties of Rare-earth Orthoferrites

Chapter 5: Theoretical Investigations of Structural, Electronic, and Magnetic Properties of Rare-earth Orthoferrites

Chapter 6: Possible Origin of d-d Transitions in RFeO$_3$ (3d^5) Systems: Experiments and Theory

Chapter 7: Conclusion and Future Perspectives

APPENDIX-A: Design and Development of a Fully Automated Experimental Setup for In-situ Temperature Dependent Magneto-Dielectric Measurements

List of Figures

List of Tables

List of Abbreviations

Rare-earth orthoferrites	**$RFeO_3$**
Ruddlesden-Popper phase	**RPP**
Dzyaloshinskii-Moriya	**DM**
Density functional theory	**DFT**
Bond valence sum	**VBS**
X-ray diffraction	**XRD**
Diffuse reflectance spectroscopy	**DRS**
X-ray absorption near edge spectroscopy	**XANES**
Soft x-ray absorption spectroscopy	**SXAS**
Near- neighbour distance	**NND**
Differential scanning calorimetry	**DSC**
X-ray emission spectroscopy	**XES**
X-photoemission spectroscopy	**XPS**
Local density approximation	**LDA**
Generalized gradient approximation	**GGA**
Dynamical mean field theory	**DMFT**
Angle dispersive x-ray diffraction	**ADXRD**
Conduction band minimum	**CBM**
Valence band maximum	**VBM**
Full-potential linearized augmented plane wave	**FP-LAPW**
Antiferromagnetic	**AFM**
Ferromagnetic	**FM**
Neel temperature	**T_N**
Global instability index	**GII**
Density of states	**DOS**
Yttrium iron garnet	**$Y_3Fe_5O_{12}$**
Yttrium orthoferrite	**$YFeO_3$**

Chapter 1

Introduction

In this chapter, a brief review of the literature on rare-earth orthoferrites and its applications in science and technology have been provided. The chapter is concluded with motivation and the questions that the present thesis seeks to answer.

1.1 Introduction

Today's Modern society demands high-performance and multitasking micro-electronic devices which can store and share information in easier and faster ways[1, 2]. This motivates and inspires scientists and industries searching for new, advanced, energy efficient and convenient ways to read, write, store, and sharing of information. One of the major problems of these highly efficient multi-functional devices is the requirement of high power consumption and the increasing need for reducing power consumption in computing and data storage[3, 4]. Thus, an important goal of today's research for our society is the minimization of this energy consumption for the use of multitasking devices. These challenges are intimately related to advances in materials research and technology. All the new product-innovation is based on materials with new and improved properties. Therefore, one approach of the material research community is the engineering of new materials with preferably strongly coupled multi-functional properties with low power consumption for reading, writing and data sharing processes.

In this framework, ABO_3 perovskite-type oxides are a versatile group of materials[5-8]. ABO_3 type structures have the possibility to explore many different elements into the structure with precise control of structural distortions gives rise to a huge variety of properties and coupling phenomena. Particularly interesting for applications in the so-called ferroic properties namely ferromagnetism, ferroelectricity and ferroelasticity which can be tuned by the chemical composition or external parameters such as electric and magnetic fields. Materials which possess more than one ferroic orders are termed as multiferroics. These materials become attractive as they can have intrinsically combined magnetic, ferroelectric, and elastic properties. In multiferroics, the magnetism and the ferroelectricity can occur independently or may have strong coupling between these ferroic orders. This is the case for example in the bismuth ferrite $BiFeO_3$[9], one of the room temperature multiferroic materials with strong polarization. On the other hand, the ferroelectricity can also be induced by canting of magnetic spins or spin chirality[10-12].

Most importantly, these properties depend very much on structural parameters such as octahedra tilts and distortions, various bond lengths, bond angles, and atomic displacements, etc. Therefore, a detailed investigation so that understanding of structural properties is of general importance to understand these properties.

In the present work, an attempt has been made to contribute in the field of multiferroic perovskite $RFeO_3$ in terms of their structural, optical, electronic and magnetic properties. Further, the influence of various site defects (R, Fe and O sites defects) on these properties with a special focus on $YFeO_3$.

Recently, the interest for multiferroics in $RFeO_3$ has been extended to their interaction with light mainly photovoltaic properties[13, 14]. This adds another coupling possibility to the multiferroic materials, making $RFeO_3$ ideal multifunctional materials for future-devices. The knowledge of the structural, electronic, as well as the influence of defect state on these properties, are very crucial.

Therefore, in the first part of the work, the structural characterization and the correlation between structural optical properties have been explored using experimental and theoretical investigations. In the second part, the origin of possessing high magnetic moments in $RFeO_3$ systems even these systems are well-established antiferromagnetic materials have been investigated considering various site defects and using theoretical investigations. These analyses provide us a basic understanding of the multiferroic coupling phenomena in $RFeO_3$ systems. In the third and last part of this work, detailed experimental and theoretical investigations on the doubly forbidden (according to electric dipole and spin selection rules) d-d transitions in $RFeO_3$ systems have been done. The analysis of d-d transitions provides basics for the investigation to fabricate optical devices using these materials.

1.2 Perovskite-type Oxides

The term perovskite is generally used for the class of compounds which have the crystal structure type of calcium titanate. The Ruddlesden-Popper phase (RPP) is the most general form of perovskite structure consist of two-dimensional perovskite slabs interleaved with cations. The general form of RPP is $A_{n+1}B_nX_{3n+1}$, where A and B are cations and X is an anion (i. e. Oxygen), and n is the number of the layers of octahedra in the perovskite-like stack. The RPP series of the form $A_{n+1}B_nX_{3n+1}$ are essentially made of n ABX_3 perovskite separated by an AO layer[15]. $n = \infty$ corresponds to the ABX_3 perovskite-type structure, while n = 1 and n = 2 corresponds to A_2BX_4 and $A_3B_2X_7$ type structure of RPP series respectively. As per the available literature the perovskite is believed to be discovered first by Gustav Rose and is named after Russian mineralogist L. A. Perovski [16]. The general chemical formula of materials ($n = \infty$) crystallize in the perovskite structure is ABX_3. In the case of perovskite-type oxides, the X site is occupied by oxygen O. Thus, the perovskite oxides usually represented with a general formula ABO_3, where A site occupied with a larger ionic radius element such as rare-earth, alkali or alkaline earth metal ions and B site is generally occupied by transition metals. A site atom situated at the corner and B site atom remains at the center of the unit cell forming three-dimensional BO_6 octahedra with six Oxygen atoms at the center of each face. An ideal perovskite structure adopts a cubic symmetry and crystalizes in the space group $Pm\bar{3}m$ [17] as shown in Figure 1.1.

The perovskite structures have received a great research interest because they can accommodate a large number of chemical elements into its structure. The doping of small chemical impurity introduces a significant amount of structural distortions and modifies the electronic structure of these materials to a large extent. Thus, the physical properties of perovskite oxides can be engineered.

The perovskite structure crystalizes in several different distorted lattices depending upon the structural flexibility of stabilization. The stability of the structure defined in terms of Goldschmidt tolerance factor *t* based on the ionic radii of the A and B site cations[18] and used as a figure of merit to characterize perovskites[19, 20]. The tolerance factor t is calculated according to equation (1.1) using the radii of the ions for general perovskite formula ABO_3.

$$t = \frac{r_A + r_O}{r_B + r_O}, \tag{1.1}$$

where r_A, r_B and r_O are the ionic radii of A, B and Oxygen atoms respectively.

For an ideal cubic perovskite structure tolerance factor *t* considered to be unity. In practice, the tolerance factors of cubic perovskites range from 0.8 to 1. The structural distortion in the lattices will increase with a deviation of *t* to either higher or lower values than *unity*. The distortion from the ideal perovskite structure can lead to a lower symmetry from cubic to orthorhombic, rhombohedral, tetragonal, monoclinic, or triclinic. The orthorhombic and rhombohedral lattices are the most common for the perovskites[21-24]. The perovskite structure is assumed to be stable if the tolerance factor lies between 0.8 and 1. The incorporation and combination of different elements into the structure lead to distortions of the perovskites from the ideal cubic structure. A vast amount of work has been done to investigate the various type of distortions such as rotation or tilt of BO_6 octahedra, displacement of the cations and the distortion of the BO_6 octahedra and their consequence on the crystal symmetry.

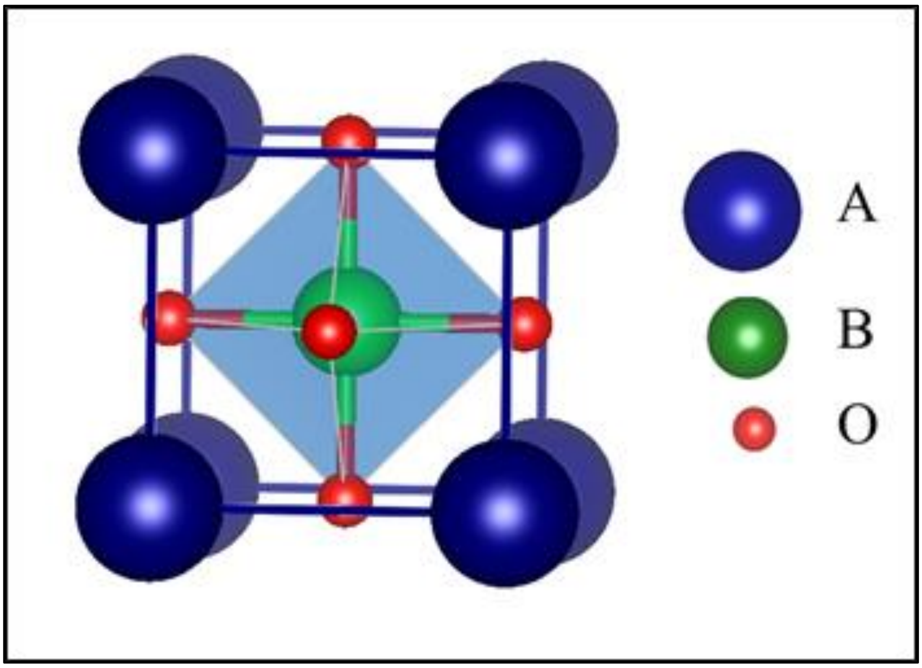

Figure 1.1: *The ideal cubic $Pm\overline{3}m$ structure of ABO_3 perovskite oxides. A is a large 12-fold and B is a small 6-fold coordinated cations.*

The variety of the elements that can be incorporated into the perovskite system and the structural flexibility with respect to distortions lead to various properties such as metal-insulator transition[25, 26], colossal magnetoresistance[27], multiferroic behavior [28, 29], etc. since long. ABO_3 perovskite-type oxides possess more than one property which can be potentially used in technological applications and thus called multi-functional materials such as multiferroics. Multiferroics materials combine several ferroic orders and are commonly classified as “type-I” and “type-II”. In “type-I” multiferroic materials ferromagnetism and ferroelectricity arises independently. $BiFeO_3$ is the classical example of multiferroic materials of “type-I”. In “type-II” multiferroic materials ferroelectricity exists in a magnetically ordered state and is arises due to a particular type of magnetism[10, 30]. For example, in $TbMnO_3$ magnetic ordering appears at 41 K and 28 K, the electric polarization appears in this material at low temperatures. The rare-earth manganites and ferrites are the examples of “type-II” multiferroics, in which magnetic ordering of A and B cations break the symmetry and gives rise to a ferroelectric displacement[31, 32]. Advances in thin film growth techniques have opened the way to strain-engineering over the existing properties of these materials[25, 33, 34]. It has also improved the ability to accurately characterize the multiferroic properties and design practical devices based on the magneto-electric coupling.

Among all the perovskite the rare earth orthoferrites possess special status due to their fascinating magnetic and ferroelectric ordering [28, 29, 35-40] because these materials have potential applications in spintronics and data storage including high-speed memory devices, magnetically tenable switches and sensors.

1.3 Rare-earth Orthoferrites

Recently, rare-earth orthoferrites ($RFeO_3$) perovskites have attracted the attention of the scientific community worldwide due to the coexistence of electric and magnetic polarization in these materials[28, 29, 41-43]. These materials have also attracted interest due to their novel magneto-optical properties[44-46]. All members of the $RFeO_3$ family known to possess a canted antiferromagnetic structure arising from spins of the Fe^{3+} ions [47, 48]. The antiferromagnetic ordering of the iron ions occurs at Neel temperature (T_N) between 650K and 750K. Several orthoferrites have shown a spin reorientation at lower temperatures [49-52]. The existence of electric polarization in $RFeO_3$ samples which possess a centrosymmetric space group (Pbnm) is an interesting phenomenon because it requires a space group with a non-centrosymmetric point of inversion. $RFeO_3$ is again retrieving interest of researchers because of their fast spin dynamics [52-54], electric field control of magnetization and vice versa [55, 56]. Another interest is the possible application of these materials in devices because some of these compounds have recently shown to exhibit spontaneous electric polarization[41], which makes them multiferroic[28, 29] possibly due to their magnetic structure[12, 57].

At room temperature, $RFeO_3$ are known to acquire an orthorhombic crystal structure with space group Pbnm [58-61]. This orthorhombic structure of $RFeO_3$ can be derived from the rotation or tilts of FeO_6 octahedra of an ideal cubic Pm3m perovskite structure, where this tilt can be tuned by the ionic radius of the rare earth cations R or by doping at Fe site.

In all the compounds of rare-earth orthoferrites group have been studied by using neutron diffraction and it was found that at room temperature the iron lattices are aligned antiferromagnetically and each iron ion having six anti ferromagnetic nearest neighbors [62-66]. On the other hand, the repeatability of the results of measurements of the weak ferromagnetism by the various groups[67-69] suggests that it is an intrinsic property of these materials. Dzyaloshinskii and Moriya have explained the origin of the weak ferromagnetism *via* antisymmetric exchange interaction and in the next section, this has been discussed in detail.

1.3.1 Antisymmetric Exchange Interaction

It is shown by Dzyaloshinskii and Moriya “the combination of low symmetry and spin-orbit coupling give rise to an anisotropic exchange interaction” known as Dzyaloshinskii-Moriya (DM) interaction or antisymmetric exchange interaction. The presence of DM interaction favors a spin canting in magnetically ordered systems which leads to intrinsic weak ferromagnetism in an antiferromagnetic system like $RFeO_3$.

The DM interaction explains the contribution to the total magnetic moment due to exchange interaction between two neighboring magnetic spins $\boldsymbol{S_i}$ and $\boldsymbol{S_j}$ slightly canted with each other as shown in Figure 1.2. In DM interaction the Hamiltonian can be expressed according to equation (1.2) given below

$$H_{DM} = \boldsymbol{D}_{ij}.\left(\boldsymbol{S_i} * \boldsymbol{S_j}\right), \qquad (1.2)$$

where $\mathbf{D}_{ij}$ is a coupling constant and defined by the equation (1.3)

$$\boldsymbol{D_{ij}} \propto \boldsymbol{r_i} * \boldsymbol{r_j}, \tag{1.3}$$

The equation (1.3) implies that the direction of $\mathbf{D}_{ij}$ is perpendicular to the plane of the triangle formed by the two neighboring spins with a ligand as shown in Figure 1.2. Here, $\boldsymbol{r_i}$ and $\boldsymbol{r_j}$ are the vectors connecting to the ligand from two neighboring spins S_i and S_j respectively. For $RFeO_3$ perovskite-type structure the direction vector of D_{ij} must be perpendicular to the Fe–O–Fe plane and the symmetry restriction [70]. In more general terms, if we consider ABO_3 perovskite structure, the A and B sites substitutions lead to the oxygen octahedra tilt and distortion. This octahedron tilt and distortion move each oxygen ions of B-O-B configuration away from 180° or from the middle point, give rise a bent in B-O-B bond angle and break the axis rotation symmetry. The change in the B-O-B bond angle will modify DM interaction as a relativistic correction to the superexchange interaction between the B ions. This suggests that the antisymmetric B-B exchange interactions can be changed by changing structural tilts and (or) distortions in the ideal perovskites.

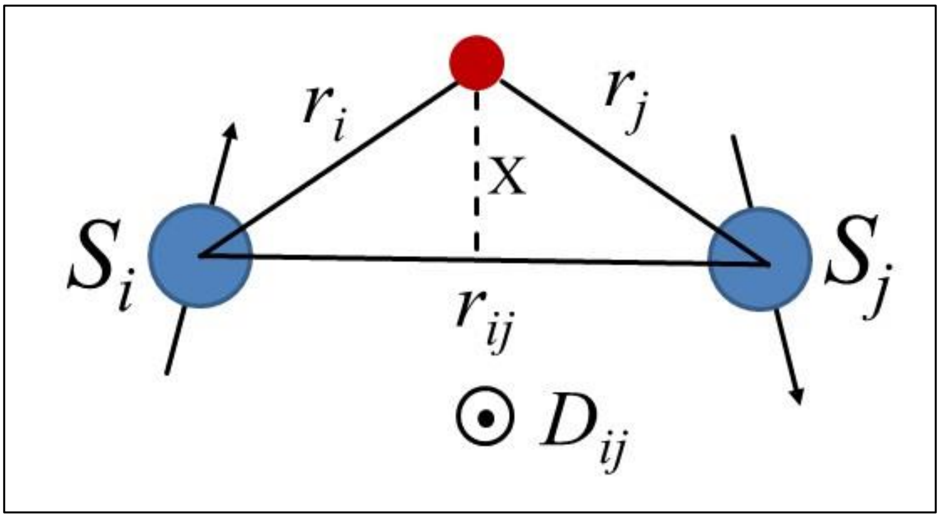

Figure 1.2: *Schematic Showing the DM vector and antisymmetric exchange interaction between two near-neighbor spins.*

The antisymmetric exchange interaction plays an important role in understanding the multiferroic behavior of an antiferromagnetic system like $RFeO_3$. It explains not only the origin of the net ferromagnetic moment but also it is important for the understanding of magnetic field induced electric polarization in multiferroic materials [71, 72].

1.3.2 Zener Double Exchange Interaction

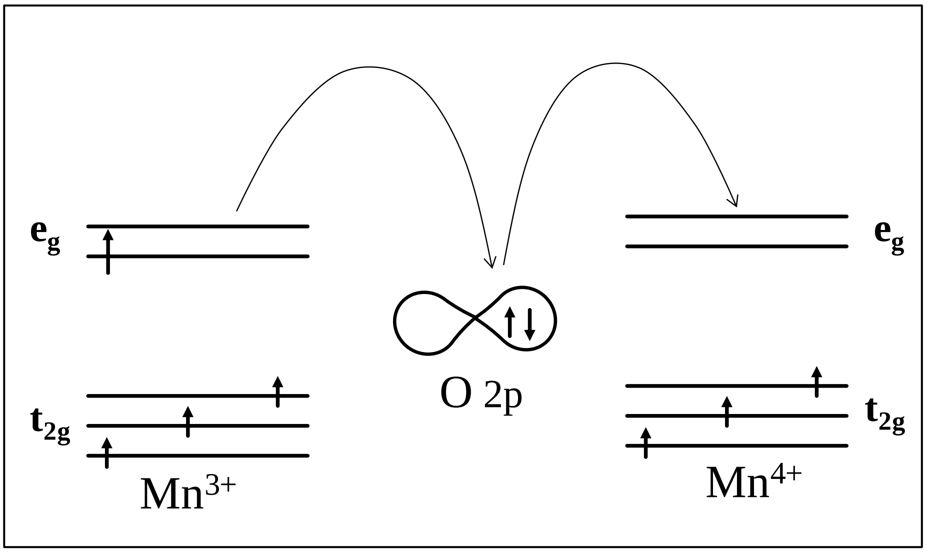

Figure 1.3: *Schematic explaining the Zener double-exchange mechanism responsible for ferromagnetism in $La_{1-x}Ca_xMnO_3$. The exchange involves the outermost orbitals like $3d^4$ (Mn^{3+}), $3d^3$ (Mn^{4+}) and $2p^6$ (O^{2-}). t_{2g} and e_g are the crystal field splitting of d orbitals due to distortion of MnO_6 octahedra[73, 74].*

The mixed valency states in perovskite structure lead to the ferromagnetism such as in $La_{1-x}Ca_x(Mn_{1-x}^{3+}Mn_x^{4+})O_3$. It was first proposed and established by Clarence Zener [75], also known as *Zener double exchange interaction*. Zener pointed out that ferromagnetic spin ordering facilitates the carrier hopping to an empty neighboring d orbital. Zener explained this phenomena in the following way: (1) intra-atomic exchange is strong so that the only important configurations are those where the spins of each carrier is parallel to the local ionic spin; (2) the carrier do not change their spin orientation when moving; accordingly they can hop from one ion to the next only if the two ionic spins are not antiparallel, i. e the electron transfer in Mn^{3+}-$O2^-$-Mn^{4+} will not change the direction of the spin; (3) when hopping is allowed the ground state energy is lowered because of strong Hund's rule coupling. This results in lower energy for ferromagnetic configurations. Zener pointed out that ferromagnetic spin ordering facilitates the carrier hopping to an empty neighbor d orbital.

Figure 1.3 shows the schematic of the double-exchange mechanism depicted in $La_{1-x}Ca_xMnO_3$ system where Mn ions remain in the mixed valence states of Mn^{3+} and Mn^{4+}. Due to the crystal field of MnO_6 octahedra, d orbital splits into t_{2g} and e_g orbitals. Mn^{3+} have partially filled while Mn^{4+} have an empty e_g orbitals. Thus, the hopping of electron will transfer one electron from O^{2-} to Mn^{4+} ions and simultaneously one electron transfer from partially filled e_g orbital of Mn^{3+} to O^{2-} ion [76]. Zener established that the cation of the same element having different valence states exchange electrons through oxygen ions via hoping mechanism. For example, $F^{3+}\text{-}O^{2-}\text{-}Fe^{2+}$ can transfer an electron by hoping mechanism to convert into $F^{2+}\text{-}O^{2-}\text{-}Fe^{3+}$ similarly from $F^{3+}\text{-}O^{2-}\text{-}Fe^{4+}$ into $F^{4+}\text{-}O^{2-}\text{-}Fe^{3+}$.

1.3.3 Crystal Field Splitting

The basic building block around which the physical properties of the $RFeO_3$ perovskite oxides revolve is the FeO_6 octahedra. In orthoferrites, the iron is surrounded by six oxygens in a regular octahedral environment. The five-fold d levels do not have the same energy but are split into two groups, the lower triple level t_{2g} and upper double level e_g. This primarily occurs due crystal field of the FeO_6 octahedra or in other words due to the strong electrostatic field considerations between the metal d electrons and the surrounding negative ions. The doubly degenerated e_g orbitals (d_{z2}, d_{x2-y2}) point directly at these ions and are shifted to higher energy. The triply degenerate t_{2g} orbitals (d_{xy}, d_{xz}, d_{yz}) point in the directions between the ions where the field are less and therefore stabilized at lower energy. The schematic of the crystal field splitting has been shown in Figure 1.4. In perovskite containing trivalent Fe ions bonded with O, the energy of crystal field splitting is smaller than the paring energy of two electrons[77] hence, Fe ions in $RFeO_3$ always remains in the high spin state[78]. An electron can be filled in d shell as per Hund's rule hence will occupy the lowest available orbitals compatible with the total spin associated with the metal ion. For example, Fe^{3+} and Fe^{4+} have configurations of t_{2g}^3, e_g^2 and t_{2g}^3, e_g^1 respectively.

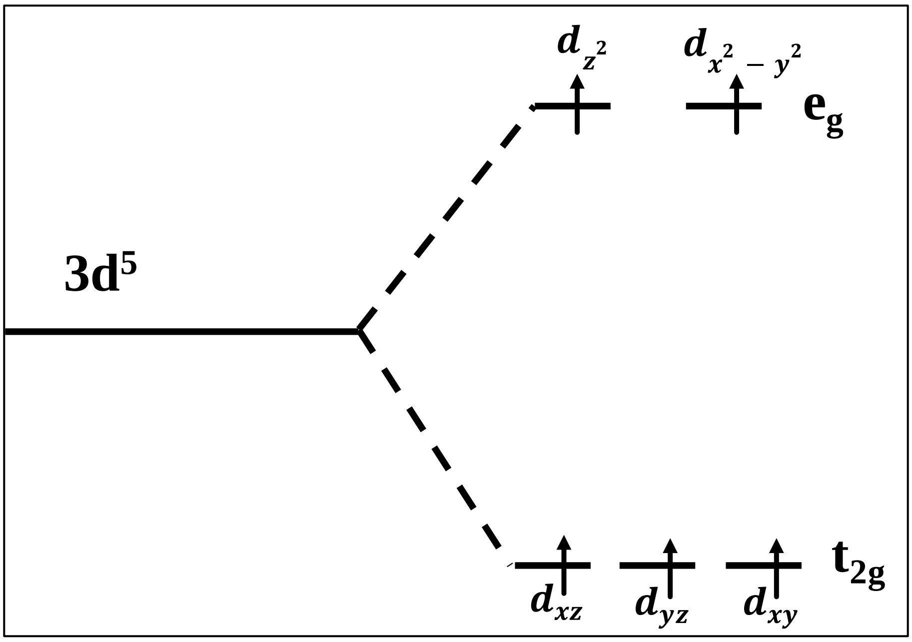

Figure 1.4: *Crystal field splitting of the five-fold degenerate atomic $3d^5$ levels into the lower t_{2g} and higher e_g levels.*

1.4 The Aim of the Present Work

The important characteristic of ABO_3 perovskites is the coupling of their various ferroic properties with the atomic structure, i.e. many of the properties can directly be modified by changing the rotation and distortion of the BO_6 octahedra. This directly affects the B-O-B bond angles and B-O bond lengths. In fact, the tilts and distortions of BO_6 octahedra in these ABO_3 perovskites are the key to control various physical properties such as weak-ferromagnetism[79]. Thus, to understand the physics and related properties of $RFeO_3$ systems, it is very important to examine the structural characteristic such as bond lengths, bond angles, distortion parameters, etc. of these samples with great accuracy. Therefore, this work has been started with the detailed structural characterization of $RFeO_3$ samples using experimental and theoretical investigations.

Furthermore, $RFeO_3$ system is well-known antiferromagnetic (AFM) ground state materials and the antiferromagnetic ordering of the

Fe^{3+} ions is known to occur at Neel temperature (T_N) ~640K-750K but simultaneously, the coexistence of electric and magnetic ordering in $RFeO_3$ samples have been reported [29, 32, 80, 81]. In addition, there exist literature on the weak ferromagnetism in these compounds due to the canting of spins [82, 83]. Thus, in the available literature, there exist large discrepancies regarding the experimentally observed high values of magnetic moments [84-86] and behavior of MH loop for $RFeO_3$ compounds as shown in Figure 1.5. Some experimental reports also suggest the occurrence of double hysteresis loop [84, 85] possibly due to two types of magnetic interactions present in the samples.

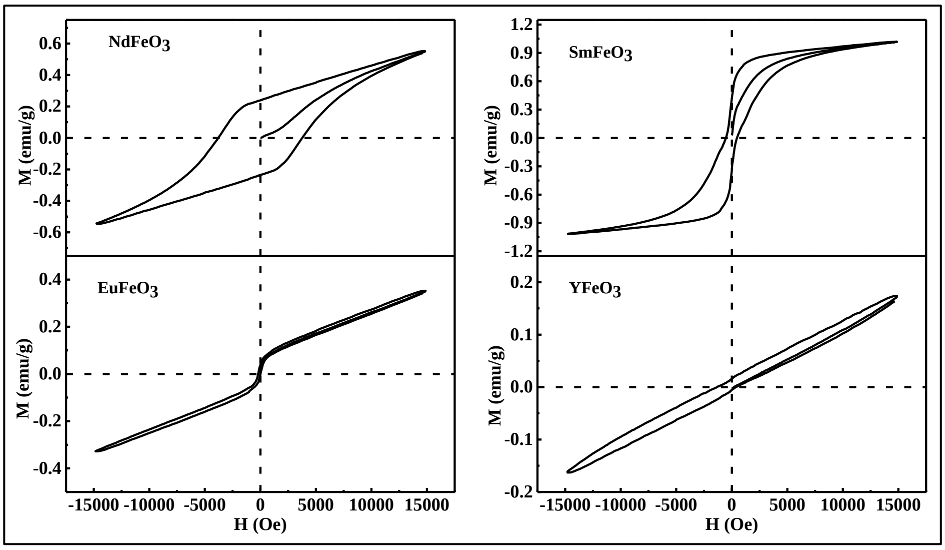

Figure 1.5: *Room temperature M-H curves of prepared $RFeO_3$ samples.*

Some available literature suggests that the formation energy of $RFeO_3$ is larger as compared to its garnet counterpart $R_3Fe_5O_{12}$[87-89]. This reveals that it is difficult to synthesize $RFeO_3$ with a proper stoichiometry especially through solid state route, which may result in self-doping in these systems. Hence, to explore the possible origin of the high value of magnetic moments, the influence of defects on the magnetic properties of $RFeO_3$ have been investigated using density functional theory.

Moreover, another interesting feature of $RFeO_3$ compounds is the d-d transition. It is observed that the strength of d-d transitions is around a thousand times weaker than that of the dipole-allowed p-d transitions (O-2p and Fe-3d)[90]. It is important to note that in $RFeO_3$ system, Fe ion occupies 3+ oxidation state i. e. $RFeO_3$ is a system with d^5 orbital and d^5 orbital splits into t_{2g} and e_g sub-orbitals due to crystal field of FeO_6 octahedra. Interestingly, in d^5 systems, d-d transitions should be forbidden. This is not only according to the electric dipole selection rule ($\Delta l = \pm 1$) but also according to the spin selection rule ($\Delta S = 0$). The schematic of the splitting of 3d orbital and electron allocations have been shown in Figure 1.6. Also, the d-d transition should be forbidden for d^5 orbital as it is completely half-filled and there is no extra electron to get excited from t_{2g} to e_g level.

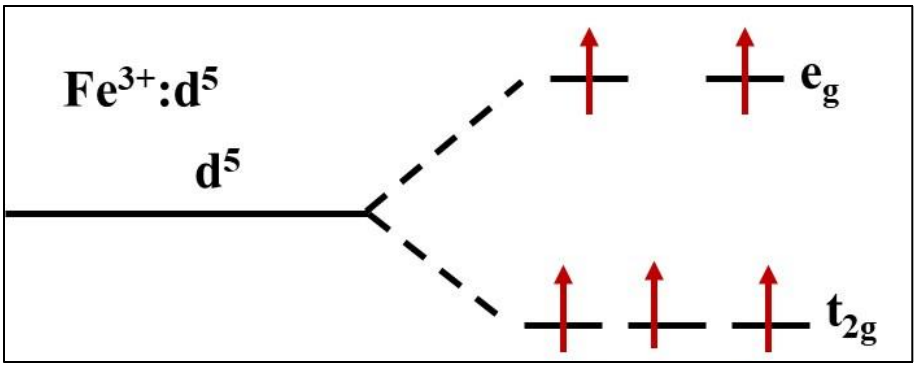

Figure 1.6: *Schematic showing possibilities of d-d transitions in d^5 orbitals.*

In recent years, optical absorption spectroscopy has been widely used to probe the electronic structure of various transition metal oxides[91] and it is also known to probe both; the band gap as well as the d-d transitions in transition metal oxide complexes including $3d^5$ systems. Therefore, in this work, we have investigated the correlation between structural, optical properties, possible origins of ferromagnetism and the signature of d-d transitions in optical absorption spectra of $RFeO_3$ systems using various experimental techniques and density functional theory (DFT).

1.5 Organization of the Thesis

The present chapter covers a brief introduction to this work. The remaining chapters of the thesis are summarized as follows:

Chapter 2: Experimental Techniques and Theoretical Background; In this chapter detail about synthesis and characterization techniques relevant to this work have been provided. The sol-gel synthesis, hydrothermal synthesis, solid-state reaction methods have been discussed in detail and used to synthesize the $RFeO_3$ samples. The important characterization techniques such as x-ray diffraction (XRD), diffuse reflectance spectroscopy (DRS), x-ray absorption near edge spectroscopy (XANES), and soft x-ray absorption spectroscopy (SXAS) used for structural and electronic characterizations, etc. are described. The basics of density functional theory (DFT) have also been discussed briefly.

Chapter 3: Synthesis, Structural, and Thermal Properties of Rare-earth Orthoferrites; In this chapter, details about synthesis of rare-earth orthoferrites ($RFeO_3$) and its structural properties in terms of Fe-O-Fe bond angles, Fe-Fe near-neighbor distances (NND), R-O bond lengths, Fe-O bond lengths, and FeO_6 octahedra distortions, etc. have been provided. Because various physical properties such as ferroelectricity, magnetism, optical, etc. are critically controlled by these parameters. A necessary transformation matrix to estimate the tilt angles associated with FeO_6 octahedra using oxygen Wyckoff positions have been demonstrated in detail. The details of differential scanning calorimetry (DSC) measurements have also been provided. DSC measurements were performed to explore the variation of Neel temperature with structural parameters of $RFeO_3$ samples.

Chapter 4: Optical and Electronic Properties of Rare-earth Orthoferrites; the present chapter has been devoted to exploring the effect of R-site ionic radius on the optical and electronic properties of $RFeO_3$ (where, R= La, Pr, Nd, Sm, Eu, Tb, Dy, Y, Ho, Er, and Yb). The optical absorption spectroscopy has been used to probe the electronic structure of similar ferrites and the said electronic structure is believed to be responsible for various physical properties of these materials.

Chapter 5: Theoretical Investigations of Structural, Electronic, and Magnetic Properties of Rare-earth Orthoferrites; In this chapter, the details of structural, electronic and magnetic properties of $RFeO_3$

samples using theoretical approaches have been provided. The structural parameters (such as lattice constants, Fe-O/R-O bond lengths, octahedra tilts) of $RFeO_3$ samples shown (experimentally determined) in chapter 3, have been validated using and *Bond Valence Sum* (BVS) and *Density Functional Theory* (DFT). Further, the optical properties such as bandgap of $RFeO_3$ samples as discussed in chapter 4, have been examined in detail using DFT. Furthermore, a detailed study of defect-induced ferromagnetism of $RFeO_3$ samples has been obtained using DFT.

Chapter 6: Possible Origin of d-d Transitions in $RFeO_3$ ($3d^5$) Systems: Experiments and Theory; Present chapter deals with the possible origin of d-d transitions peak in the optical absorption spectra of $RFeO_3$ samples. It has been observed that the presence of peak due to d-d transition is associated with the annealing temperatures driven defects present in these samples. Our experimental and theoretical analysis suggests that the non-stoichiometry present in samples is the main origin of d-d transitions peak in the optical spectra of $RFeO_3$ samples and so does in d^5 systems.

Chapter 7: Conclusions and Future Perspectives; This chapter summarizes the results of the present research work with concluding remarks. The possible future scope of present study has also been discussed.

Chapter 2

Experimental Techniques and Theoretical Background

In this chapter detail about synthesis and characterization techniques relevant to this thesis have been provided. The sol-gel synthesis method has been used to synthesize the samples. The important characterization techniques such as x-ray diffraction (XRD), diffused reflectance spectroscopy (DRS), x-ray absorption near edge spectroscopy (XANES), and soft x-ray absorption spectroscopy (SXAS) used for structural and electronic characterizations, etc. are described. The basics of density functional theory (DFT) have also been discussed briefly.

2.1 Synthesis of $RFeO_3$

2.1.1 Sol-gel Synthesis Method

The sol-gel process is one of the well-established synthesis methods to prepare novel metal oxide nanoparticles and oxide ceramic[92]. This synthesis method has potential control over the textural and surface properties of the materials. This method depends on the transformation of relevant liquid precursors to sol and finally to a network structure called a gel. A ‘sol’ can be more generally defined (according to IUPAC) as a colloidal suspension, which is defined as a dispersion of one phase in another, where the molecules dispersed in a medium have at least in one direction with a dimension roughly between 1 nm to 1μm. Generally, the gel state is simply defined as a non-fluid 3D network that extends through a fluid phase. Sol-gel method can be classified into two routes; 1) aqueous sol-gel method, if water is used as a reacting medium and non-aqueous sol-gel method, if organic solvent used as a reacting medium.

In aqueous sol-gel method, oxygen is necessary for the formation of metal oxide and in this method, oxygen is supplied by water solvent. Generally, metal acetates nitrates, sulfates, chlorides, and metal alkoxides are used as the metal precursors for this method. However, nitrates were widely used as precursors for the production of metal oxides with an aqueous sol-gel method. The gel obtained is densified through thermal annealing. It is possible to fabricate ultra-fine ceramic powders, glassy, aerogel materials using this method. The main advantages of the sol-gel process are;

- lower formation temperature,
- high homogeneity,
- precise composition control of multi-component compounds and
- synthesis with low-cost apparatus.

Synthesis of rare-earth orthoferrites

In this work, the ‘aqueous sol-gel’ method [93] has been used to synthesize a series of polycrystalline $RFeO_3$ samples. The gels have been prepared by using stoichiometric amounts of Iron Nitrate Nonahydrate ($Fe[NO_3]_3$:$9H_2O$), corresponding rare-earth oxides with nitric acid (HNO_3), Citric Acid (CA) ($C_6H_8O_7$) and Ethylene Glycol (EG) ($C_2H_6O_2$). For the preparation of the samples by this method, the corresponding rare-earth oxides were first dissolved in nitric acid (HNO_3). The obtained rare earth nitrites were dissolved in 50ml of water and stirred at 70-80^oC for 30minutes. $Fe[NO_3]_3.9H_2O$ was dissolved in 50ml water and after stirring of 30 minutes it was added to the rare-earth metal solution. The mixtures of $Fe[NO_3]_3.9H_2O$ and corresponding rare earth nitrates were heated at 80-100^oC with stirring for 3h to avoid precipitation and to obtain a homogeneous mixture. The brown color clear solution with no precipitation, for each combination of $RFeO_{3,}$ was obtained. This was followed by the addition of ethylene glycol and citric acid in a molar ratio of metal ions: citric acid: ethylene glycol 1:1:1.

Ethylene glycol and citric acid used as a complexing and chelating agent respectively [93]. After 6-8h of stirring on the hot plate, the gel initially started to puff up and fill the beaker, producing foam like precursor consisting of very light and homogeneous gel. The resultant gel was dried at 400^{o}C in the air for 10 hours to burn out the organic compounds present in the gel. The powder obtained at this stage is grounded in an agate mortar, again sintered at 900°C in air for 10hours.

2.1.2 Solid State Reaction Method

Solid state reaction is one of the simplest and most commonly used methods for the synthesis of a variety of bulk ceramics. In this method, exchange of ions involves heat treatment of a well ground specimen under vacuum, inert gas, or at ambient atmosphere at high temperatures, often in the range of 900 to 1500 ^{o}C. The required rate of solid state exchange reaction and corresponding temperature depends on the type of cation and anion.

The first step in the solid state reaction synthesis method is to weigh the raw materials in stoichiometric amounts and mix homogeneously. In order to make a homogeneous mixture, grinding is done in a volatile liquid medium such as propanol. Materials used for the reaction should be fine-grained in order to maximize the surface area and hence the reaction rate. Pelletizing the compound is helpful in speeding up the reaction during the sintering process by increasing the area of contact between the grains. Since solid state reaction takes place at high temperatures it is necessary that the container used for the sintering process should be chemically inert to the reactants under desire heating conditions. Metals such platinum is the most suitable candidate but is expensive. Therefore, good quality alumina (Al_2O_3) having melting point ~ 2400 ^{o}C can be used for sintering purposes. In solid state synthesis process, high purity alumina boats and crucibles have been used.

After grinding, the compounds were heated to a fixed sintering temperature at a fixed rate and held for the fixed time and then cooled down to room temperature. This process is referred to as isothermal sintering and most of the chemical reaction occurs at this step. The isothermal sintering temperature and process vary for different compounds. The final product of the reaction usually requires several hours, or even days, depending on the reaction rates. The reaction is often significantly facilitated by cooling and grinding the sample repeatedly. The effect of grinding is to maintain a high surface area as well as to bring the fresh surfaces into the contact. Repeated sintering was performed in order to increase the density of the pellets formed during the sintering. The isothermal sintering was done using high-temperature furnace having microprocessor-based PID temperature control. We have used the solid state reaction method to synthesize pure and defected YFeO3 and is discussed in chapter 6.

2.1.3 Hydrothermal Synthesis Method

The concept ‘hydrothermal’ originates from earth science in the nineteenth century, where it implies a regime of high temperatures and water pressures[94]. Hydrothermal synthesis refers to the synthesis of the substances via chemical reactions and relies on the forced hydrolysis of the reactants in order to produce the oxide ceramics. This is achieved at moderate temperatures (~200 ^oC) and high pressures by placing the reagents in a sealed container and heating the system to the reaction temperatures. In the hydrothermal synthesis process, the crystal growth is normally performed in an apparatus consisting of a steel pressure vessel called autoclave. The solvent is usually deionized water and a metal hydroxide (such as KOH, NaOH) is added as a mineralizer, while metal salts serve as the source of metal ions. As in precipitation systems, nucleation is followed by particle growth to yield a powder with a certain particle-size distribution. Hydrothermal synthesis offers many advantages such as relatively mild operating conditions (reaction temperature < 250 ^oC), one-step synthesis process, environmentally friendly and good dispersion in solution. Moreover, hydrothermal synthesis is inexpensive in terms of instrumentation and energy consumption as compared to other synthesis methods.

The main difference between hydrothermal and solid-state reactions lies in the ‘reactivity’. Solid state reactions depend on the diffusion of the raw materials at the interface, whereas in hydrothermal reactions the reactant ions or molecules react in solution. Hydrothermal synthesis deals with the chemistry in preparation, synthesis, assembly of special compounds or materials through solution route. More importantly, many compounds or materials with special structures and properties, which cannot be prepared from solid-state synthesis, may be obtained by hydrothermal reactions. In this work, the hydrothermal synthesis method is used to prepare a stoichiometric sample of $YFeO_3$ and will be discussed in chapter 6. The hydrothermal synthesis procedure includes the following steps[94];

- To choose suitable reagent;
- To determine the molar ratio of reagents;
- To mix the reagents;
- To put the mixture of reagents into an autoclave and seal the autoclave;
- To choose suitable reaction temperature and reaction time;
- To take out the autoclave from the oven and cool the autoclave to room temperature;
- To open the autoclave and take out the products from the autoclave;
- To process the products such as wash, filter, and dry;
- To characterize the products by using suitable research instruments.

2.1.4 Preparation of Circular Pellets

After synthesis of pure phase powder samples of $RFeO_3$, highly dense circular pellets have been made using a high-pressure hydraulic press, particularly for the dielectric and magneto-dielectric measurements. The pure phase powder is pressed in the form of a circular pellet by means of a hydraulic press and a 13 mm circular die set. Then pellets are again sintered at high temperature. This post-sintering of pellets helps to improve the crystal quality by minimizing defects, enhance grain growth by reducing the total area of grain boundary, and maximize the possible density of the samples. In this work, the pure phase $RFeO_3$ powder samples have been pelletized at a pressure of 13-15 ton to form 1-1.5 mm thick circular discs of 13 mm diameter. These pellets were finally sintered in air at 1300 °C for 12 hours and these pellets are then used for rest of the measurements.

2.2 Characterization Techniques

2.2.1 X-Ray Diffraction

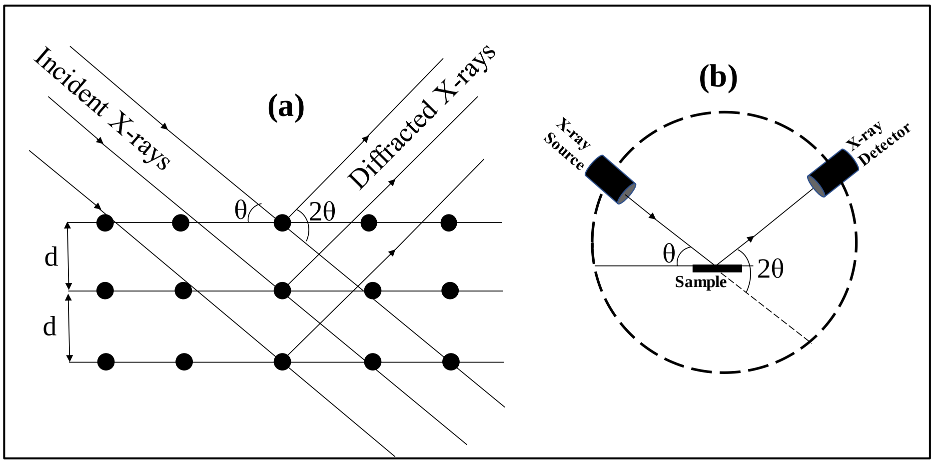

Figure 2.1: *(a) the schematic of Bragg's law of x-ray diffraction, (b) schematic of instrumentation used during x-ray diffraction measurement.*

The discovery of x-rays by Wilhelm Conrod Roentgen in 1985 followed by the work of W. L. Bragg made possible to examine the structural properties of the materials using x-rays diffraction (XRD) technique. It is a non-destructive characterization technique and extremely useful tool for the investigation of crystal structure, strain analysis, particle size determination of crystalline materials. Since the wavelength of x-rays is comparable to the inter-atomic distances, they are suitable to probe the structural arrangement of atoms and hence provide detailed information about the various structural parameters like lattice constants, particle size, unit cell volume, various kind of bond lengths and bond angles, etc.

The incident x-rays primarily interact with electrons bound to the atoms in the lattice as shown in figure 2.1 (a) and (b). The x-rays fall on the material at some incidence angle, gets diffracted through a different set of atomic planes present in the crystal. According to Bragg's law of x-ray diffraction, a certain wavelength of radiation will constructively interfere if they are reflected between crystal planes with a path difference equal to an integral number of wavelengths i. e.

$$2d \sin\theta = n\lambda, \tag{2.1}$$

where d is the interplanar distance, θ is the angle between incident x-rays and planes of reflection, and λ is the x-rays wavelength and n is an integer. There are set of planes of lattices which are indexed using Miller indices *hkl* and the interplanar distances d could also be written as d_{hkl}. In this way, with the satisfaction of Bragg's condition, a peak, across the corresponding θ value appears in the intensity versus 2θ curve.

The intensity of powder diffraction peaks is determined by the atomic scattering factor or form factor f_{hkl}. Form factor (f_{hkl}) depends on the crystal structure including relative positions of atoms in the unit cell, types of unit cells and other characteristics such as thermal motion, and population parameters. The expression for f_{hkl} is given by equation

$$f_{hkl} = \sum_{n=1}^{N} g^n t^n(s) f^n(s) e^{2\pi i(hu_n+Kv_n+lw_n)}, \tag{2.2}$$

where, $f^n(s)$ is the atomic scattering factor, g^n is the population factor of the nth atom, $t^n(s)$ is the temperature factor, (*h, k, l*) Miller indices, and (*u, v, w*) are the fractional co-ordinates of the n^{th} atom in the unit cell. In addition to the primary structural factors, the intensity of diffraction also depends on other factors such as sample's grain size, its shape and size and instrument components such as the intensity of the x-ray beam, detector, slit and monochromator geometry, etc.[95, 96].

In this work, primary phase-purity check of the samples has been done using lab source XRD experiments on a Rigaku SmartLab, diffractometer, with Cu K_α (λ = 1.54 Å) radiation was employed and operated at an applied voltage of 45 kV and current of 40 mA. The phase identification for all as-synthesized samples reported here was performed by matching the peak positions and intensities of the patterns that are available in the Joint Committee on Powder Diffraction Standards (JCPDS) database. For the calculations of structural parameters such as lattice constants, bond-angles, bond-lengths, and octahedra tilts with great accuracy, a synchrotron powder x-ray diffraction experiments were performed at Indian synchrotron radiation source (Indus-II), at Raja Ramanna Center for Advanced Technology Indore, India. The detail of the experimental parameters will be discussed in Chapter 3.

2.2.2 Differential Scanning Calorimetry

Differential scanning calorimetry (DSC) measurement is a useful technique which measures the heat flow associated with various phase transitions of a material as a function of temperature. This technique often used to study the phase transitions as a function of temperature, change in the heat capacity of endothermic and exothermic processes. When sample absorbs energy i. e. the change in enthalpy is positive, it is called endothermic and conversely when the sample releases energy i. e. when the enthalpy is negative, the process is said to be exothermic.

The DSC measurement system has a platform to keep the sample and the reference material is kept in the appropriate pan. The reference material is chosen in such a way that it does not decompose in the desired temperature range. During measurement, sample and reference material are maintained at the same temperature i. e. $\Delta T = T_s - T_r = 0$, where T_s and T_r are the sample and reference temperatures respectively. If the process is endothermic T_s will lag behind T_r and heat source gives the heat equivalent to the energy difference and this energy difference is recorded against that temperature. Different phase transitions in the sample appear as deviations from the baseline, either in positive (endothermic) or negative (exothermic) direction, depending upon energy (more or less) that needs to be supplied to the sample with respect to the reference materials.

DSC is also useful in determining the ordering temperature of magnetic materials because it is a first-order transition and is often accompanied by the amount of energy absorbed (endothermic process) or release (exothermic process)[97]. Anti-ferromagnetic and ferrimagnetic transitions in solid materials govern by exothermic processes and can be observed by exothermic shifts in upward direction in DSC thermograms[98].

In this work, DSC measurements were performed on $RFeO_3$ samples using DSC 214 Polyma from NETZSCH in a temperature of 115K-770K at the rate of 10K/min in the N_2 environment for all prepared $RFeO_3$ samples. The DSC results are presented in Chapter 3.

2.2.3 Diffuse Reflectance Spectroscopy

Diffuse reflectance spectroscopy (DRS) is a well-known technique for the qualitative and quantitative analysis of optical properties (such as bandgap and various kind of electronic transitions) of powdered samples. It is a non-destructive technique and the main advantage of DRS is that there is no need for difficult sample preparation, only powder sample could be used for the purpose. The detail of the DRS technique has been provided below.

Let's consider the case where the dimensions of the particles are large compared with the incident wavelength. Since the crystal surfaces can be oriented in all possible direction, the incident radiation is reflected at all angles into the hemisphere from which the incident radiation originates. The reflections in such cases called *diffuse reflection* in contrast to regular reflection from a phase plane boundary (i. e. it is reflected in all directions, unlike light reflected from a polished surface like a mirror) (see Fig. 2.2). Ideally, diffuse reflection is defined by the condition that the angular distribution of the reflected radiation is independent of the angle of incidence[99]. Lambert[100] was the first who proposed the law of diffuse reflection based on his observations that a white wall illuminated by sunlight appears equally bright at all observation angles. Therefore, he assumed that such a surface behaves as radiating independently of the angle of incidence of the radiation.

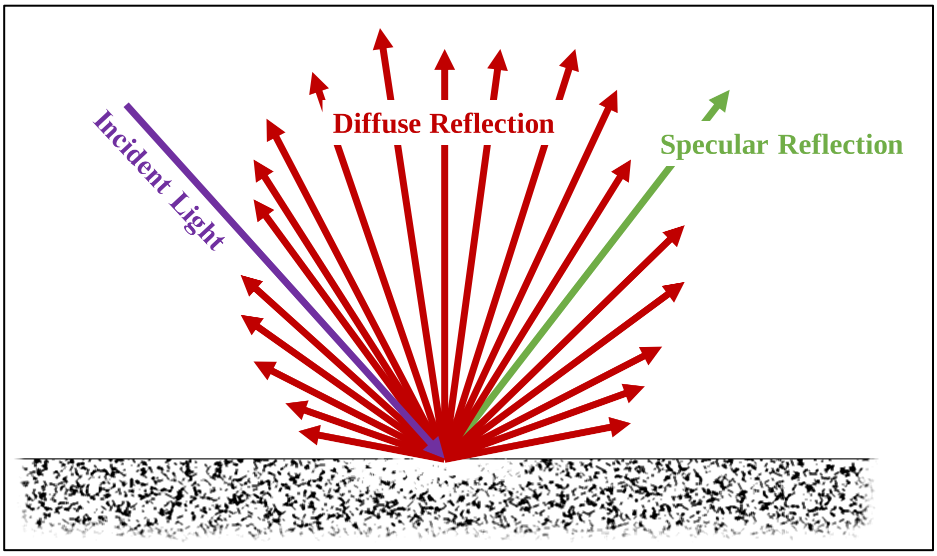

Figure 2.2: *Schematic of diffuse reflection and specular reflection, when a light incident on a rough surface or powder sample.*

Presently, Diffuse reflection spectroscopy (DRS) becomes one of the important tools used to investigate the optical properties of solid samples, especially of powders[101, 102]. Most of the applications of DRS are based on the correlations between observed scattered light and chemical and physical properties of materials.

Although various models exist[103-106], the Kubelka-Munk model is the most common approach to interpret the diffuse reflectance spectra [107-109]. The derivation of Kubelka-Munk formula assumes that light traveling through a diffusely reflecting medium can be divided into two counter-propagating components: one light flux traveling into the medium and another returning towards the surface. Each component loses intensity by scattering and absorption and each also adds up the intensity via scattering of its partner. For the powder or infinitely thick layered samples the Kubelka-Munk equation may be written as;

$$F(R) = \frac{(1-R_\infty)^2}{2R_\infty}, \qquad (2.3)$$

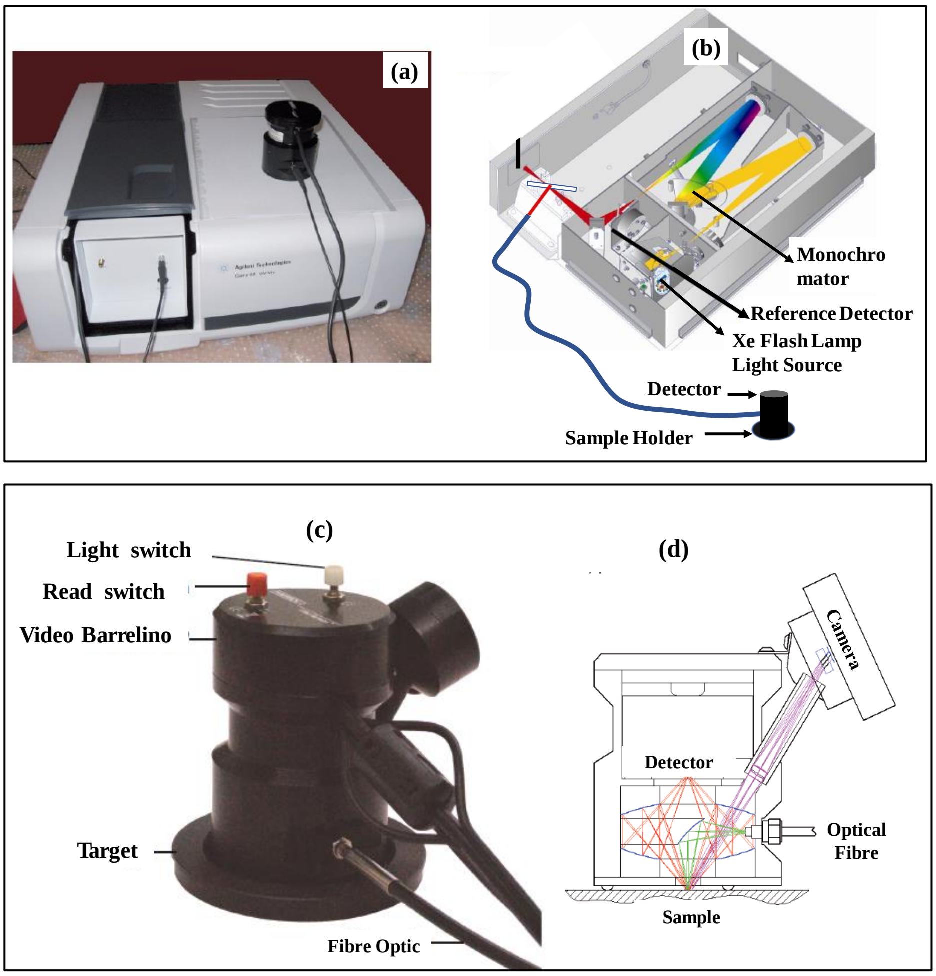

Figure 2.3: *(a) spectrophotometer with DRS attachment in the lab, (b) internal ray diagram of the spectrophotometer, (c) components of DRS attachment, (d) schematic of data collection inside DRS attachment.*

where $F(R_\infty)$ is Kubelka-Munk function and $R_\infty = R_{sample}/R_{standerd}$, R_{sample} is the diffused reflectance of the sample over a baseline of standard sample $R_{standard}$.

We have measured DRS spectra of $RFeO_3$ samples using a commercial spectrometer Cary 60 from Agilent Technology, shown in figure 2.3(a). Figure 2.3 (b) shows its internal ray diagram. In DRS measurement, a broad spectrum of UV-Vis-NIR radiation is made to fall on a rough bulk sample through an optical fiber coupled with source and the diffusely reflected light through the sample are collected using the ellipsoidal lens and guided to the detector (shown in figure 2.3 (c) and (d)). From this radiation, a spectrum is obtained containing the information about the optical properties of target samples. The DRS setup available in the lab can measure the bandgap with an accuracy of 0.001 eV and the detail about the data processing and the calculation of optical bandgap will be discussed in chapter 3, section 3.3.

2.2.4 X-Ray Absorption Spectroscopy

By the absorption of an x-ray photon, a core electron can be excited with a certain kinetic energy to an empty state below the ionization threshold or to an essentially free electron above the ionization threshold as shown in figure 2.4. This process is essentially the photoelectric effect and is the basis of x-ray absorption spectroscopy (XAS), x-ray photoemission spectroscopy (XPS) and x-ray emission spectroscopy (XES). The first two will be discussed in detail in the coming sections of this chapter.

When an x-ray enters a material, the intensity of the x-ray beam decreases due to the absorption of x-ray photons in that material. This phenomenon is described by Lambert-Beer's law, given by the equation below

$$I_f = I_i e^{-\mu d}, \tag{2.4}$$

where I_i and I_f are the incident and transmitted intensities measured before and after the absorption of x-ray photons by the absorber with thickness d and linear absorption coefficient μ. The equation (2.4) may be written as

$$\mu = \frac{1}{d} ln\left(\frac{I_i}{I_f}\right), \tag{2.5}$$

The probability that an x-ray photon is absorbed by the material is given by this absorption coefficient μ described in equation (2.5). As shown in Figure 2.4, it can be noticed that when the x-ray energies equal to the bonding energies of a core-electron of an element in the material, μ increases sharply and this step like feature in an absorption spectrum are called *absorption edge*. The energy of the absorption edge is determined by the binding energy of a core level i. e. at the edge, the photon energy is equal to the binding energy. The absorption edges for an atom can be named according to the principle quantum number of the electron that is, K for n=1, L for n=2, M for n=3, etc.

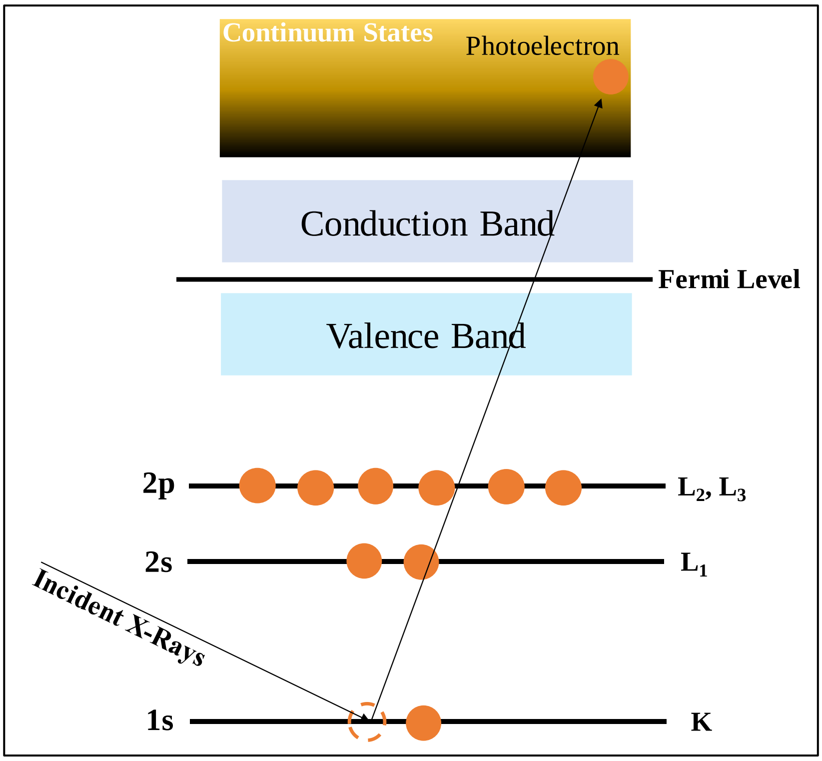

Figure 2.4: *Schematic of x-ray absorption process of a core electron to continuum state[110].*

The x-ray absorption spectra acquired of material shows oscillations just above the absorption edge and these oscillations called x-ray absorption fine structure. Thus, the spectrum can be divided into two parts: the x-ray absorption near edge structure (XANES) up to 50 eV above the absorption edge and the extended x-ray absorption fine structure (EXAFS), region from 50 eV to 1000 eV above absorption edge (as shown in Figure 2.5). In this work, we will focus on XANES spectroscopy.

2.2.4.1 X-ray Absorption Near Edge Structure Spectroscopy

X-ray absorption near edge structure (XANES) spectroscopy is a well-established technique to get information about the electronic structure of a material. In XANES, a photon is absorbed, and an electron is excited from a core state to unoccupied state. To excite an electron in a given core-level, the photon energy must be equal or higher than the binding energy of this core-level. The energy of an absorption edge, therefore, corresponds to the core-level energy, which is the characteristic for each element, making XANES an element-selective technique.

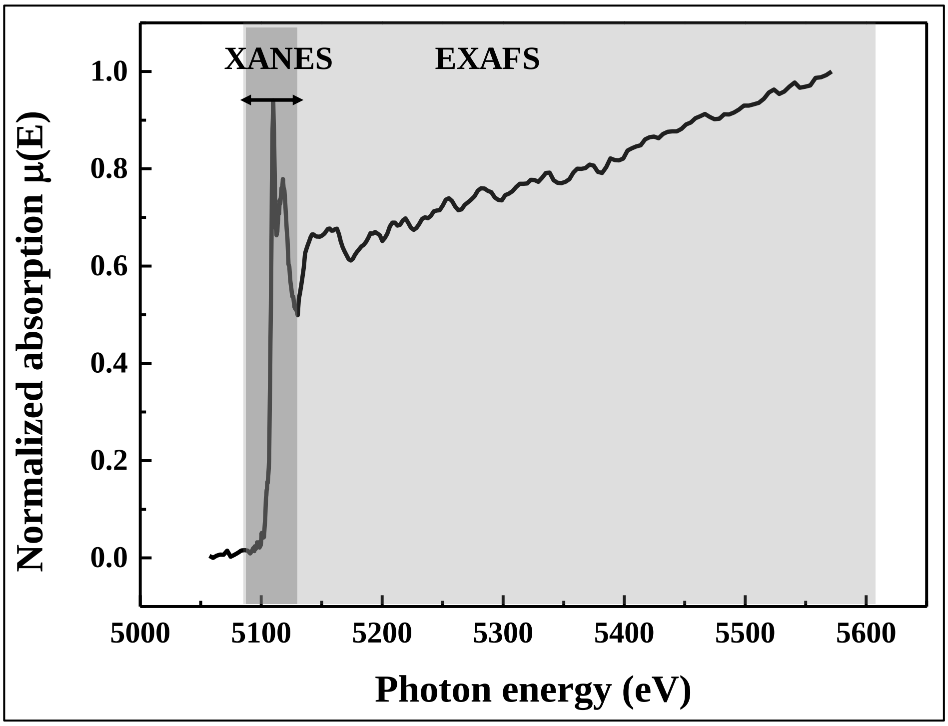

Figure 2.5: *A typical X-ray absorption spectrum showing XANES and EXAFS regions[111].*

XANES basically measures the change in the absorption of the x-rays due to the photoelectric effect and the intensity of the XANES spectra described with the Fermi-Golden rule, which can be written as

$$I_{XANES} \propto \left|< \boldsymbol{\Phi_f} \middle| \hat{e}_{\boldsymbol{q}}.\boldsymbol{r} \middle| \boldsymbol{\Phi_i} >\right|^2 \delta_{E_f - E_i - \hbar\omega}, \qquad (2.6)$$

where, $\hat{e}_{\boldsymbol{q}}.\boldsymbol{r}$ is the dipole matrix operator coupling initial state (Φ_i) and final state (Φ_f). given, δ is the delta function takes care of the energy conservation.

In the final state, a core electron has been excited. It can be described as the initial state with a continuum electron ($\boldsymbol{\epsilon}$) added and a core electron removed, i. e. $\boldsymbol{\Phi_f} = \boldsymbol{c\epsilon\Phi_i}$. Therefore, the intensity of XANES spectra can be written as

$$I_{XANES} \propto |< \boldsymbol{c\epsilon\Phi_i}|\hat{e}_{\boldsymbol{q}}.\boldsymbol{r}|\boldsymbol{\Phi_i} >|^2 \delta_{E_f - E_i - \hbar\omega}, \qquad (2.7)$$

All electron rearrangements that take place when a core hole is excited to a continuum electron are neglected, the delta functions may be replaced with the density of states (ρ) and the XANES spectral intensity becomes

$$I_{XANES} \propto |< \boldsymbol{\epsilon}|\hat{e}_{\boldsymbol{q}}.\boldsymbol{r}|\mathbf{c} >|^2 \rho, \qquad (2.8)$$

The dipole matrix element dictates that the density of stats has an orbital moment that differs be 1 from the core state i. e. $\Delta l = \pm 1$, while the spin is conserved i. e. $\Delta S = 0$. The quadrupole transition is ~ 100 times weaker than the dipole transitions and may be neglected in a broad sense. But, in the case of the metal K edges, the quadrupole transition is important because the 3d density of states is much larger than the 4p density of states and the quadrupole peaks appear in the pre-edge region where there is no 4p density of states[112].

In the present work, Fe $L_{2,3}$ edges, O K edge and Fe K edge XANES measurements were performed in the total electron yield mode to determine the oxidation states of Fe and to probe the d-electrons bandwidth of $RFeO_3$ systems. The experiments were performed at Indian synchrotron radiation center, at BL-01, BL-12, Indus-II, Raja Ramanna Center for Advanced Technology Indore, India.

Fe K Edge (1s) XANES Spectroscopy

Transition metal K edge (1s) XANES spectroscopy is an important technique to investigate local coordination environment and electronic structure depending on sample composition, and structure.

The energy of K edge transition of 3d transition metal have energies ranging from about ~4 keV to ~9 keV. The shift of metal 1s XANES spectra edge energy towards higher energies with higher valence is generally used to determine the valence of 3d transition metals[113]. The metal 1s XANES spectra often interpreted with the help of a molecular orbital approach [114].

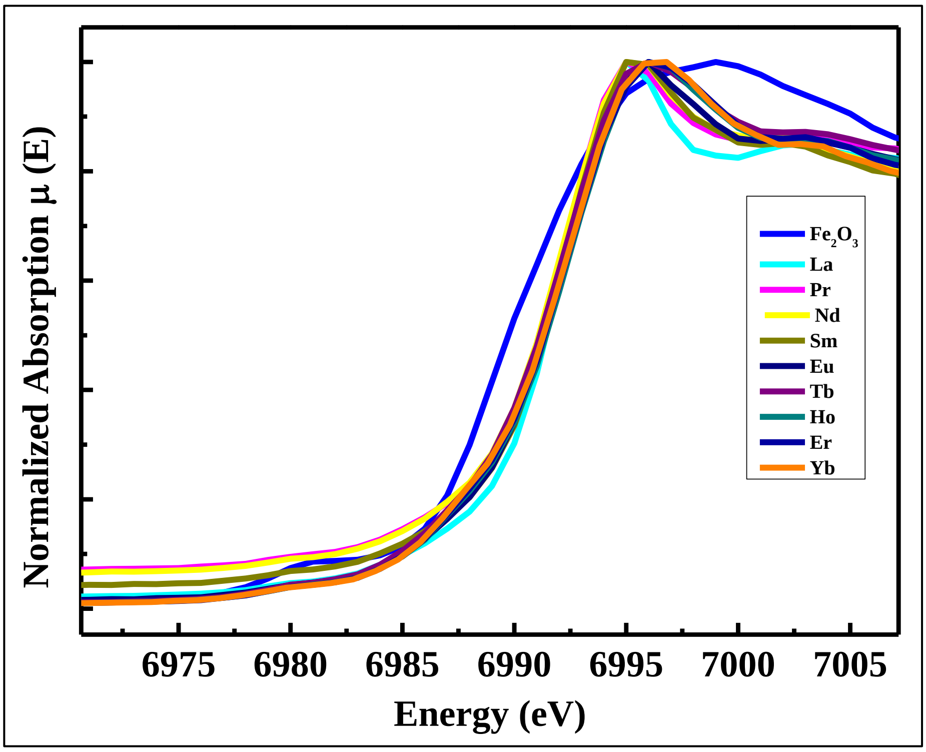

Figure 2.6: *XANES spectra at Fe K edge of $RFeO_3$ samples*

In this work, the Fe K edge XANES spectra of $RFeO_3$ having orthorhombic structure has been investigated. The Fe K edge XANES spectra were acquired at Indian synchrotron radiation center, Raja Ramanna Centre for Advanced Technology Indore, India, Indus-II, BL-12. All the data were taken with an accuracy of 0.1 eV. The measurements were carried out in fluorescence mode using an energy dispersive detector (VERTEX-EX). The spectra were normalized to the incident photon current, measured by an ionization chamber. For the photon energy calibration, the absorption edge energies of Fe foil, FeO and Fe_2O_3 samples we were used as a standard. The normalized XANES spectra of $RFeO_3$ samples along with Fe_2O_3 as a standard has been shown in Figure 2.6 The Fe K edges of $RFeO_3$ samples found shifted towards higher energy than Fe_2O_3 shows the presence of co-existence Fe^{4+} together with Fe^{3+} complexes. The low-energy pre-peak region observed in the Fe K edge spectra is a representative of quadrupole 1s to 3d excitations. We will discuss the detailed analysis of Fe 1s XANES spectra in Chapter 6.

O K Edge (1s) and Fe $L_{2,3}$ edge (2p) Soft X-Ray Absorption Spectroscopy

Since both O K edge (O 1s) and Fe $L_{2,3}$ edge (Fe 2p) XANES spectra use soft energies region of x-rays (i. e. ~300 to ~1000 eV), is known as soft x-ray absorption spectroscopy (SXAS). The O 1s spectra correspond to transitions of an electron from the O 1s core level to unoccupied O 2p orbitals mixed in bands of metal 3d character [115]. Thus, the O 1s spectrum is one of the useful techniques to understand the hybridization between O and metal 3d. The O 1s XANES spectra are usually interpreted by their band structure approach or multiple scattering theoretical calculations. In band structure approach the spectral features are explained by comparison with the atomic and symmetry projected density of states (DOS) calculated using DFT. On the other hand, multiple scattering calculations use a cluster model in which the x-ray absorption cross section is computed using the cluster Green’s function[110].

L-edge or metal 2p x-ray absorption spectroscopy probe transitions of $2s^2 2p^6$ core electrons into 3d valence holes. The L edge spectroscopy for the study of transition metal complexes generally refers to the $L_{3,2}$ edges. The 2p core-hole and d-electron multiplet interactions are responsible for the whole shape of the spectrum. In the case of $L_{2,3}$ SXAS spectroscopy, the single-particle approximation breaks down and the spectral shape is affected by the core hole wave function. The metal $L_{2,3}$ edge spectra are generally understood by the so-called multiplet effect. The O K edge and Fe $L_{2,3}$ edge spectra of $RFeO_3$ samples were collected at Indian synchrotron radiation center, Raja Ramanna Centre for Advanced Technology Indore, India, Indus-II, BL-01. A detailed analysis of these spectra will be given in Chapter 6.

2.3 Density Functional Theory

2.3.1 Introduction

The main goal of the most quantum mechanical approaches is the approximate solution of the time-independent, non-relativistic Schrodinger equation

$$\hat{H}\psi_i(\boldsymbol{x_1}, \boldsymbol{x_2} \ldots, \boldsymbol{x_N}, \boldsymbol{R_1}, \boldsymbol{R_2}, \ldots, \boldsymbol{R_M}) = E_i\psi_i(\boldsymbol{x_1}, \boldsymbol{x_2}, \ldots, \boldsymbol{x_N}, \boldsymbol{R_1}, \boldsymbol{R_2}, \ldots, \boldsymbol{R_M}), \qquad (2.9)$$

where, $\hat{H}$ is the Hamiltonian operator for a system consisting of M nuclei and N electrons. $\psi_i(\boldsymbol{x_1}, \boldsymbol{x_2} \ldots, \boldsymbol{x_N}, \boldsymbol{R_1}, \boldsymbol{R_2}, \ldots, \boldsymbol{R_M})$ stands for the wave function of the ith state of the system, which depends on the 3N spatial coordinates $\{\vec{r_i}\}$, and the N spin coordinates $\{S_i\}$ of the electrons, which are collectively termed $\{\boldsymbol{x}_i\}$ and the 3M spatial coordinates of the nuclei $\{\boldsymbol{R}_i\}$. E_i is the numerical value of the energy of the state described by $\boldsymbol{\psi_i}$

We have to find the eigenfunctions ψ_i and corresponding eigenvalues E_i of Hamiltonian $\hat{H}$. Once the ψ_i are determined, all properties of interest can be obtained by applying the appropriate operators to the wave function. Unfortunately, this simple-looking program is of hardly any practical relevance, since apart from a few, trivial exceptions, no strategy to solve the Schrodinger equation exactly for atomic and molecular systems are known.

Nevertheless, the situation is not completely hopeless. There is a way for the systematically approaching the wave function of the ground state ψ_0, i. e. the state which delivers the lowest energy E_0. This is the *variational principle*, which holds a very prominent place in all quantum mechanical applications. The expectation value of a particular observable represented by the appropriate operator $\hat{O}$ for any wave function ψ given by according to the equation

$$\langle\hat{O}\rangle = \iint \boldsymbol{\psi}^* \, \hat{O} \, \boldsymbol{\psi} \, \boldsymbol{dx_1 dx_2} \ldots \ldots \boldsymbol{dx_N} = \langle\boldsymbol{\psi}|\hat{O}|\boldsymbol{\psi}\rangle, \qquad (2.10)$$

where ψ* indicates the complex-conjugate of ψ. $dx_1 dx_2 \dots \dots dx_N$ volume elements for the electrons 1, 2…… N.

The variational principle now states that the energy computed via equation (2.10) as the expectation value of the Hamiltonian operator Ĥ from any guessed ψ will be an upper bound to the true energy of the ground state, i. e.,

$$\langle \boldsymbol{\psi} | \widehat{\mathrm{H}} | \boldsymbol{\psi} \rangle = \boldsymbol{E} \geq \mathbf{E_0} = \langle \boldsymbol{\psi_0} | \widehat{H} | \boldsymbol{\psi_0} \rangle, \qquad (2.11)$$

where the equality holds if and only if ψ is identical to ψ_0.

Equations (2.10) and (2.11) for the first time encounter the main mathematical concept of density functional theory. A rule such as that given through equation (2.10) or (2.11), which assigns a number, e. g. , E to a function ψ, is called a functional. This is to be contrasted with the much more familiar concept of a function, which is the mapping of one number onto another number. In a different way, we can say that a functional is a function whose argument is itself a function. Thus, expectation values such as $\langle \hat{O} \rangle$ in equation (2.10) are obviously functionals, since the value of $\langle \hat{O} \rangle$ depends on the function ψ present.

In the variational principle, the strategy for finding the ground state energy and wave function is: one needs to minimize the functional E[ψ] by searching through all acceptable N-electron wave functions i. e. these wavefunctions should make physical sense. For example, to be eligible as a wavefunction, ψ must be continuous everywhere and be quadratically integrable. The function which gives the lowest energy will be ψ_0 and the energy will be the true ground state energy E_0 and this can be compactly expressed as

$$E_0 = \min_{\boldsymbol{\psi} \to \boldsymbol{N}} E[\boldsymbol{\psi}] = \min_{\boldsymbol{\psi} \to \boldsymbol{N}} \langle \boldsymbol{\psi} | \hat{T} + \hat{V}_{Ne} + \hat{V}_{ee} | \boldsymbol{\psi} \rangle, \qquad (2.12)$$

where ψ → N indicates that ψ is an allowed N-electron wave function. While such a search over all eligible functions is obviously not possible, we can apply the variational principle as well to a subset of all possible functions. One usually chooses these subsets such that the minimization in the equation (2.12) can be done in some algebraic scheme. The result will be the best approximation to the exact wave function that can be obtained from this particular subset. It is important to realize that by restricting the search to a subset the exact wave function itself cannot be identified (unless the exact wave function is included in the subset, which is rather improbable). The Hartree-Fock approximation discussed below, where the subset consists of all antisymmetric products (Slater determinants) composed of N spin orbitals solved this problem.

Hartree and Fock were the first, who derived a set of self-consistent, wave-functions based equation which allowed an iterative calculation of energy and other desired parameters of complex systems for which many-body Schrodinger equation was analytically not accessible. Up to some extent, the Hartree-Fock (HF) method is being intensively used in atomic and nuclear physics as well as in theoretical chemistry, but one of the most important negative point in the large computation time when large systems are investigated due to the dependency of the many-body wave function on 3N spatial variables. Therefore, to reduce the computational cost of molecular calculations, a less complex variable should be used that contains all information of all 3N spatial variables.

An approach to lower the computation time was first made by Hohenberg and Kohn (HK) in 1964, they proved that '*the electron density is the only variable depends on 3N spatial variable and in principle should contain all information about the ground state properties of a system'*. This leads to the *birth* of the density functional theory (DFT)[116], in which the electron density distribution plays a central role, rather than the many-electron wave function. In 1998, Kohn got Nobel prize in chemistry for his development of the density functional theory[116, 117].

In 1965, Kohn and Sham used the theoretical concept of Hohenberg and Kohn and derived a set of self-consistent, iteratively solvable equations in actual computer simulation[118]. Because of the fact that the electron density is much less complex quantity than the wave function, the computational time is lowered considerably.

Nowadays, DFT has become a popular technique for the calculation of ground state properties of interacting many-body electron systems such as atoms, molecules, or solids such as binding energy of molecules, the calculation of band structures of solids in physics, etc. The increasing demand for DFT can be seen in current research trends[40, 119, 120].

A major constituent of DFT is the choice of the correct approximation for the exchange-correlation which arises from the Kohn-Sham approach. The most widely used exchange-correlation functionals are *local density approximation* (LDA) and *generalized gradient approximation* (GGA). The former comes from the exchange-correlation functional of homogeneous electron gas by point to point mapping and the latter is a generalization of the former by including a contribution from electron density gradient. In order to better describe the correlation effect in some strongly correlated systems such as compounds with transition metals (3d electrons) and lanthanides (4f electrons), several extensions to LDA and GGA have been made including LDA+U, GGA+U, and dynamical mean field theory (DMFT), generally used as a combination of LDA and DMFT.

2.3.2 Basic of Density Functional Theory

DFT formulation now applies to any system of interacting particles in an external potential $V_{ext}(r)$, including any problem of electrons and fixed nuclei, where the Hamiltonian can be written as

$$\hat{H} = -\frac{\hbar}{2m_e}\sum_i \nabla_i^2 + \sum_i V_{ext}(r_i) + \frac{1}{2}\sum_{i\neq j}\frac{e^2}{|r_i - r_j|}, \tag{2.13}$$

where, r_i, r_j are the positions of the electrons and ħ, m_e, and e are the well-known fundamental constants.

DFT is simply based upon two theorems, illustrated as follows:

Theorem 1: For any system of interacting particles in an external potential $V_{ext}(\boldsymbol{r})$ is uniquely determined, upto a constant, by the ground state particle density; $n_0(\boldsymbol{r})$.

Theorem 2: The energy functional $E[n]$ can be defined in terms of the density $n(\boldsymbol{r})$ in an external potential $V_{ext}(\boldsymbol{r})$. For any $V_{ext}(\boldsymbol{r})$, the exact ground state energy of the system is the global minimum value of this functional and the density $n(\boldsymbol{r})$ that minimizes the functional is the exact ground state density $n_0(\boldsymbol{r})$.

2.3.3 Kohn-Sham Formulations

The Kohn-Sham formulation[118] is based on the mapping the full interacting system with the real potential, onto a fictitious non-interacting system whereby the electrons move within an effective ``Kohn-Sham" single-particle potential $V_{KS}(\boldsymbol{r})$. The Kohn-Sham method is still exact since it yields the same ground state density as the real system, but greatly facilitates the calculation. First consider the variation problem presented in the second Hohenberg-Kohn theorem - the ground state energy of a many-electron system can be obtained by minimizing the energy functional subject to the constraint that the number of electrons N is conserved, which leads to,

$$\delta[F[n(\boldsymbol{r}) + \int V_{ext}(\boldsymbol{r})n(\boldsymbol{r})dr \\ -\mu(\int n(\boldsymbol{r})d\boldsymbol{r} - N)] = 0, \qquad (2.27)$$

and the corresponding Euler equation is given by

$$\mu = \frac{\sigma F[n(\boldsymbol{r})]}{\sigma n(\boldsymbol{r})} + V_{ext}(\boldsymbol{r}), \qquad (2.28)$$

where $\mu$is the Lagrange multiplier associated with the constraint of constant N. The idea of Kohn and Sham was to set up a system where the kinetic energy could be determined exactly, since this was a major problem in Thomas-Fermi theory. This was achieved by invoking a non-interacting system of electrons. The corresponding ground state wave function ψ_{KS} for this type of system is given exactly by a determinant of single-particle orbital $\psi_i(\boldsymbol{r_i})$

$$\psi_{KS} = \frac{1}{\sqrt{\Gamma N}} det[\,\psi_1(\boldsymbol{r_1}) \ldots \ldots . \psi_N(\boldsymbol{r_N})], \qquad (2.29)$$

The universal functional F[n(**r**)] was then partitioned into three terms, the first two of which are known exactly and constitute most of the energy, the third being a small unknown quantity,

$$F[n(\boldsymbol{r})] = T_S[n(\boldsymbol{r})] + E_H[n(\boldsymbol{r})] + E_{XC}[n(\boldsymbol{r})], \qquad (2.30)$$

where $T_S[n(\boldsymbol{r})]$ is the kinetic energy of a non-interacting electron gas of density $n(\boldsymbol{r})$, $E_H[n(\boldsymbol{r})]$ is the classical electrostatic (Hartree) energy of the electrons,

$$E_H[n(\boldsymbol{r})] = \frac{1}{2} \frac{n(r)n(r')}{|r-\boldsymbol{r}'|} d\boldsymbol{r} d\boldsymbol{r}', \qquad (2.31)$$

and $E_{XC}[n(\boldsymbol{r})]$ is the exchange-correlation energy, which contains the difference between the exact and non-interacting kinetic energies. The non-classical contribution to the electron-electron interactions of which the exchange energy is a part of the system. In that case, the Kohn-Sham prescription the Euler equation given in (2.28) now becomes,

$$\mu = \frac{\delta T_S[n(\boldsymbol{r})]}{\delta n(\boldsymbol{r})} + V_{KS}(\boldsymbol{r}), \qquad (2.32)$$

where; the Kohn-Sham potential $V_{KS}(\boldsymbol{r})$ is given by,

$$V_{KS}(\boldsymbol{r}) = V_{XC}(\boldsymbol{r}) + V_H(\boldsymbol{r}) + V_{ext}(\boldsymbol{r}), \qquad (2.33)$$

with the Hartree potential $V_H(\boldsymbol{r})$,

$$V_H(\boldsymbol{r}) = \frac{\delta E_H[n(\boldsymbol{r})]}{\delta n(\boldsymbol{r})} = \int \frac{n(\boldsymbol{r}')}{|\boldsymbol{r}-\boldsymbol{r}'|} d\boldsymbol{r}', \tag{2.34}$$

and the exchange-correlation potential $V_{XC}(\boldsymbol{r})$,

$$V(\boldsymbol{r}) = \frac{\delta E_{XC}[n(\boldsymbol{r})]}{\delta n(\boldsymbol{r})}, \tag{2.35}$$

The crucial point to understand in Kohn-Sham theory is that is just a rearrangement, so the density obtained when solving the alternative non-interacting Kohn-Sham system is the same as the exact ground state density. The ground state density is obtained in practice by solving the N one-electron Schrödinger equations,

$$\left[-\frac{1}{2}\nabla^2 + V_{KS}(\boldsymbol{r})\right]\psi_i(\boldsymbol{r}) = \varepsilon_i\psi_i(\boldsymbol{r}), \tag{2.36}$$

where, ε_i are Lagrange multipliers corresponding to the ortho normal of the N single-particle states $\psi_i(\boldsymbol{r})$, and the density is constructed from,

$$n(\boldsymbol{r}) = \sum_{i=1}^{N} |\psi_i(\boldsymbol{r})|^2, \tag{2.37}$$

The non-interacting kinetic energy $T_S[n(r)]$ is therefore given by,

$$T_S[n(\boldsymbol{r})] = -\frac{1}{2}\sum_{i=1}^{N} \int \psi_{i=1}^{*} \int \psi_i^{*}\,(\boldsymbol{r})\nabla^2\psi_i(\boldsymbol{r})d\boldsymbol{r}, \tag{2.38}$$

Since $V_{KS}(\boldsymbol{r})$ depends on the density through the exchange-correlation potential, relations, which are known as the Kohn-Sham equations, must be solved self-consistently as in the Hartree- Fock scheme .In order to handle the kinetic energy in an exact manner, N equations have to be solved in Kohn-Sham theory to obtain the set of Lagrange multipliers ε_i as opposed to one equation that determines μ when solving for the density directly, as in the Thomas-Fermi approach. However, an advantage of the Kohn-Sham method is that as the complexity of a system increases, due to N increasing, the problem becomes no more difficult, only the number of single-particle equations to be solved increases. Although exact in principle, Kohn-Sham theory is approximate in practice because of the unknown exchange-correlation functions $E_{XC}[n(\boldsymbol{r})]$. An implicit definition of $E_{XC}[n(\boldsymbol{r})]$ can be given through (2.29), is as follows,

$$E_{XC}[n(\boldsymbol{r})] = T[n(\boldsymbol{r})] + E_{ee}[n(\boldsymbol{r})] - T_S[n(\boldsymbol{r})] - E_H[n(\boldsymbol{r})], \qquad (2.39)$$

where $T[n(\boldsymbol{r})]$ and $E_{ee}[n(\boldsymbol{r})]$ are the exact kinetic and electron-electron interaction energies respectively. The intention of Kohn and Sham was to make the unknown contribution to the total energy of the non-interacting system as small as possible, and this is indeed the case with the exchange-correlation energies; however, it is still an important contribution since the binding energy of many systems is about the same size as $E_{XC}[n(r)]$, so an accurate description of exchange and correlation is crucial for the prediction of binding properties. Present approximations for the exchange-correlation energy are far from satisfaction; consequently, the development of improved exchange-correlation functional is essential. An in-depth discussion of the exact properties of $E_{XC}[n(r)]$.

2.3.4 Exchange-correlation Functional

Now since DFT is the most widely used method for predicting the electronic structure possibly because of the success of exchange-correlation (approximate) functionals. The crucial quantity in the Kohn-Sham approach is the exchange-correlation energy which is expressed as a functional of density $E_{XC}[n(\boldsymbol{r})]$. In this section, we will discuss relevant approximate functionals, in particular, two basic methods, the local density approximation (LDA) and generalized gradient approximation (GGA).

Local Density Approximation (LDA)

To make DFT applicable in practical problems the important type of approximation for the exchange-correlation density functional is the LDA, which was proposed by Hohenberg and Kohn in their original DFT paper[116]. The LDA is only dependent on the local density, and the total energy. The most commonly used and successful approximation is the LDA, first formulated by Kohn and Sham in 1965[118]. The LDA locally approximate the true exchange-correlation energy of a system by the exchange-correlation energy associated with a homogeneous electron gas of the same density. The homogeneous gas is the only system for which the form of the exchange-correlation energy is known precisely. The LDA uses the exchange-correlation energy of the homogeneous electron gas, evaluated from the charge density at the point r under consideration. Effectively at r, $n = n(\boldsymbol{r})$ and E_{xc} is equal to the exchange-correlation energy for the electron-gas system which has a homogeneous charge density n. This is valid if the in homogeneity of $n(\boldsymbol{r})$ is small, but the main approximation of LDA is that this is applied even if the in homogeneity is large. If the electron kinetic energy is written as $T[n(\boldsymbol{r})]$ then in the LDA the universal functional is given by (note that atomic units are used throughout this section):

$$F[n(\boldsymbol{r})] = T[n(\boldsymbol{r})] + \frac{1}{2}\int \frac{n(\boldsymbol{r})n(\boldsymbol{r}')}{|\boldsymbol{r}-\boldsymbol{r}'|} + E_{xc}^{LDA}[n(\boldsymbol{r})], \qquad (2.40)$$

where, $E_{xc}^{LDA}[n(\boldsymbol{r})]$ is the exchange-correlation energy functional for local-density approximation and is given as

$$E_{xc}^{LDA}[n(\boldsymbol{r})] = \int n(\boldsymbol{r})\epsilon_{xc}(n)\partial\boldsymbol{r}, \qquad (2.41)$$

where; $\epsilon_{xc}[n]$ is the exchange and correlation energy per particle of a uniform electron gas of density n.

By applying the variation principle to the equation, with the constraint that for an N electron system $\int n(\boldsymbol{r})\partial\boldsymbol{r} = N$, the following equation is obtained:

$$\int \delta n(\boldsymbol{r})\{\frac{\delta T[n]}{\delta n(\boldsymbol{r})} + V(r) + \int \frac{n(\boldsymbol{r}')}{|\boldsymbol{r}-\boldsymbol{r}'|}\partial r' + \frac{\delta Exc}{\delta n(\boldsymbol{r})} - \mu\}\partial\boldsymbol{r} = 0, \quad (2.42)$$

where; μ is the Lagrangian multiplier equivalent to the chemical potential. The solution of the equation is then given by solving the following effective one-electron Schrödinger equation for Ψ_λ:

$$\left\{-\frac{1}{2}\Delta^2 + V(r) + \int \frac{n(r')}{|r-r'|}\partial r' + \frac{\delta E_{XC}}{\delta n(r)}\right\}\Psi_\lambda(r) = E_\lambda \Psi_\lambda(r), \quad (2.43)$$

where, E_λ is the energy eigen value of the λ^{th} state. This equation is called the Kohn-Sham equation and the eigen values are usually identified as the one-electron energy levels (this is an approximation due to LDA's deviation from the real result for states far below the Fermi level). If the equation is solved self-consistently then the solutions, Ψ_λ will be related to the electron charge density and kinetic energy density via equations, but the Slater determinant constructed from Ψ_λ is not the true many-electron HF wave function. Ψ_λ is not the same as the one-electron wave functions in the Hartree-Fock approximation but are more directly related to the true electronic charge density.

Generalized Gradient Approximation (GGA)

Hohenberg and Kohn presumed that the LDA would be too simplistic to work for real systems and so proposed an extension to the LDA known as the gradient expansion approximation (GEA). The GEA is a series expansion of increasingly higher order density gradient terms. The first order form of the GEA was subsequently implemented and tested for atoms and molecules and was a complete failure. The source of the GEA problems was later found to be caused by the violation of the sum rule and the non-positivity constraint on the exchange hole both of which are important physical conditions that happen to be fulfilled by the LDA. Despite the disappointing results, the GEA provided the basis for the generalized gradient approximation (GGA) which is currently the most popular exchange-correlation functional in condensed matter physics. The vital steps that lead to the GGA were principally made by Perdew and co-workers who devised a cutoff procedure that sharply terminates the GEA exchange-correlation hole in real-space using delta functions to restore the sum rule and non-positivity hole conditions. As the LDA approximates the energy of the true density by the energy of a local constant density, it fails in situations where the density undergoes rapid changes such as in molecules. An improvement to this can be made by considering the gradient of the electron density, the so-called Generalized Gradient Approximation (GGA). Symbolically this can be written as

$$E_{xc}^{LDA} = E_{XC}[\rho(r), \mathit{\Delta}\rho(r)], \tag{2.44}$$

This can lead to a large improvement over LDA results with accuracy approaching that of correlated wave function methods such as MP2 and in some cases surpassing these while there is only one LDA, there are several different parameterizations of the GGA. Some of these are semi-empirical, in that experimental data (e.g. atomization energies) is used in their derivation. Others are found entirely from first principles. A commonly used functional is the PW91 functional, due to Perdew and Yang.

In physics, the most widely used approximation is the LDA, where the functional depends only on the density at the coordinate where the functional is evaluated as

$$E_{XC}[n] = \int \varepsilon_{xc}(n) n(r)\, \partial^3 r, \tag{2.45}$$

The local spin-density approximation (LSDA) is a straightforward generalization of the LDA to include electron spin

$$E_{xc}^{LSDA}[n_{\uparrow}, n_{\downarrow}] = \int \varepsilon_{xc}(n_{\uparrow,} n_{\downarrow})n(r)\partial^3 r, \tag{2.46}$$

Highly accurate formulae for the exchange-correlation energy density $\varepsilon_{XC}(n_{\uparrow,}n_{\downarrow})$ have been constructed from quantum Monte Carlo simulations of a free electron model. Generalized gradient approximations (GGA) are still local but also take into account the gradient of the density at the same coordinate:

$$E_{xc}^{GGA}[n_{\uparrow}, n_{\downarrow}] = \int \varepsilon_{xc}\,(n_{\uparrow}, n_{\downarrow}, \Delta n_{\uparrow}, \Delta n_{\downarrow})n(r)\partial^3 r, \tag{2.47}$$

Using the latter (GGA) also good results for molecular geometries and ground-state energies have been achieved. These functional include a further term in the expansion, depending on the density, the gradient of the density and the Laplacian (second derivative) of the density. Difficulties in expressing the exchange part of the energy can be relieved by including a component of the exact exchange energy calculated from Hartree- Fock theory. Functional of this type are known as hybrid functionals.

DFT has been used widely in both physics and chemistry. In both fields, DFT has proved very useful for broad classes of systems and often leads to important practical results. It often provides clues of how our present understanding of electronic structure in real space coordinates needs to be modified. It offers a nice scaling of computational cost with size and allows calculations to be performed on large and complex systems. DFT introduced by Hohenberg-Kohn together with the approach by Kohn-Sham are exact and thus allow an exact solution provided that the functional $E_{XC}[n(\boldsymbol{r})]$ is known exactly known. But, in practice this never the case, which reveals the point in DFT. An approach of calculation in DFT stands and falls with the quality of the approximation.

In this research work, the first principle calculations have been carried out again using the full-potential linearized augmented plane wave (FP-LAPW) method within the density-functional theory (DFT)[116, 118].

Structural Optimization using DFT

To optimize the structure, a full-potential linearized augmented plane wave (FPLAPW) calculations within the framework of density functional theory [118, 121] have been performed using WIEN2k code[122]. The PBE parameterization of generalized gradient approximation (GGA) [123] has been used as an exchange-correlation potential. The basic function has been expanded up to $R_{MT}K_{max} = 9$, where, R_{MT} is the muffin tin radius and K_{max} is the plane wave cut off parameter. The R_{MT} values selected as 2.11 Bohr for R, 1.90 Bohr for Fe and 1.65 Bohr for O. $6 \times 6 \times 6$ k points were taken in the calculation. The self-consistent calculations were run until the energy convergence criterion 10^{-4} Ry/cell reached. For orthorhombic systems optimizations were achieved by calculating the ground energies for different values of b/a, c/a, and volume and selecting the combination that had the lowest energy. Structural optimizations of orthorhombic $RFeO_3$ were performed by varying c/a with constant b/a ratio and volume. Then we vary the ratio c/a between -10% to 10% of its initial value with a step of 2%. Similarly, we have optimized the ratio b/a with constant c/a ratio and volume.

The Methodology used for Electronic and Magnetic Calculations

The generalized gradient approximation (Predew-Burke-Ernzerhof) (GGA-PBE)[123] has been used as an exchange-correlation potential as implemented in WIEN2k package[122]. As the standard GGA-PBE approximation underestimates the bandgap and shows $RFeO_3$ systems as metallic, we have used GGA with strong Coulomb interaction (GGA+U), introduced by Anisimov et al[124], U = 4.0 eV was taken into consideration to treat Fe-3d electrons for self-interaction correction. The cut-off energy is set to -6 Ry to separate core states from valance states. The k-mesh size in the first Brillouin zone was 11 x 11 x 7 have been used. The basic function has expanded up to $R_{MT}K_{max} = 7$, where, R_{MT} is the muffin tin radius and K_{max} is the plane wave cut off parameter. The R_{MT} values of Y, Fe, and O atomic spheres are set to 2.11, 1.90, and 1.65 Bohr respectively. The self-consistent calculations were considered to be converged only when the absolute charge density difference per formula unit between the successive loops is less than 0.0001|e|, where 'e' is the electron charge.

To investigate the electronic structure, spin-polarized ferromagnetic (FM) calculations were performed taking unit cell into account, containing 20 atoms per formula unit of $RFeO_3$ samples. The magnetic investigations were made in two configurations, a complete ferromagnetic (FM) and an antiferromagnetic (AFM) orientation between the Fe and their neighbors Fe atoms and after that AFM arrangement has been taken to generate the various defect models. [122]. A supercell of size 3×1×1 containing 60 atoms was used to create Y, Fe, and O-defect models of orthorhombic $YFeO_3$ in our calculations. The formation energy of defect X with charge q depends on the Fermi energy and is calculated using equation [125-127] below

$$E_f(X^q) = E^{total}(X^q) - E^{total}(bulk) - \sum_i n_i\mu_i + q(E_F + E_v + \Delta V), \qquad (2.48)$$

where, E^{total} $(X^q)$is the total energy derived from a supercell with defect X, E^{total} (bulk) is the total energy of the defect-free supercell, n_i is the number of atoms of species i that have been added ($n_i>0$) or removed ($n_i<0$) upon defect creation and μ_i are the corresponding chemical potentials. E_F is the Fermi level with respect to the bulk valence band maxima E_v and ΔV is the reference potential in the defect supercell with that in bulk. The chemical potential energy μ_i depends on the preparation conditions[126]. Since we have considered the neutral defect (q=0), so the equation (2.48) becomes

$$E_f(X^q) = E^{total}(X^q) - E^{total}(bulk) - \sum_i n_i\mu_i, \qquad (2.49)$$

In order to understand the large value of magnetic moment in self-doped $YFeO_3$, we performed the Bader charge analysis using Critic2 code[128, 129] with QTREE algorithm[130] based on Bader's Atoms in Molecules (AIM) theory[131] for the electron charge distribution of Y, Fe and O-defect models from the electron density results of WIEN2k package. In this method, each atom of a crystal is surrounded by an effective surface that runs through minima of the charge density and the total charge of an atom, the so-called Bader charge is determined by integration within this region. These analyses enable us to examine the charge distributions on different atoms and their deviations from the formal one due to defects and to discuss some parameters like magnetic moments from the calculated data.

2.4 Bond Valence Sum (BVS)

Structural Optimization has also been done by using Bond valence sum (BVS) approach. The concept of bond valence has been widely used in solid-state sciences. This approximation is based on the fact that 'the bond length is a unique function of bond valence'. Thus, it provides a powerful method for the prediction and interpretation of bond lengths in crystals[132, 133]. The program used (SPuDS)[134] requires only the composition and oxidation state of each ion as its input. To optimize the structure, it requires determination of the unit-cell dimensions and all free positional parameters. SPuDS restrict the octahedra to remain rigid, i. e. it fixes six equivalent B-O distances and all O-B-O angles to 90° in ABO_3 type structure in order to minimize the input variables and simplify the process. The size of the octahedron and the optimum magnitude of the octahedra tilting distortion is calculated utilizing the bond-valence model. In bond valence, the overall structural stability is determined by comparing the calculated bond-valence sums with the ideal formal valences [135]. This quantity is referred to as the global instability index (GII) and is calculated according to the equation below

$$GII = \left\{\frac{\left[\sum_{i=1}^{N} d_i^2\right]}{N}\right\}, \qquad (2.50)$$

The variables involved in equation (2.50) are the discrepancy factor (d_i) and N, which is the number of atoms in the asymmetric unit. Here 'd_i' is the discrepancy factor is a measure of the lattice strains present in the compound. The discrepancy factor can be calculated according to the equation below

$$d_i = V_{i(ox)} - V_{i(calc)}, \qquad (2.51)$$

here, $V_{i(ox)}$ is the formal valence and $V_{i(calc)}$ is the calculated bond-valence sum for the ith ion. In ABX_3 type perovskites, the atomic valences, $V_{i(calc)}$, of the A and B cations, and X anion are calculated according to equation (2.52) by summing the individual bond valences $\boldsymbol{S_{ij}}$ about each ion

$$V_{i(calc)} = \sum_j S_{ij}, \qquad (2.52)$$

where, S_{ij} is the bond valence, associated with each cation-anion interaction, is calculated using the equation below

$$S_{ij} = e^{\left[\left(R_{ij} - d_{ij}\right)/B\right]}, \qquad (2.53)$$

where 'd_{ij}' is the cation-anion distance. The parameter B and R_{ij} are empirically determined for each cation-anion pair based upon a large number of well-determined bond distances for the cation-anion pair.

Chapter 3

Synthesis and Structural Characterization of Rare-earth Orthoferrites

In this chapter, details about the synthesis of rare-earth orthoferrites (RFeO$_3$) and its structural properties in terms of Fe-O-Fe bond angles, Fe-Fe near-neighbour distances (NND), R-O bond lengths, Fe-O bond lengths, and FeO$_6$ octahedra distortions, etc. have been provided. Because various physical properties such as ferroelectricity, magnetism, optical, etc. are critically controlled by these parameters. A necessary transformation matrix to estimate the tilt angles associated with FeO$_6$ octahedra using oxygen Wyckoff positions have been demonstrated in detail. The details of differential scanning calorimetry (DSC) measurements have also been provided. DSC measurements were performed to explore the variation of Neel temperature with structural parameters of RFeO$_3$ samples[1].

3.1 Introduction

Recently, RFeO$_3$ perovskites have attracted the attention of the scientific community worldwide due to the coexistence of electric and magnetic polarization in these materials[28, 29, 41-43]. At room temperature, rare-earth orthoferrites (RFeO$_3$) are known to acquire an orthorhombic crystal structure with space group Pbnm [58-61]. This orthorhombic structure of RFeO$_3$ can be derived from the rotation or tilts

---

[1] ***M. Kamal Warshi et al. Advances in Materials and Processing Technology, (2018), 1-15.***

of FeO_6 octahedra of an ideal cubic Pm3m perovskite structure, where this tilt can be tuned by the ionic radius of the rare earth cations R or by doping at Fe site. The existence of electric polarization in $RFeO_3$ samples which possess a centrosymmetric space group (Pbnm) is an interesting phenomenon because it requires a space group with a non-centrosymmetric point of inversion.

The $RFeO_3$ compounds have been investigated for years, because of its astonishing magnetic properties [49, 60, 136-139]. All members of the $RFeO_3$ family known possess a canted antiferromagnetic structure arising from spins of the Fe^{3+} ions [47, 48]. The antiferromagnetic ordering of the iron ions occurs at Neel temperature (T_N) between 650K and 750K. Several orthoferrites have shown a spin reorientation at lower temperatures [49-52]. $RFeO_3$ is again retrieving interest of researchers because of their fast spin dynamics [52-54], electric field control of magnetization and vice versa [55, 56], etc. Another interest is the possible application of these materials in devices because some of these compounds have recently shown to exhibit spontaneous electric polarization[41], which makes them multiferroic[28, 29] possibly due to their magnetic structure[12, 57].

Although the vast amount of activities has been dedicated to these compounds, some key features of these compounds are still remaining to be understood. The important characteristic of ABO_3 perovskites is the coupling of their various ferroic properties with the atomic structure, i.e. many of the properties can directly be modified by changing the rotation and distortion of the BO_6 octahedra. This directly affects the B-O-B bond angles and B-O bond lengths. In fact, the tilts and distortions of BO_6 octahedra in these ABO_3 perovskites are the key to control various physical properties such as weak-ferromagnetism [79, 140-143]. Thus, to understand the physics and related properties of $RFeO_3$ systems, it is very important to examine the evolution of structural characteristics like lattice constants a, b, and c, Fe-O bond lengths, Fe-O-Fe bond angles, FeO_6 octahedral tilts with R-site ionic radius. The structural distortion parameters of these samples have been calculated with great accuracy. Here, it is important to note that the rotation of FeO_6 octahedra i.e. tilt angles ϕ along (001) direction and θ along (110) direction may be estimated using lattice constants and through the atomic coordinates of oxygen anions. Amongst these, the estimation of tilt angles ϕ and θ through the oxygen coordinates is reported to be more accurate [144, 145]. Due to the presence of low 'Z' element i.e. oxygen in $RFeO_3$ perovskite oxides, the measured values of Fe-O bond lengths and tilts associated with FeO_6 octahedra may have a large error (in case the diffraction data is collected using low power x-ray lab source). This is due to the low value of the atomic scattering factor associated with oxygen. The neutron diffraction measurements or high intense (high flux) synchrotron-based x-ray diffraction measurements may be useful in this regard. Further, actual estimation of above-mentioned tilt angles, require necessary transformation and mathematical calculation. Keeping this in view, here it is aimed to present a detailed mathematical process for estimating these tilt angles ϕ and θ using oxygen coordinates. For this purpose, pure phase polycrystalline samples of $RFeO_3$ family have been prepared using the sol-gel method and structural properties studied using synchrotron-based XRD experiments. Using this diffraction data; tilts, bond angles, and bond lengths associated with FeO_6 octahedra have been estimated.

3.2 Experimental Detail

3.2.1 Synthesis of Rare-earth Orthoferrites

The sol-gel synthesis method was used to synthesize the series of $RFeO_3$ samples. The detail of method and procedure followed had discussed in chapter 2, section 2.1.1.

3.2.2 X-Ray Diffraction

SPXRD experiment was carried out at BL-12 ADXRD beamline at Indus-2, Synchrotron Radiation Source (Raja Ramanna Centre for advanced Technology Indore) [146]. The energy of the incident x-ray beam was 15 keV. The diffraction pattern recorded in the 2θ range of 10-50^o with the step size of 0.01^o using Huber six-circle diffractometer (model: 5020). All obtained diffraction patterns have been analyzed by using the FullProf [147] suite. The VESTA [148] software was used for visualization of the crystal structure of the refined pattern. In order to further understand the experimental results, the structural optimization of $RFeO_3$ has been done using DFT and BVS. The details of optimization process have been given in chapter 2, section 2.3 and 2.4.

3.2.3 Thermal Analysis

Differential scanning calorimetry (DSC) measurement was performed by using DSC 214 Polyma from NETZSCH in a temperature of 115K-770K at the rate of 10K/min in the N_2 environment for all prepared $RFeO_3$ samples.

3.3 Results and Discussions

3.3.1 Structural Properties of $RFeO_3$ *via* X-Rays Diffraction

In Figure 3.1(a) the SPXRD pattern of the as-synthesized $RFeO_3$ samples have been shown. SPXRD patterns reveal that $RFeO_3$ samples were synthesized in pure phase and there is no impurity present in these samples. Rietveld refinements of SPXRD data of all $RFeO_3$ samples have been done to calculate the structural parameters like lattice constants, bond lengths, bond angles, etc. All compounds of $RFeO_3$ were indexed using orthorhombic crystal structure with space group Pbnm. A representative Rietveld refined SPXRD pattern is shown in Figure 3.1(b). Inset of Figure 3.1(b) shows a magnified view to highlight the quality of fittings.

The structural parameters like lattice constants, cell volumes, Goldschmidt tolerance factors, Fe-O bond lengths, Fe-O-Fe bond angles, and Fe-Fe NND extracted from the Rietveld refinements of XRD data of $RFeO_3$ samples and their evolutions with increasing ionic radius of R-site ions of $RFeO_3$ samples has been shown in Figure 3.2 (a)-(f). The lattice constants (a, b, and c), cell volumes (V), Goldschmidt tolerance factors (t), R-O bond lengths, Fe-O-Fe bond angles, and Fe-Fe NND observed to be varied linearly, while Fe-O bond lengths found constant as function of ionic radius of R-site ions of $RFeO_3$ samples, i. e. Fe-O bond length found unaffected throughout the series of $RFeO_3$ with the replacement of R ions.

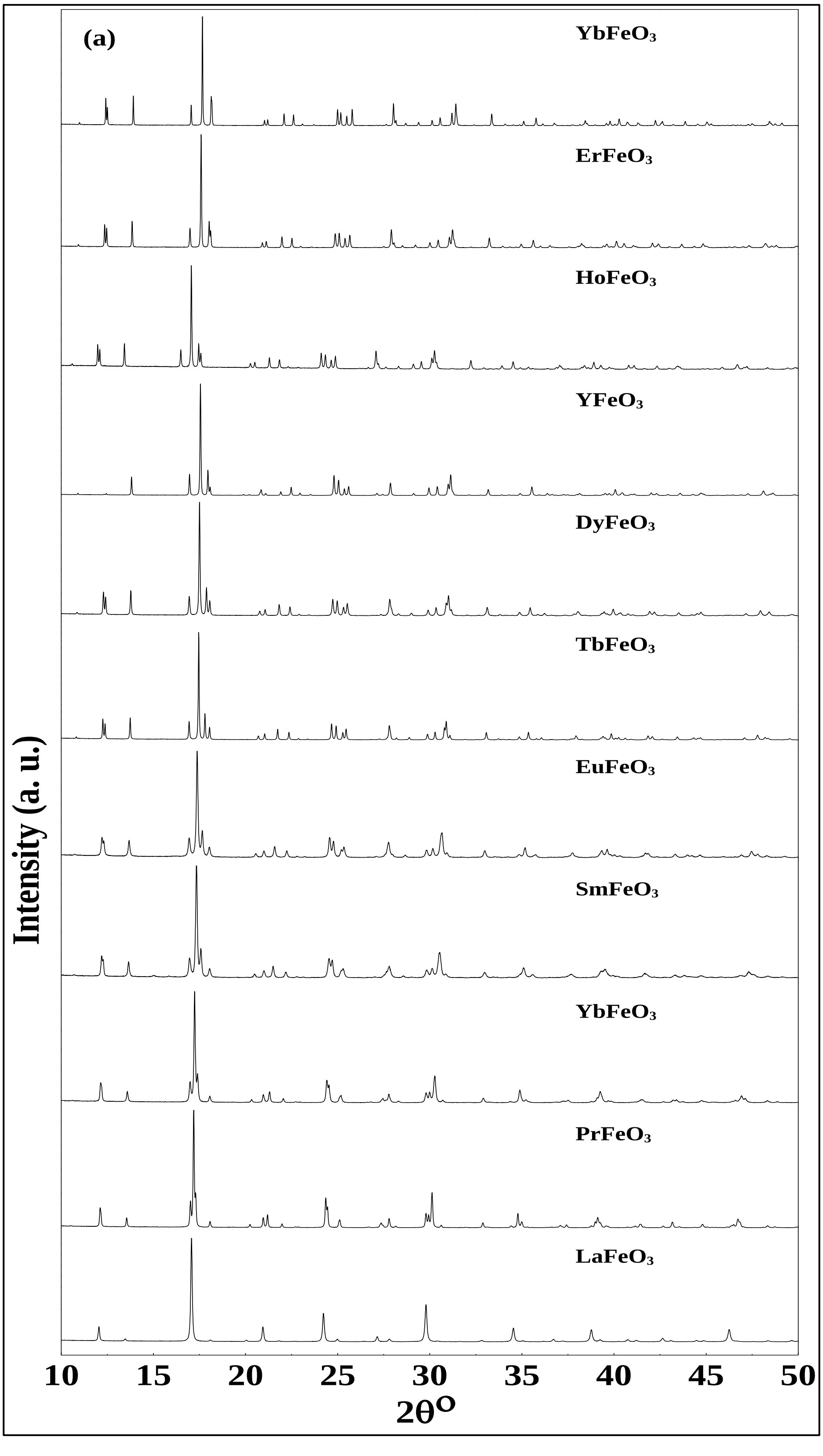

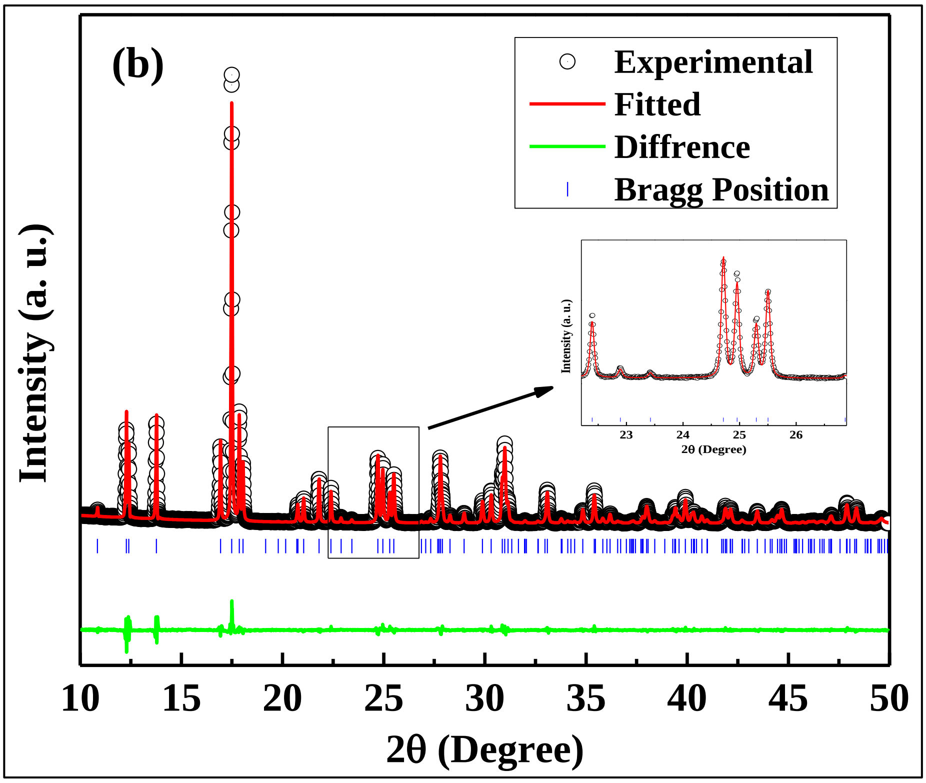

Figure 3.1: *(a) SPXRD data for $RFeO_3$ samples. (b) A representative Rietveld refined SPXRD pattern for $DyFeO_3$, the inset shows the quality of fit.*

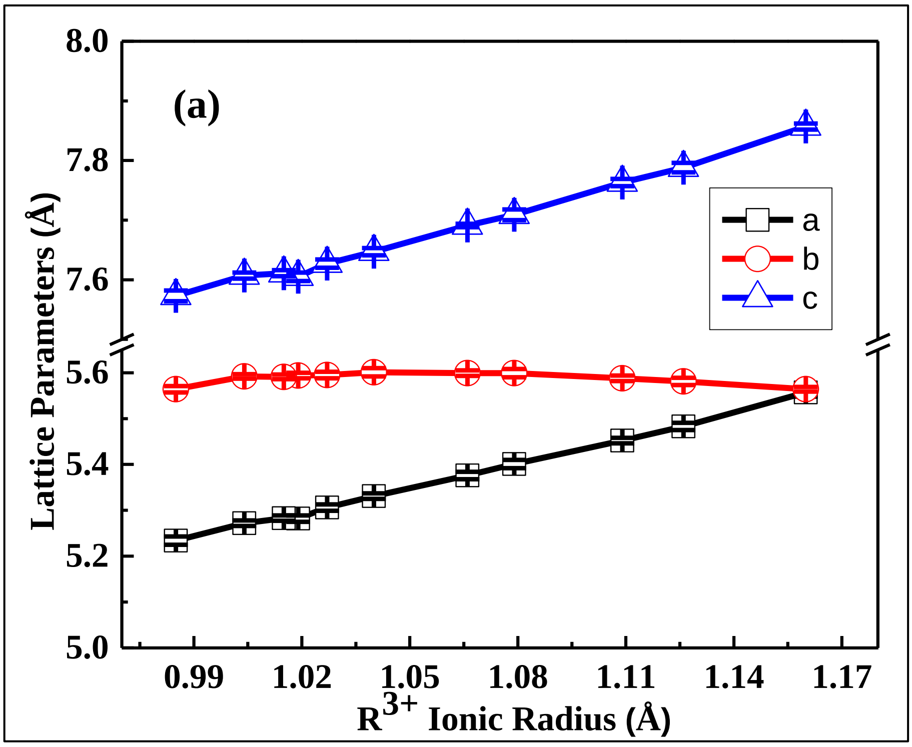

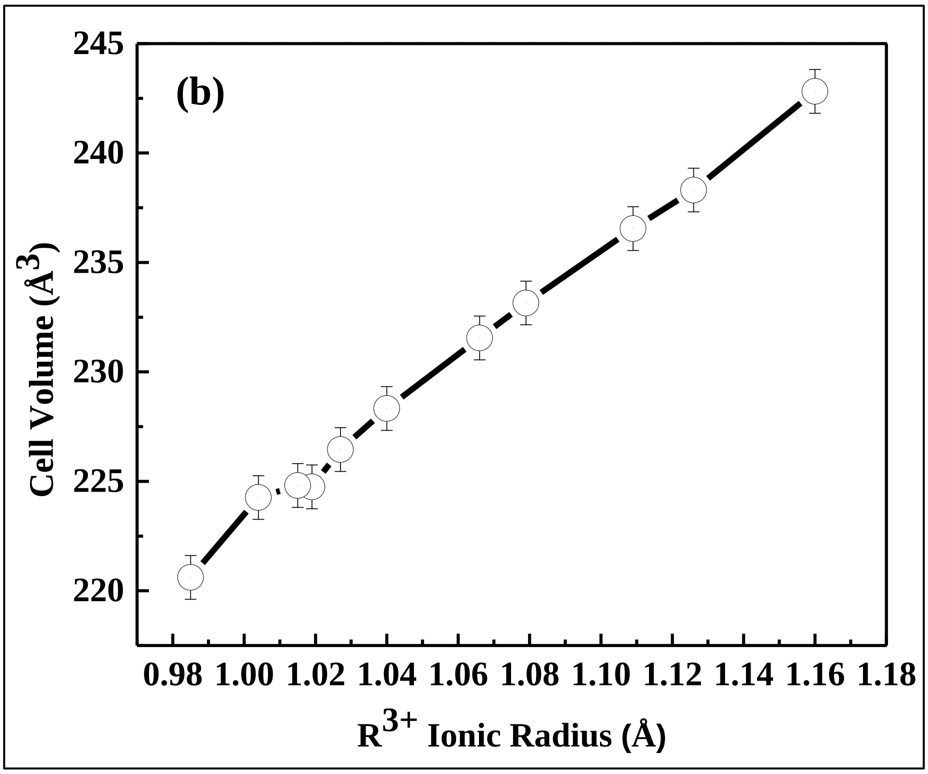

(b)
245
240
235
230
225
220
Cell Volume ($\AA^3$)
0.98
1.00
1.02
1.04
1.06
1.08
1.10
1.12
1.14
1.16
1.18
R^{3+} Ionic Radius (Å)

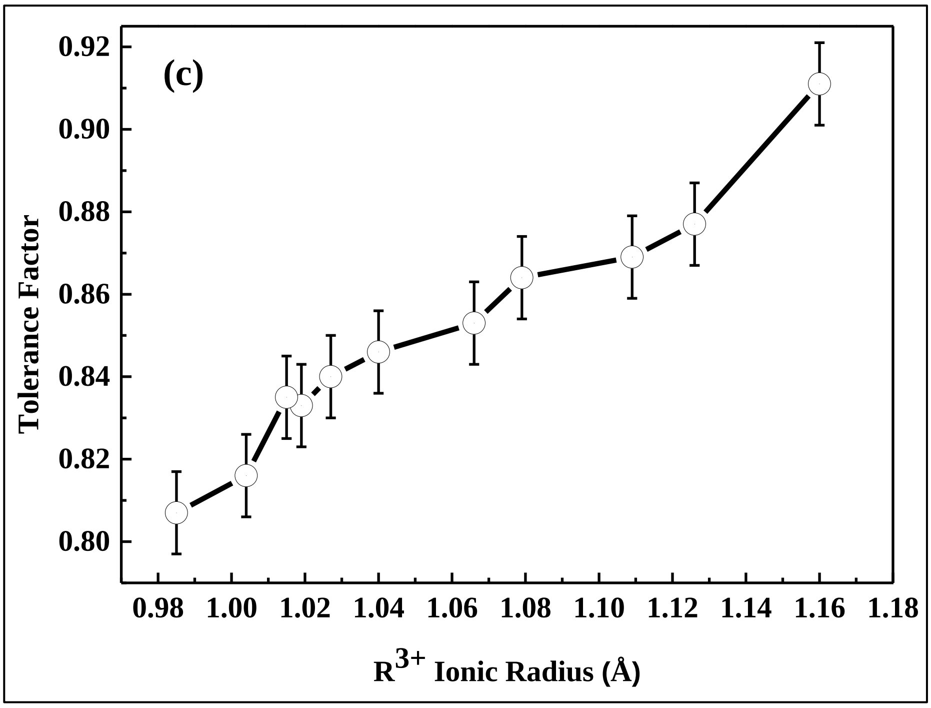

(c)
0.92
0.90
0.88
0.86
0.84
0.82
0.80
Tolerance Factor
0.98
1.00
1.02
1.04
1.06
1.08
1.10
1.12
1.14
1.16
1.18
R^{3+} Ionic Radius (Å)

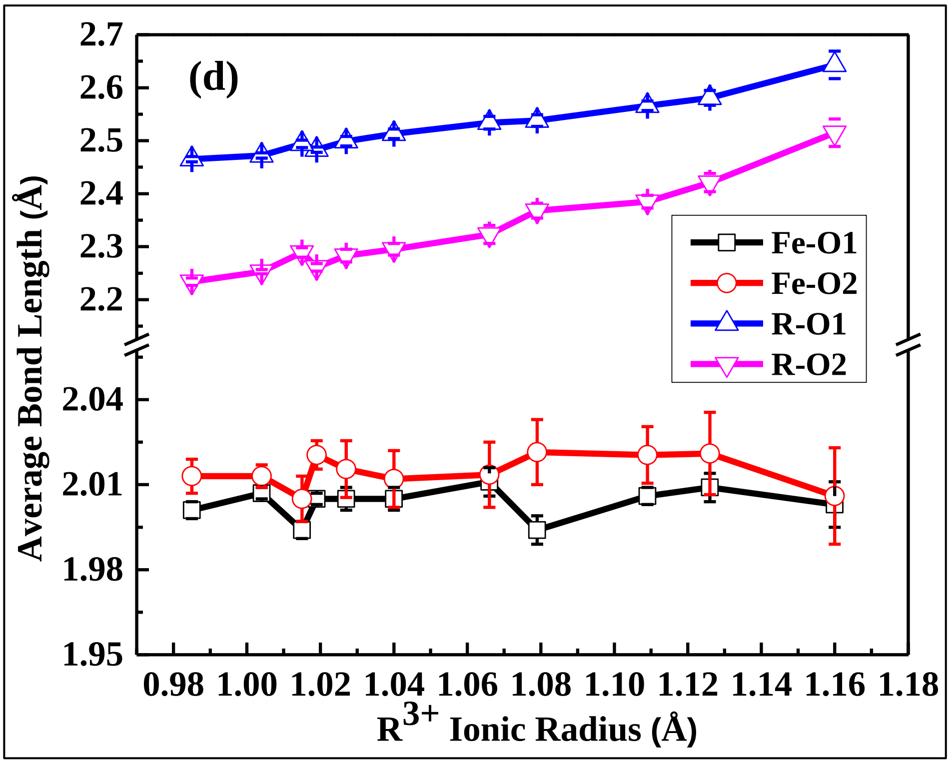
(d)
Average Bond Length (Å)
2.7
2.6
2.5
2.4
2.3
2.2
2.04
2.01
1.98
1.95
0.98
1.00
1.02
1.04
1.06
1.08
1.10
1.12
1.14
1.16
1.18
R3+ Ionic Radius (Å)
Fe-O1
Fe-O2
R-O1
R-O2

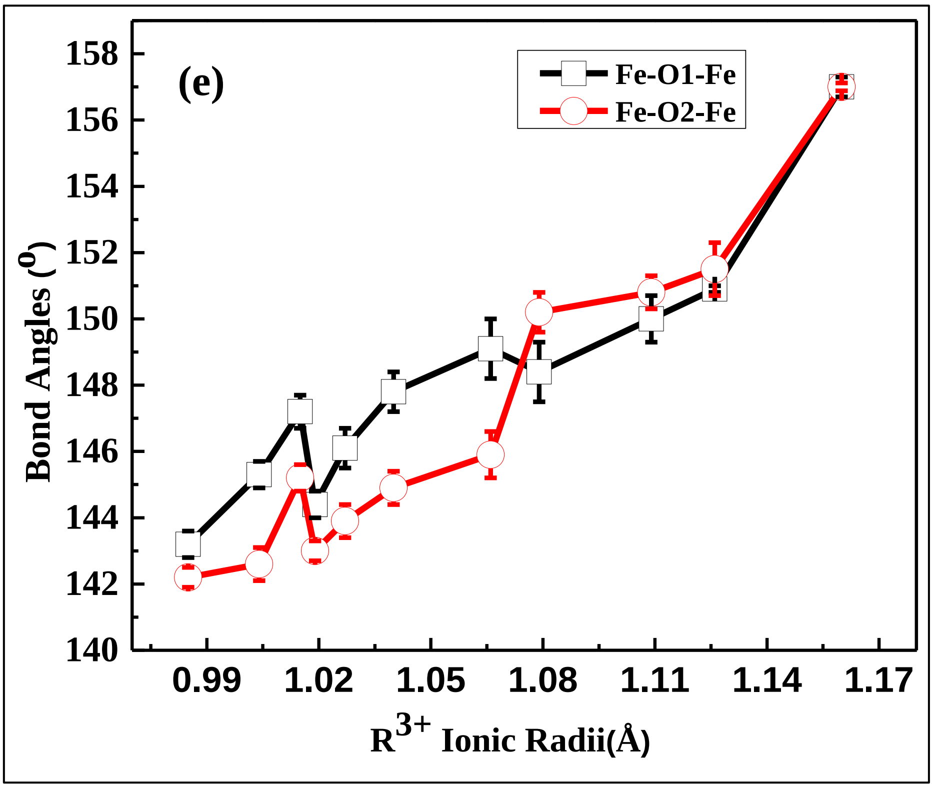
(e)
Bond Angles (0)
158
156
154
152
150
148
146
144
142
140
0.99
1.02
1.05
1.08
1.11
1.14
1.17
R3+ Ionic Radii(Å)
Fe-O1-Fe
Fe-O2-Fe

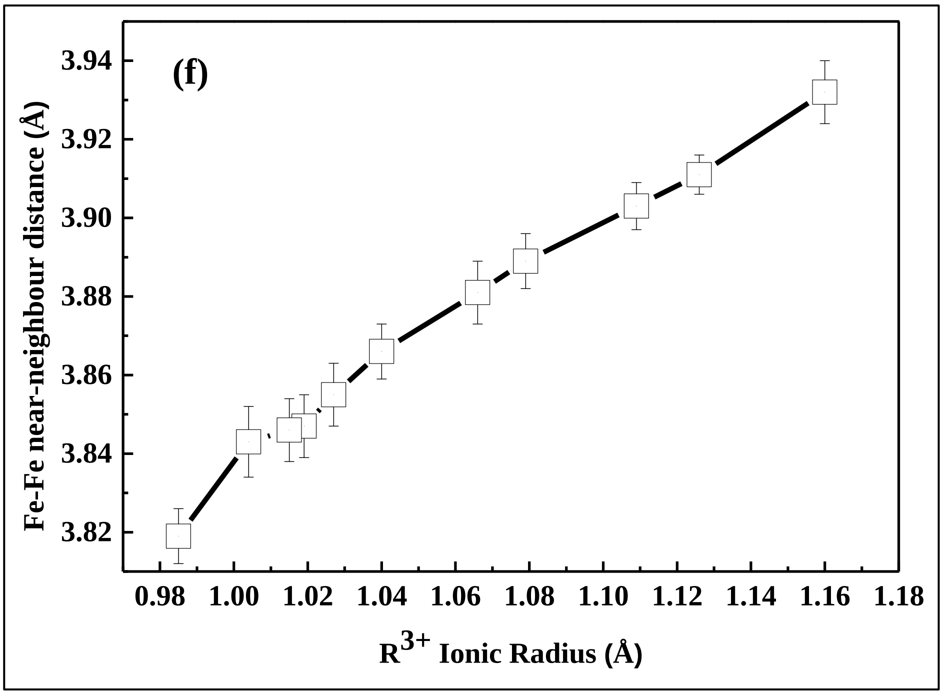

Figure 3.2: *(a)Variation of lattice constants, (b) cell volume, (c) tolerance factor, (d) Fe-O and R-O bond lengths, (f) Fe-O-Fe bond angles, (f) Fe-Fe NND as a function of ionic radii of rare earth elements of* $RFeO_3$ *compounds.*

In order to understand the effect of R site ionic radius on the structural distortions particularly in terms of octahedra tilts, the lattice constants and Wyckoff positions were used to find the distortions along (100) and (001) axes of basic cubic perovskite structure based on the formalism reported by Zhao et al [144]. In Glazer's notation the octahedra tilt of Pbnm system is expressed as $a^{-} a^{-} c^{+}$ [149] or in pseudo-cubic settings it is known as rotations by angles θ, ϕ, and Φ around the (110), (001), and (111) axes, respectively [17].

Figure 3.3(a) shows the undistorted ABO_3 type cubic perovskite unit cell with A-site cation at the corners and B-site cation at the center surrounded by six oxygen atoms to form the iron-oxygen (FeO_6) octahedra. The rotation of oxygen octahedra about the three cubic axes (100), (010), and (111) by the angles θ, ϕ, and Φ, respectively, can accommodate the deviations from this basic structure, as shown in Figure 3.3(b). To maintain corner connectivity, adjacent octahedra must rotate as well, which reduces the symmetry. In Figure 3.3(c), the orthorhombic pseudo-cubic unit cell is shown, which has been constructed with the several undistorted cubic perovskites, in which the orthorhombic main axes (100) coincide with the (110) cubic axes, and the (001) is parallel to the (001) cubic axis. The schematic for the various octahedral rotations observed in ideal cubic ABO_3 type perovskite have been expressed as rotation θ along (110), ϕ along (001) and Φ along (111). The angle Φ can be then expressed as $\cos\Phi = \cos\theta\cos\phi$.

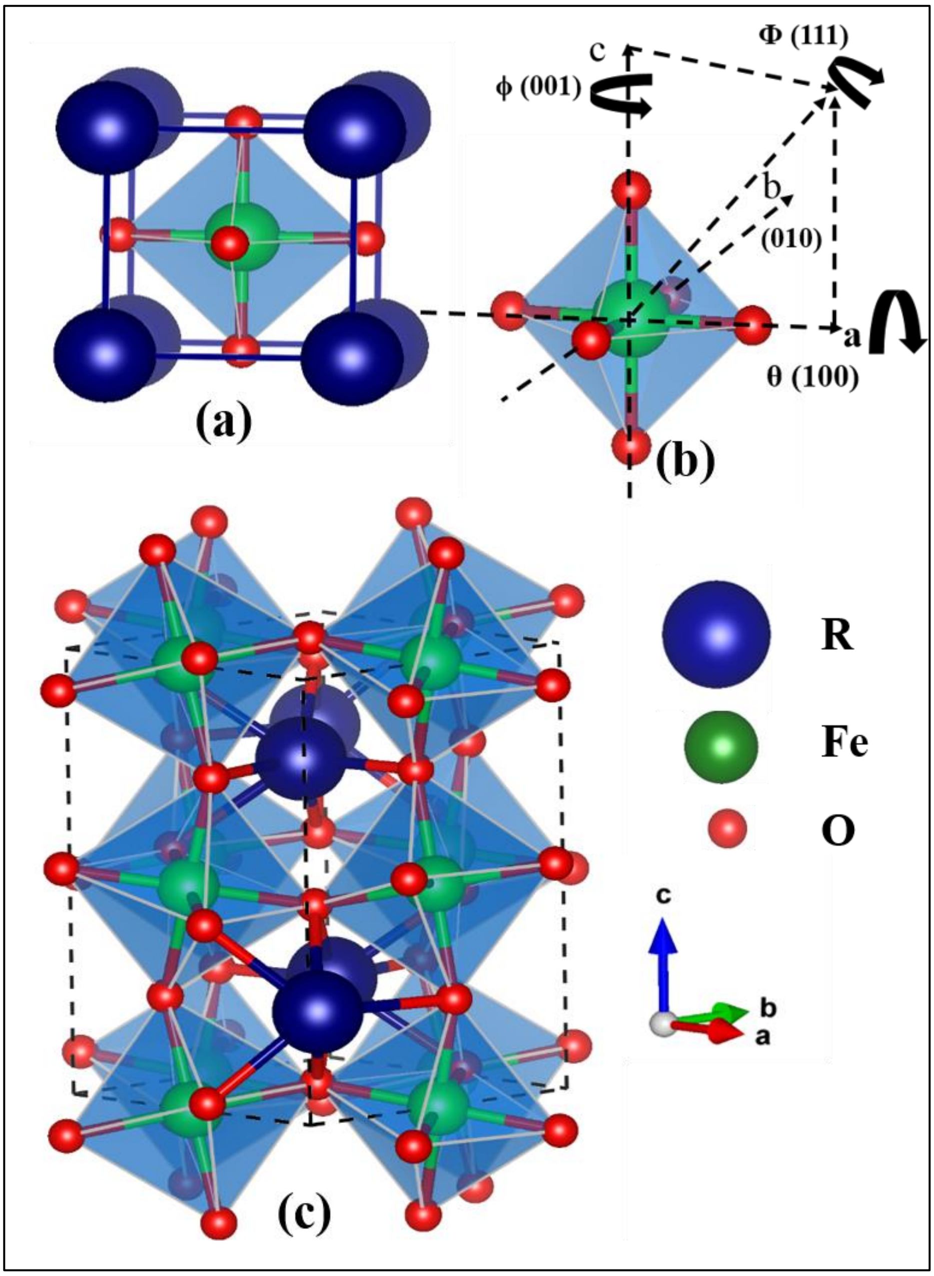

Figure 3.3: *(a) Schematic view of the crystal structure of ideal cubic perovskite ABO_3 (b) showing the octahedral rotation along ϕ (001), θ (110), and Φ (111) axes of regular octahedra (c) orthorhombic structure as a result of distortion and tilts.*

The octahedral rotation angles θ along [110] and ϕ along [001] can be calculated as follows [144],

$$\phi = \cos^{-1}\left(\sqrt{2}a/c\right), \quad \theta = \cos^{-1}(a/b), \tag{3.1}$$

here, a, b and c are the lattice constants of the orthorhombic unit cell. Further, it is also known that distortion in perovskite can be described only by the three-fold axes (111), of regular octahedra [150]. This angle may be calculated from unit cell dimensions as follows

$$\Phi = \cos^{-1}\left(\sqrt{2}a^2/bc\right), \tag{3.2}$$

Figure 3.4(a) shows the variation of tilt angles derived from the orthorhombic crystal structure by using the above formalism. A systematic decrease in the octahedral tilts (θ and ϕ), with the increasing R-site ionic radius of $RFeO_3$ has been observed.

Here, it is important to note that the tilts calculated using lattice constants may have large errors [144]. In order to get more accurate values of distortion angles, Oxygen Wyckoff positions have been used (as discussed below). To calculate the tilt angles θ and Φ in terms of atomic displacements, following formalisms [145] were used

$$\theta = \tan^{-1}\left[\frac{4\sqrt{u_{O(1)}^2 + v_{O(1)}^2}}{c}\right] = \frac{2\sqrt{2}w_{O(2)}}{\sqrt{a^2+b^2}} \ ;$$

$$\phi = \tan^{-1}\left[\frac{\sqrt{u_{O(2)}^2+v_{O(2)}^2}}{\sqrt{a^2+b^2}}\right], \tag{3.3}$$

Here $u_{O(1)}$, $v_{O(1)}$, $u_{O(2)}$, $v_{O(2)}$ and $w_{O(2)}$ are the absolute displacements in the Wyckoff positions of oxygen atoms. u, v, and w represent the displacement in the direction of x, y, and z respectively and subscript O(1) and O(2) represents the first and second oxygen in the Wyckoff position as given in Table 3.1(a). An example of the Wyckoff position for an orthorhombic system ($PrFeO_3$) is given in Table 3.1(b).

The displacement coordinates can easily be found by comparing both tables.

Table 3.1: *(a) Schematic of determining the atomic displacements for the orthorhombic systems, (b) Wyckoff position of an orthorhombic system ($PrFeO_3$).*

(a)	**x**	**y**	**z**
R	**$1-u_{R(1)}$**	**$V_{R(1)}$**	**0.2500**
Fe	**0.0000**	**0.5000**	**0.0000**
O1	**$u_{O(1)}$**	**$0.5-v_{O(1)}$**	**0.2500**
O2	**$0.75-u_{O(2)}$**	**$0.25+v_{O(2)}$**	**$w_{O(2)}$**

(b)	**x**	**y**	**z**
Pr	**0.9913**	**0.0442**	**0.2500**
Fe	**0.0000**	**0.5000**	**0.0000**
O1	**0.0890**	**0.4850**	**0.2500**
O2	**0.7120**	**0.2950**	**0.0501**

To estimate the various tilt angles using oxygen Wyckoff positions one need to perform necessary transformations to get an absolute value of atomic displacements of Oxygen atoms. The displacement co-ordinate of oxygen atoms $u_{O(1)}$, $u_{O(2)}$, $v_{O(1)}$, $v_{O(2)}$, and $w_{O(2)}$ were transformed into absolute displacements by using the equation

$$d = \left[(x \quad y \quad z) \mathbf{G} \begin{pmatrix} x \\ y \\ z \end{pmatrix} \right]^{1/2}, \tag{3.4}$$

where; d is the absolute displacement of oxygen atoms ($u_{O(1)}$, $u_{O(2)}$, $v_{O(1)}$, $v_{O(2)}$, and $w_{O(2)}$) and will acquire the unit of lattice constant, (x, y, z) is an arbitrary Oxygen atom displacement and G is the metric tensor and is defined as

$$G = \begin{pmatrix} \mathbf{a.a} & \mathbf{a.b} & \mathbf{a.c} \\ \mathbf{b.a} & \mathbf{b.b} & \mathbf{b.c} \\ \mathbf{c.a} & \mathbf{c.b} & \mathbf{c.c} \end{pmatrix}$$

$$= \begin{pmatrix} a^2 & abCos\gamma & acCos\beta \\ abCos\gamma & b^2 & bcCos\alpha \\ acCos\beta & bcCos\alpha & c^2 \end{pmatrix}, \tag{3.5}$$

here a, b, c, α, β, and γ are the lattice constants of the system. For orthorhombic system, a ≠ b ≠ c and $\alpha = \beta = \gamma = 90^o$. Therefore, equation (5) becomes

$$\mathrm{G} = \begin{pmatrix} \mathrm{a}^2 & 0 & 0 \\ 0 & \mathrm{b}^2 & 0 \\ 0 & 0 & \mathrm{c}^2 \end{pmatrix}, \tag{3.6}$$

Combining equations (3.4) and (3.6), the value of d can be written as

$$\mathrm{d} = \left[(\mathrm{x} \quad \mathrm{y} \quad \mathrm{z}) \begin{pmatrix} \mathrm{a}^2 & 0 & 0 \\ 0 & \mathrm{b}^2 & 0 \\ 0 & 0 & \mathrm{c}^2 \end{pmatrix} \begin{pmatrix} \mathrm{x} \\ \mathrm{y} \\ \mathrm{z} \end{pmatrix} \right]^{1/2}, \tag{3.7}$$

For example, $PrFeO_3$ system if considered, with lattice constants a = 5.483(4) Å, b = 5.580(2) Å, c = 7.788(4) Å, $\alpha = \beta = \gamma = 90^o$ and Wyckoff position given in table1 (b). By using above formalism, the obtained coordinates of oxygen atom displacements are as $u_{O(1)} = 0.089$, $v_{O(1)} = 0.015$, $u_{O(2)} = 0.038$, $v_{O(2)} = 0.045$, and $w_{O(2)} = 0.0501$. Now by using equation (3.7) the absolute atomic displacement of oxygen can be obtained i.e.

$$\mathrm{u}_{\mathrm{O}(1)}(\text{Å}) = \left[(\mathrm{u}_{\mathrm{O}(1)} \quad 0 \quad 0) \begin{pmatrix} 5.48340^2 & 0 & 0 \\ 0 & 5.58020^2 & 0 \\ 0 & 0 & 7.7884^2 \end{pmatrix} \begin{pmatrix} \mathrm{u}_{\mathrm{O}(1)} \\ 0 \\ 0 \end{pmatrix} \right]^{1/2}$$

$$\left[(0.089 \quad 0 \quad 0) \begin{pmatrix} 5.48340^2 & 0 & 0 \\ 0 & 5.58020^2 & 0 \\ 0 & 0 & 7.7884^2 \end{pmatrix} \begin{pmatrix} 0.089 \\ 0 \\ 0 \end{pmatrix} \right]^{1/2}$$

$$= \left[(0.089 \times 5.48340^2 \quad 0 \quad 0) \begin{pmatrix} 0.089 \\ 0 \\ 0 \end{pmatrix} \right]^{1/2}$$

$$= [(0.089 \times 5.48340^2 \times 0.089)]^{1/2}$$

$$= 0.48802$$

$$\therefore u_{O(1)} = 0.48802\text{Å}$$

Similarly, it was found that $v_{O(1)} = 0.0837$ Å, $u_{O(2)} = 0.20837$Å, $v_{O(2)} = 0.25111$Å, $w_{O(2)} = 0.3902$Å. By using these values in equation (3.3); for this case "θ = 14.26793" and "ϕ = 9.47162" have been estimated. The evolution of octahedra tilts derived from atomic positions for all $RFeO_3$ with increasing ionic radius of R-site ions have been shown in Figure 3.4(b) and the same tabulated in Table 3.2.

The octahedra tilt, using both the methods, as described by equation (3.1) which uses lattice constants and equation (3.3) primarily based on Oxygen Wyckoff positions were calculated and our results from both methods differ in trend as well as in its values from previous reports[60, 61] which may be due to different sample preparation methodology used or slightly different oxygen stoichiometry, which may need further investigations. All structural characteristics of $RFeO_3$ samples and octahedra tilts have been given in table 3.2 (a) and (b) respectively.

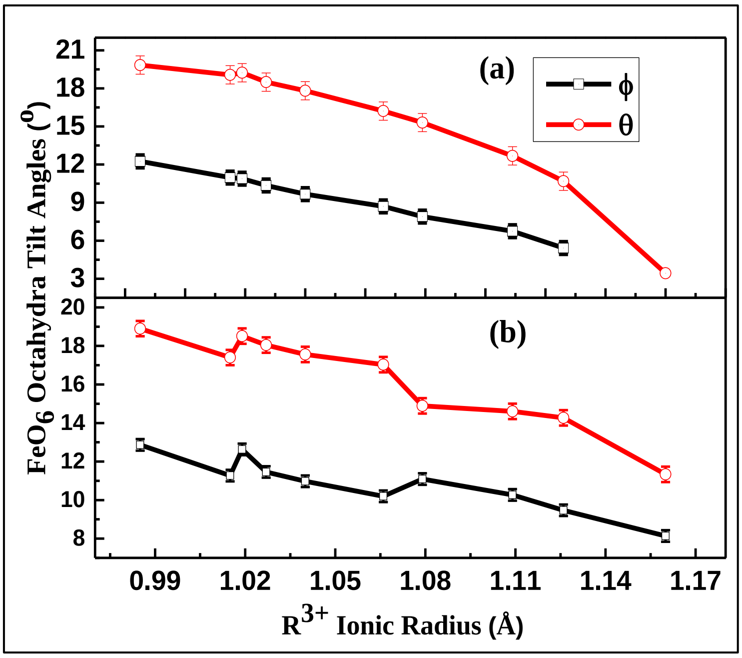

Figure 3.4: *Variation of FeO_6 octahedral tilts ϕ (100) and θ (110) with the ionic radii of rare earth cations as estimated (a) using experimental lattice constants and (b) using refined oxygen Wyckoff position of experimental SXRD data of $RFeO_3$ samples.*

Table 3.2: *Structural characteristics of RFeO3 samples: (a)R site ionic radii, lattice parameters, cell volumes, tolerance factor t calculated from the ionic radii as* $[t = (r_R + r_O)/(\sqrt{2}(r_{Fe}+ + r_O))]$ *and (b) octahedra tilt angles* $\phi(001)$, $\theta(110)$ *calculated by using lattice parameters and the atomic coordinates as well.*

(a)						
Samples		**Lattice Parameters (Pbnm Settings)**				
	r (Å)	**a (Å)**	**b (Å)**	**c (Å)**	**V ($Å^3$)**	**t**
$LaFeO_3$	**1.160**	**5.557(6)**	**5.564(1)**	**7.857(5)**	**242.816(5)**	**0.910(2)**
$PrFeO_3$	**1.126**	**5.483(4)**	**5.580(2)**	**7.788(4)**	**238.313(1)**	**0.877(6)**
$NdFeO_3$	**1.109**	**5.452(2)**	**5.588(6)**	**7.763(2)**	**236.552(6)**	**0.869(5)**
$SmFeO_3$	**1.079**	**5.400(8)**	**5.599(4)**	**7.709(9)**	**233.156(9)**	**0.864(1)**
$EuFeO_3$	**1.066**	**5.376(7)**	**5.599(5)**	**7.691(2)**	**231.557(8)**	**0.853(6)**
$TbFeO_3$	**1.040**	**5.331(6)**	**5.600(1)**	**7.647(6)**	**228.338(2)**	**0.846(5)**
$DyFeO_3$	**1.027**	**5.306(2)**	**5.595(3)**	**7.627(3)**	**226.452(9)**	**0.840(7)**
$YFeO_3$	**1.019**	**5.282(1)**	**5.594(5)**	**7.605(7)**	**224.750(8)**	**0.833(4)**
$HoFeO_3$	**1.015**	**5.283(8)**	**5.590(7)**	**7.610(3)**	**224.809(3)**	**0.845(6)**
$ErFeO_3$	**1.004**	**5.272(3)**	**5.592(3)**	**7.607(8)**	**224.2621(4)**	**0.816(5)**
$YbFeO_3$	**0.985**	**5.234(4)**	**5.564(7)**	**7.573(9)**	**220.611(5)**	**0.827(8)**

(b)	**FeO_6 Octahedra Tilt Angles (^{o})**			
Samples	**From Lattice Parameters**		**From Atomic Positions**	
	$\phi_{(001)}$	**$\theta_{(110)}$**	**$\phi_{(001)}$**	**$\theta_{(110)}$**
$LaFeO_3$	**-**	**3.438(5)**	**8.136(3)**	**11.336(3)**
$PrFeO_3$	**5.425(5)**	**10.688(5)**	**9.472(3)**	**14.267(3)**
$NdFeO_3$	**6.744(5)**	**12.682(5)**	**10.271(3)**	**14.605(3)**
$SmFeO_3$	**7.899(5)**	**15.306(5)**	**11.089(3)**	**14.892(3)**
$EuFeO_3$	**8.701(5)**	**16.217(5)**	**10.197(3)**	**17.02(3)**
$TbFeO_3$	**9.674(5)**	**17.815(5)**	**10.977(3)**	**17.558(3)**
$DyFeO_3$	**10.359(5)**	**18.498(5)**	**11.460(3)**	**18.043(3)**
$YFeO_3$	**10.887(5)**	**19.237(5)**	**12.631(3)**	**18.510(3)**
$HoFeO_3$	**10.969(5)**	**19.071(5)**	**11.269(3)**	**17.390(3)**
$ErFeO_3$	**11.445(5)**	**19.477(5)**	**12.103(3)**	**18.677(3)**
$YbFeO_3$	**12.251(5)**	**19.841(5)**	**12.269(3)**	**18.901(3)**

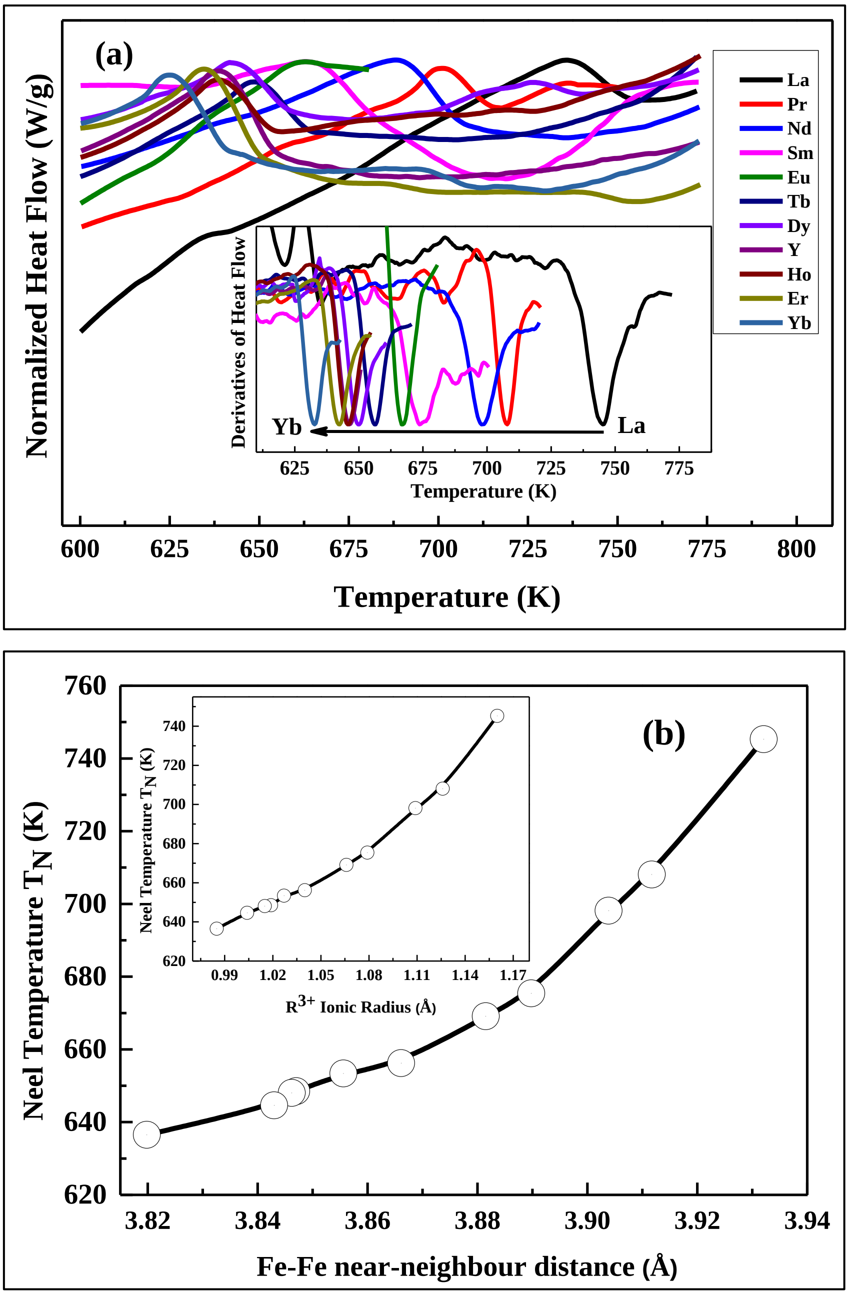

Figure 3.5: *(a) Differential scanning calorimetry (DSC) curves in the temperature range 520–775 K, in the inset the first derivative of DSC curves have been shown, and (b) Neel temperature (T_N) as a function of Average Fe-Fe NND, inset shows the variation of T_N with increasing ionic radius of R site cations of $RFeO_3$.*

3.3.2 Thermal Analysis

The DSC measurements were performed to determine the ordering temperature of $RFeO_3$ samples, because it possesses anti-ferromagnetic first order transition and is often accompanied by the amount of energy release (exothermic process)[97], as discussed in

Chapter 2, section 2.2, the anti-ferromagnetic and ferrimagnetic transitions in solid materials governs by exothermic processes and can be observed by exothermic shifts in upward direction in DSC thermograms[98].

In $RFeO_3$ samples, the magnetism originates due to the presence of Fe and R ions and their mutual interactions. The antiferromagnetic interaction between iron magnetic moments (Fe-Fe) is remarkably strong and responsible for the transition from antiferromagnetic state to a paramagnetic state characterized by the Neel temperature in the high-temperature region. Figure 3.5(a) shows the magnified section of differential scanning calorimetry (DSC) curves of $RFeO_3$ samples and in the inset of Figure 3.5(a) derivative of DSC curves have been shown. The temperature corresponding to the dip associated with each curve is recognized as Neel temperature (T_N) i.e. the transition from paramagnetic (high temperature) to antiferromagnetic (low temperature) state which is consistent with the earlier report [151, 152]. The variation of T_N with Fe-Fe near-neighbor distances of $RFeO_3$ samples have been shown in Figure 3.5(b).

A nonlinear dependency of the magnetic ordering T_N with Fe-Fe NND and with ionic radius of R-site cations was observed (as shown in the inset of Figure 3.5(b)). In $RFeO_3$ samples, each Fe ion is surrounded by six O ions in a FeO_6 octahedron and an increase in the radius of R site ions lower the octahedra tilts (Figure 3.4) which leads to the increase in Fe-O-Fe bond angles and Fe-Fe near neighbor distances. Hence an increase in Neel Temperature is observed with the increase in R-site ionic radius of $RFeO_3$ family.

3.4 Summary

In summary of this chapter, we report the pure-phase sample preparation and characterization of polycrystalline samples of $RFeO_3$ with R = La, Pr, Nd, Sm, Eu, Tb, Dy, Y, Ho, Er, and Yb by using citrate sol-gel method. The synchrotron powder X-ray diffraction (SPXRD) measurements have been carried out on all $RFeO_3$ samples to analyze the structure of the prepared samples in greater details. SPXRD results and analysis suggest that the $RFeO_3$ systems crystallize in pure orthorhombic structure with space group Pbnm. The structural characteristics i. e. lattice constants, R-O bond length and Fe-O-Fe bond angles, and FeO_6 octahedra tilts were found to vary almost linearly, while Fe-O bond length observed to be constant with increasing R-site ionic radius of $RFeO_3$ samples. Further, thermal analysis was used to explore the correlation between magnetic ordering temperature (T_N) and structural parameter (Fe-Fe NND and ionic radius of rare-earth ions).

Chapter 4

Optical and Electronic Properties of Rare-earth Orthoferrites

In recent years, optical absorption spectroscopy has been widely used to probe the electronic structure of similar ferrites and the said electronic structure is believed to be responsible for various physical properties of these materials. Thus, the present chapter is devoted to exploring the effect of R-site ionic radius on the optical and electronic properties of $RFeO_3$[2]

4.1 Introduction

In the recent years, optical absorption spectroscopy in the energy range from ~6 eV to ~0.5 eV has been widely used to probe the electronic structure of various transition metal oxides including that of rare-earth orthoferrites such as $LaFeO_3$, $PrFeO_3$, $YFeO_3$, etc.[91, 99, 153, 154]. It is well known that the electronic structure critically control various physical properties of material[155] and the electronic structure is essentially dictated by the periodic arrangement of the atoms present in the sample [156-163]. Therefore, keeping in view the advantages of optical absorption spectroscopy to probe the electronic structure, band gap etc., optical absorption spectroscopy experiments have been carried out for all the $RFeO_3$ samples and possible correlation between the structural parameters such as lattice constants, bond length, etc. on the electronic structure (bandgap) of $RFeO_3$ has been investigated. The optical absorption study on $RFeO_3$ samples suggests that the band gap 'E_g' of the prepared samples do not have a significant effect with a

---

[2] ***M. Kamal Warshi et al. Ceramic International, 44 (2018), 8344-8347.***

change in the R site ionic radius of $RFeO_3$ samples i.e. the E_g of the prepared samples almost remain constant and observed to lie between 1.94 eV to 1.97 eV.

From chapter 3, it can be observed that with the increase in the radius of R site cations, the lattice constants (a, b, c), Fe-O-Fe bond angles, and R-O bond lengths vary systematically, whereas; Fe-O bond lengths associated with FeO_6 octahedra almost remain constant with replacement of R-site ions throughout the series.

4.2 Experimental Details

Optical Characterizations

Defused Reflectance Spectra (DRS) of $RFeO_3$ samples were collected in the spectroscopic range of 1000-200 nm using a high precision Carry 60 UV-Vis-Agilent spectrophotometer. A Harrick Video-Barrelino diffuse reflectance probe has been used to acquire the data [154, 164-166]. The detail of DRS was discussed in detail in chapter 2.

4.3 Results and Discussions

In Figure 4.1, diffuse reflectance spectra of all $RaFeO_3$ samples have been shown as a function of wavelength. Strong absorptions have been observed around 500-600 nm in all $RFeO_3$ samples, generally, it is called p-d transition, and this is recognized as the main absorption peak which decides the bandgap of these materials. Another important feature of these spectra appeared around 600-700 nm, this is manifested as a well-known d-d transition in these samples. This transition will be discussed in detail in chapter 6.

The obtained spectra were converted into absorption spectra using Kubelka-Munk equation [107, 108] given by

$$F(R) = \frac{(1-R_\infty)^2}{2R_\infty}, \tag{4.1}$$

where $F(R_\infty)$ is Kubelka-Munk function and $R_\infty = R_{sample}/R_{standerd.}$ Here, R_{sample} is the diffuse reflectance of the sample and $R_{standard}$ is diffuse reflectance spectra of a non-absorbing standard sample ($BaSO_4$ in the present case). The Kubelka-Munk function represented in equation (4.1), can be written in terms of absorption coefficient as follows;

$$F(R_\infty) \propto \alpha \propto \frac{\left(h\nu - E_g\right)^{1/n}}{h\nu}, \tag{4.2}$$

$$[F(R_\infty) * h\nu]^n = A\left(h\nu - E_g\right), \tag{4.3}$$

here, n = 2 for the direct bandgap materials and for indirect bandgap materials n = 1/2. For $RFeO_3$ n = 1/2 is used as it is known to be indirect bandgap materials [167, 168].

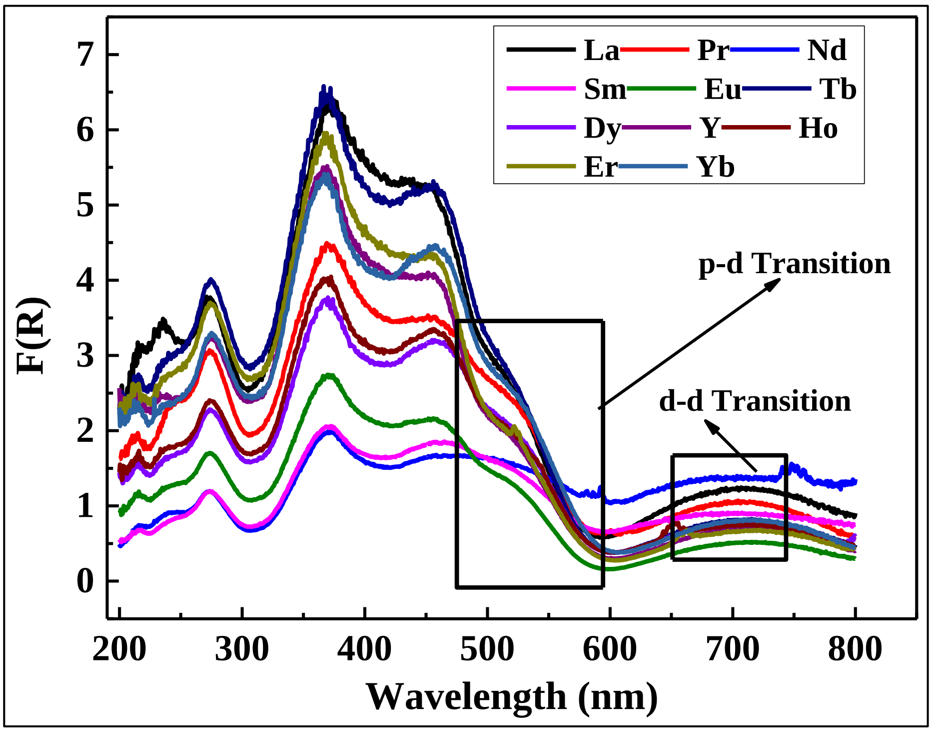

Figure 4.1: *Diffused reflectance spectra of $RFeO_3$ samples.*

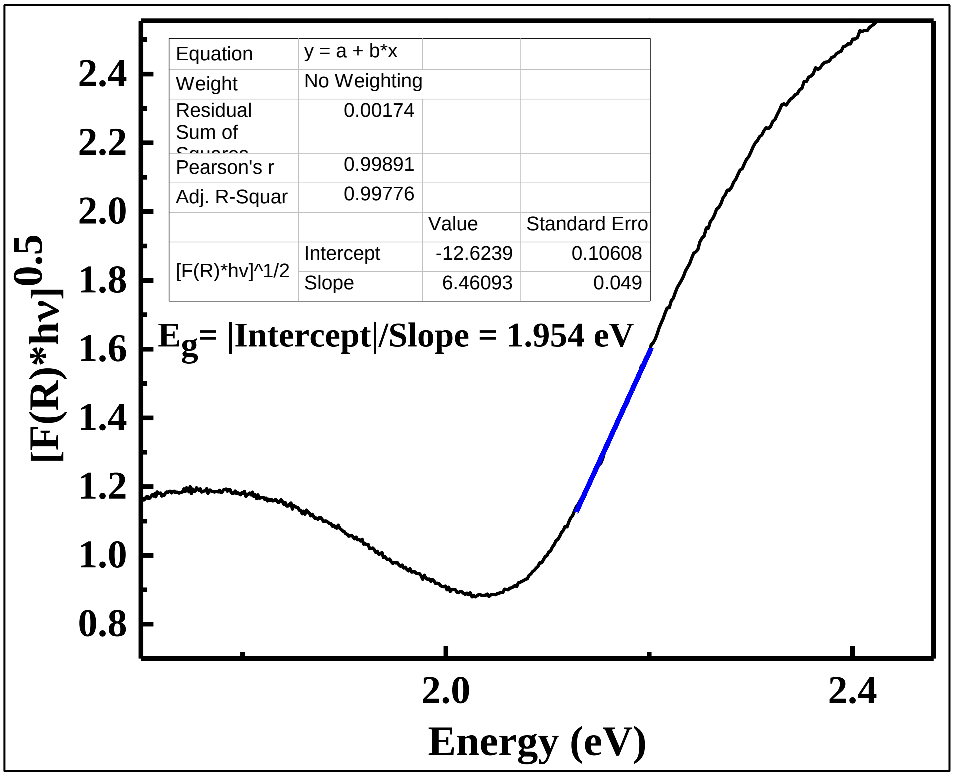

Figure 4.2: *Zoomed section of absorption spectra derived from DRS spectra by using the Kubelka-Munk equation, the inset shows the parameters of linear fitting and the way of calculation of bandgap*

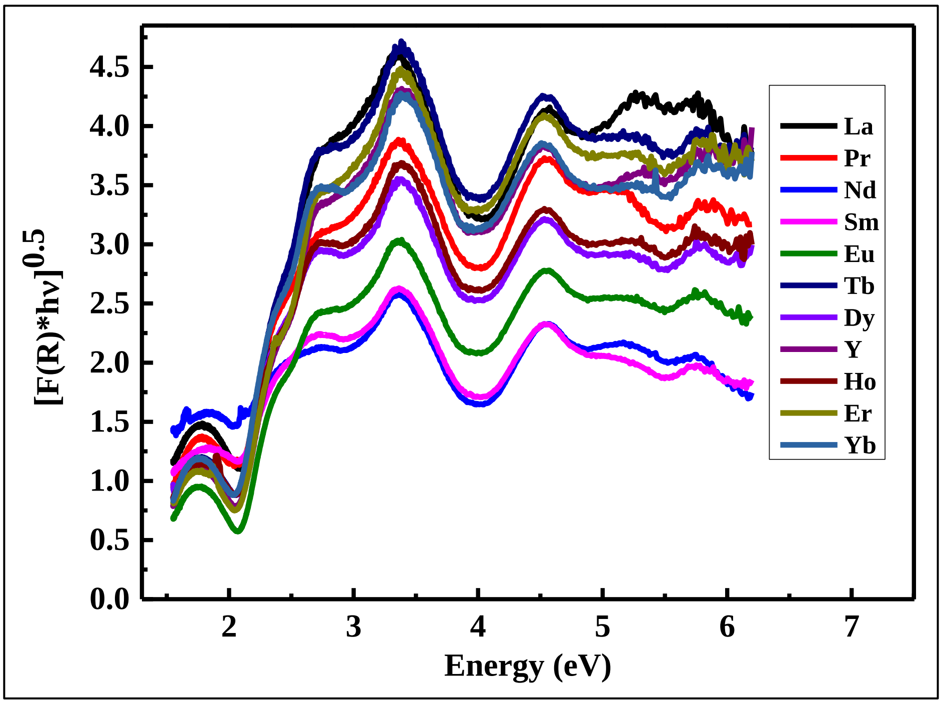

Figure 4.3: *Absorption spectra as a function of energy derived from diffuse reflectance spectra by using the Kubelka-Munk equation of all* $RFeO_3$ *samples.*

Figure 4.2 shows the zoomed section of *$[F(R_\infty)*hv]^{0.5}$* versus photon energy (*E)* plot of $YbFeO_3$ sample. A line has been fitted in the linear region of optical absorption spectra. The point where the straight line cuts the energy axis is taken as the bandgap E_g of the studied sample. In the inset of Figure 4.2, some parameters of linear fitting and the way of calculating bandgap have demonstrated. Accordingly, the absorption spectra of each $RFeO_3$ samples have been shown in Figure 4.3, the band gap of all samples has been estimated and plotted as a function of the ionic radius of R-site cations, shown in Figure 4.4. It is clear from this figure that E_g of all samples is found to be around 1.94eV to 1.97 eV (±0.02eV), i. e. these appear to be almost constant, keeping in view the statistical error of the measurements (To determine the statistical error, the experiment was repeated for 10 times on the same sample. Each time the bandgap of that sample has been estimated using the scheme discussed above and an error of about ±0.02 eV has been found in the estimation of bandgap).

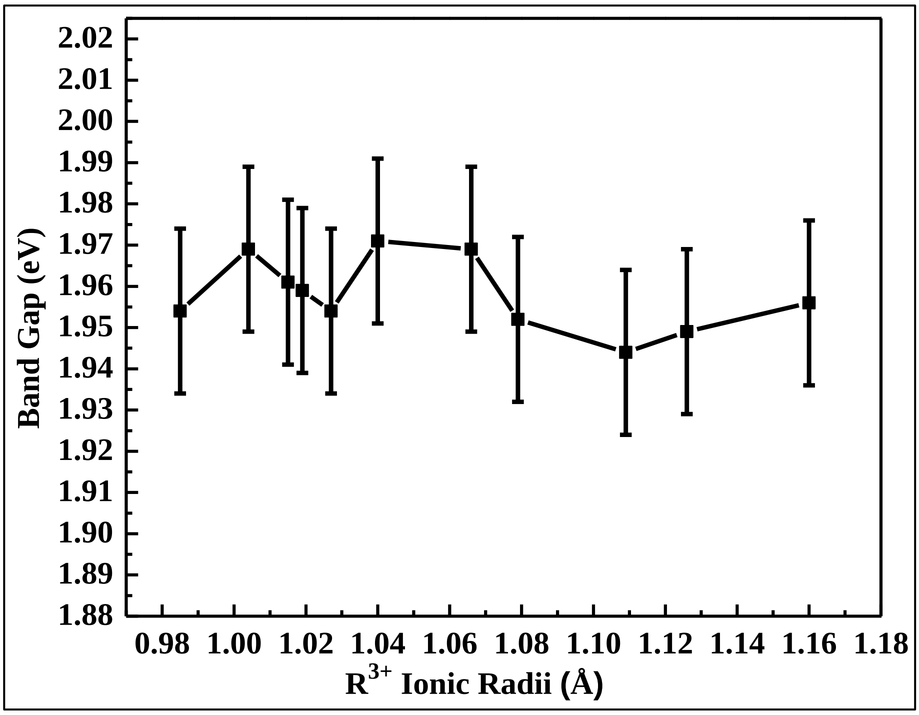

Figure 4.4: *The bandgap of $RFeO_3$ samples as a function of the ionic radius of R site cations.*

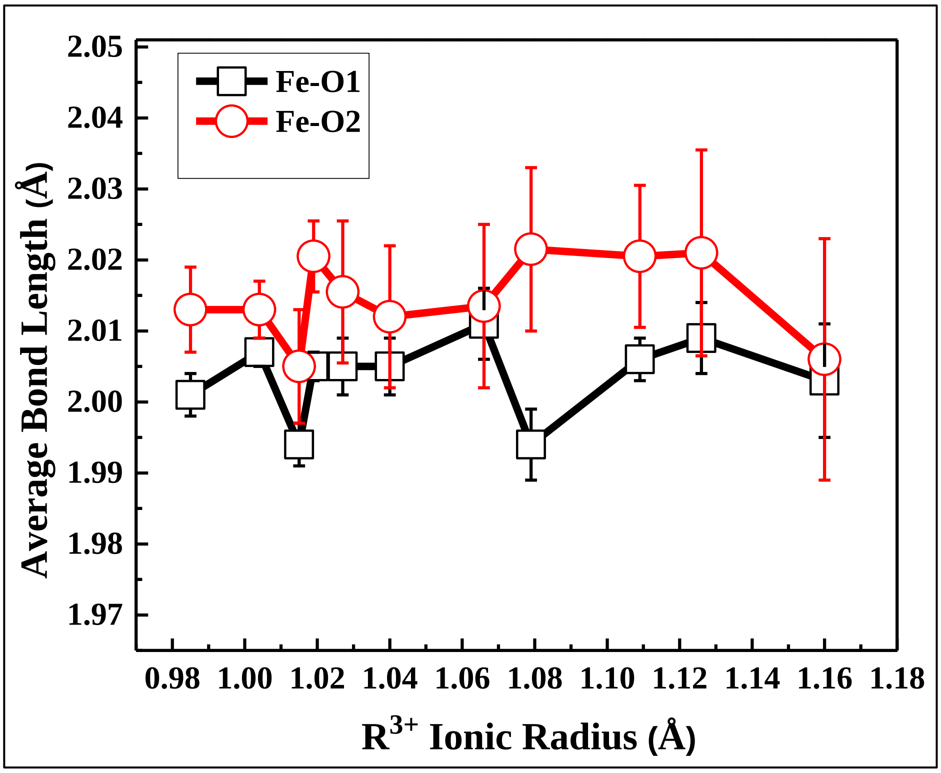

Figure 4.5: *Fe-O bond lengths as a function of the increasing radius of R site cations of* $RFeO_3$ *samples.*

Now, if we recall the structural analysis of $RFeO_3$ samples done in chapter 3, it can be observed that the structural parameters such as lattice constants (a, b, c), cell volume, R-O bond length, and octahedra tilts vary systematically, whereas Fe-O bond length (i.e. Fe-O orbital overlap almost remains constant with increasing ionic radius of R site cations, as shown in Figure 4.5. In $RFeO_3$ systems, it is known that near Fermi level i.e. states near conduction band minimum (CBM) and valence band maximum (VBM) is dominated by Fe-3d and O-2p orbitals[165, 169]. That is the band gap is essentially controlled by the extent of overlap between the Fe-3d and O-2p orbitals and corresponding hybridization. Thus, it appears that the constant value of Fe-O bond length (e.g. the constant value of overlap or hybridization between O-2p and Fe-3d orbitals) may be responsible for the constant value of the optical bandgap in $RFeO_3$ samples[28, 32, 40, 61, 170]. This indicates that the value of bond length or the extent of Fe-3d and O-2p overlap may change the bandgap. This means the Fe-O bond lengths may critically dictate bandgaps in these materials. This is found to be consistent with earlier reports which suggest that band gap changes with the modification in the bond lengths [161, 171-173]. Further, A first-principles study needed to explore the claim in depth.

4.4 Summary

We have studied the effect of R-site ionic radius on the optical properties of pure-phase polycrystalline $RFeO_3$ (R = La, Pr, Nd, Sm, Eu, Tb, Dy, Y, Ho, Er, and Yb) perovskite oxides, synthesized using citrate sol-gel method. Our study suggests that the optical bandgap in $RFeO_3$ samples appears to be independent of structural parameters such as lattice constants and R-O bond length, etc. whereas, it appears that the bandgap is essentially controlled by Fe-O bond length i.e. the overlap between Fe-3d and O-2p orbitals in $RFeO_3$ samples. Thus, the tuning of Fe-O bond lengths may be used to control the band gap in $RFeO_3$ samples. Further, A first-principles study strongly needed to establish the claim.

Chapter 5

Theoretical Investigations of Structural, Electronic, and Magnetic Properties of Rare-earth Orthoferrites

In this chapter, the details of structural, electronic and magnetic properties of $RFeO_3$ samples using theoretical approaches have been provided. The structural parameters (such as lattice constants, Fe-O/R-O bond lengths, octahedra tilts) of $RFeO_3$ samples shown (experimentally determined) in chapter 3, have been validated using and Bond Valence Sum (BVS) and Density Functional Theory (DFT). Further, the optical properties such as bandgap of $RFeO_3$ samples as discussed in chapter 4, have been examined in detail using DFT. Furthermore, a detailed study of defect-induced ferromagnetism of $RFeO_3$ samples has been provided using DFT[3].

5.1 Introduction

In chapter 2, we have discussed the evolutions of density functional theory (DFT) as an alternative quantum mechanical many-body approach to study the ground state properties of materials. Hohenberg-Kohn-Sham density functional theory[116-118] has emerged as one of the most successful theories for predicting the ground state electronic structure of crystalline systems and consequently other physical properties of systems.

---

[3] ***M. Kamal Warshi et al. Ceramic International, 44 (2018), 8344-8349.***
M. Kamal Warshi et al. Ceramic International, 44 (2018), 13507-13512.

In chapter 3, using synchrotron powder x-ray diffraction data, we have determined the structural parameters of $RFeO_3$ samples experimentally. It was observed that with increasing radius of R site cations the structural parameters such as lattice constants (a, b, c), Fe-O-Fe bond angles and R-O bond lengths change systematically, whereas; Fe-O bond lengths associated with FeO_6 octahedra almost remain constant throughout the series. In order to explain the mechanism behind the observed experimental results, DFT has been carried out using the WIEN2k package. In order to simulate the values of lattice parameters etc. two approaches have been adopted (i) Bond Valence Sum [135] implemented in SPuDS [134] and (ii) density functional theory as implemented in WIEN2k package [122].

In chapter 4, the optical absorption study on $RFeO_3$ samples suggests that the band gap 'E_g' of the prepared samples do not show any significant effect due to change in the R-site ionic radius i.e. the E_g of the prepared samples almost remain constant and observed to lie between 1.94 eV to 1.97 eV. In order to comprehend the obtained experimental results with greater details, again DFT was carried out using the full-potential linearized augmented plane wave (FP-LAPW) method within the density-functional theory implemented in WIEN2k package.

Moreover, $RFeO_3$ system is well-known antiferromagnetic (AFM) ground state materials [60, 174] and the antiferromagnetic ordering of the Fe^{3+} ions known to occur at Neel temperature (T_N) ~640K-750K [60, 174], but, simultaneously, the coexistence of electric and magnetic ordering (multiferroicity) in $RFeO_3$ samples have been reported [29, 32, 80, 81]. Also, there exist literature on the weak ferromagnetism in these compounds due to the canting of spins [82, 83] which is also considered to be responsible for the observed ferroelectricity in $RFeO_3$ [12, 56]. Thus, there exist large discrepancies regarding the experimentally observed high values of magnetic moments [84-86] and behavior of MH loop for $RFeO_3$ compounds as shown in Figure 5.1. Some experimental reports also suggest the occurrence of double hysteresis loop [84, 85] possibly due to two types of magnetic interactions [85, 175-177] present in the samples.

On the other hand from the viewpoint of synthesis of these materials, available literature suggests that the formation energy of $RFeO_3$ is larger as compared to its garnet counterpart $R_3Fe_5O_{12}$ [87-89]. This reveals that it is difficult to synthesize $RFeO_3$ with a proper stoichiometry especially through solid state reaction route, which may result in defect or self-doping in $RFeO_3$ samples and thus, self-doping is very common in the samples prepared *via* solid state reaction route and sol-gel methods [178, 179]. Also, ferromagnetism in antiferromagnetic systems like $LaMnO_3$ reported [11, 180, 181] due to self-doping.

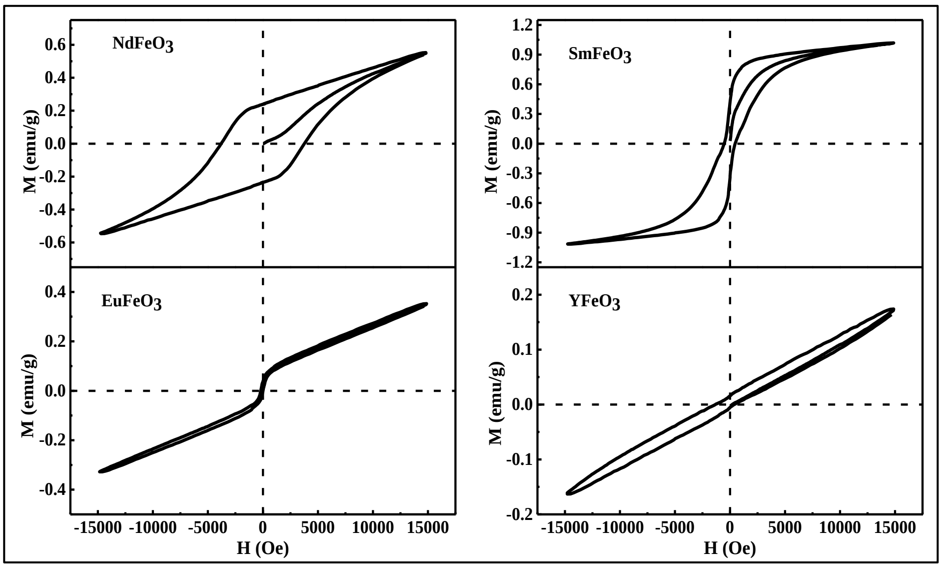

Figure 5.1: *Room temperature M-H curves of prepared* $RFeO_3$ *samples.*

Hence, it will be advantageous to investigate the possible effect of self-doping on the magnetic ground state of orthoferrites in order to explore the origin of ferromagnetism in $RFeO_3$ systems. Hence in the present chapter, a detail investigation of the effect of self-doping on the magnetic properties of $RFeO_3$ have been provided. In order to explore the effect of self-doping on the magnetic ground state of $RFeO_3$, the first principle calculations considering spin-polarization into account have been carried out on one of the rare-earth orthoferrites $YFeO_3$. The Bader charge analysis [131] has also been done in order to understand the calculation results in terms of the mixed-valence state of Fe (i. e. Fe^{3+}/Fe^{4+}) which may result in ferromagnetism.

5.2 Theoretical Details

The theoretical approach used in calculation had given in chapter 2, section 2.3 and 2.4 in detail.

5.3 Results and Discussions

5.3.1 Structural Properties

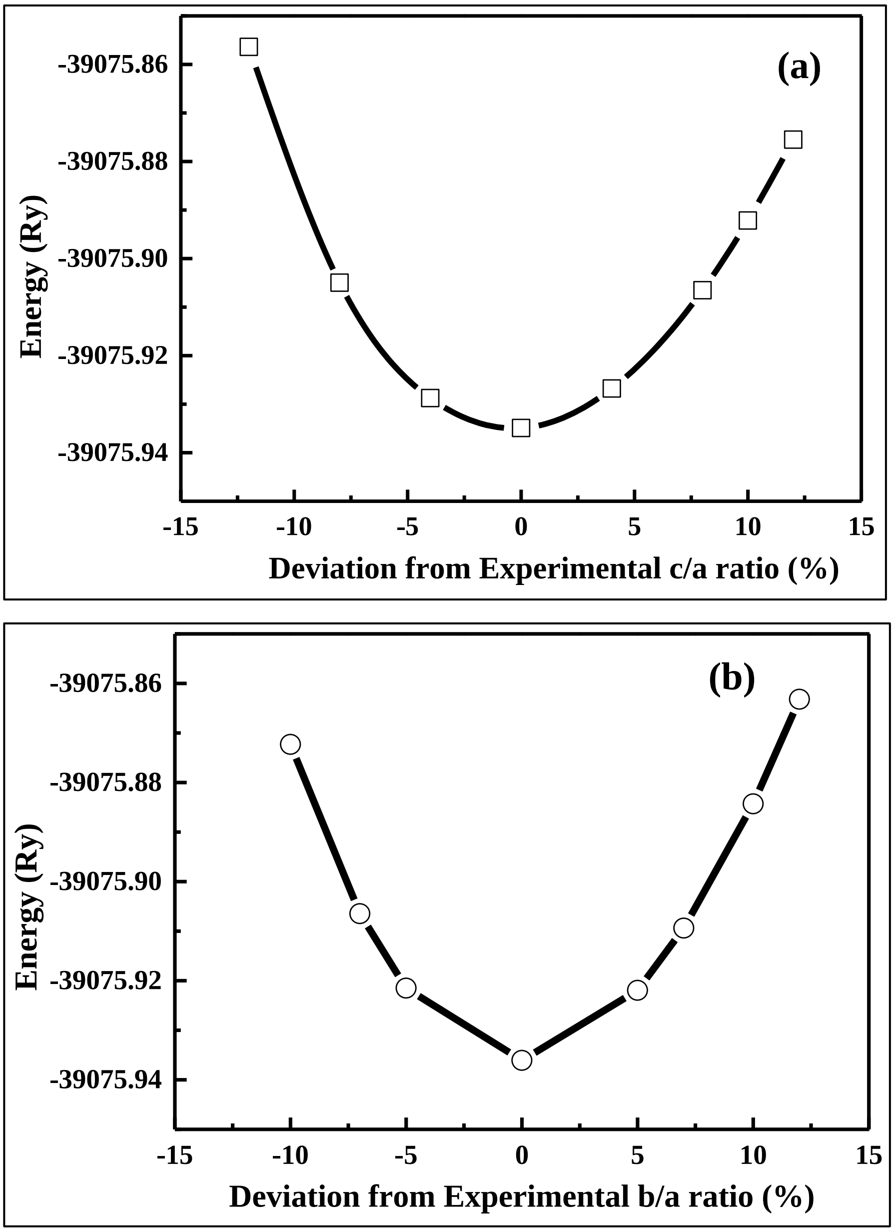

Figure 5.2: *The ground state energy verses (a) percentage change in c/a, (b) percentage change in b/a ratio.*

The optimized lattice parameters were obtained for $RFeO_3$ systems by calculating ground state energies of conventional unit cells for different c/a and b/a percentages with constant volumes, we observed that our system is stable around 0 percent change in c/a (b/a) as shown in Figure 5.2. Then the optimized c/s ratios were obtained by fitting energy as a function of c/a (b/a) ratio with higher order polynomial to get the minima of the curve which corresponds to the optimized lattice parameters. In both optimizations (c/a and b/a) we got the same values of lattice parameter for minimal energy $RFeO_3$ systems.

Figure 5.3 (a) and (b) shows the comparative graphs of lattice constants and octahedra tilt angles respectively, obtained experimentally and theoretically. From the Figure 5.3 (a) and (b), it appears that the value of lattice constants and various tilts obtained experimentally using synchrotron-based powder x-ray diffraction experiments and estimated using theoretical calculations (DFT and BVS), matches well.

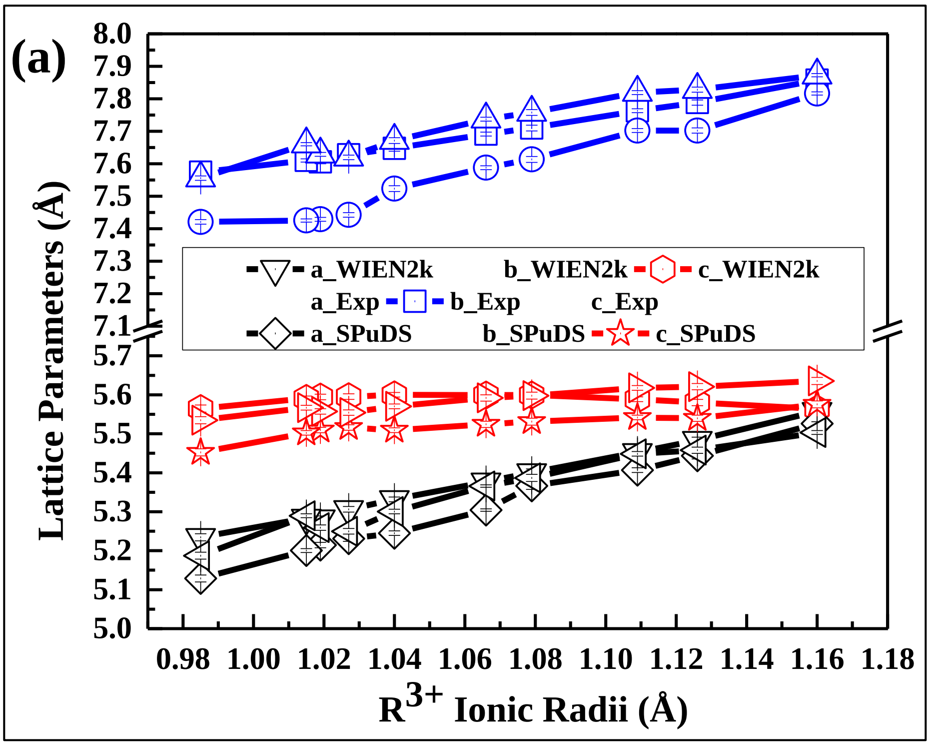

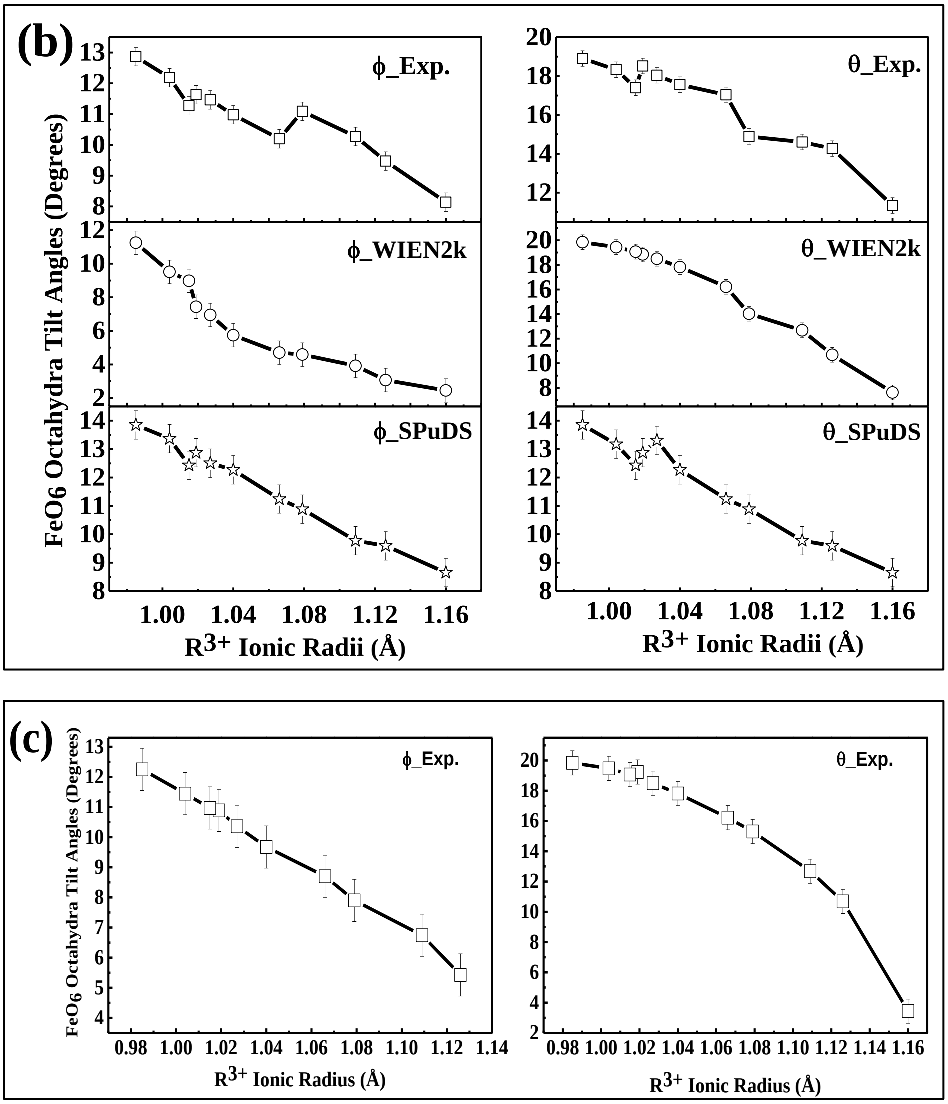

Figure 5.3: *Comparison of experimental and theoretical (a) lattice constants, (b) octahedra tilts obtained from O Wyckoff positions, (c) Octahedra tilts obtained from lattice constants.*

The octahedra tilt angles predicated by BVS (SPuDS), DFT (WIEN2k) and estimated experimentally using oxygen Wyckoff positions shows almost linear dependence (See figure 5.3(b)), whereas the tilt angle estimated experimentally using lattice constants shows the nonlinear behavior with R-site ionic radius for $RFeO_3$ system (see figure 5.3(c)). This suggests that the behavior tilt angles estimated using Wyckoff positions may be more accurate as compared to that of lattice constants. A high-resolution neutron diffraction studies may be further useful in this regard.

5.3.2 Electronic and Optical Properties

In order to understand the experimentally observed constant value of E_g with the increasing ionic radii of R-site cations, first principle calculations have been carried out employing DFT in WIEN2k package as discussed above. Calculations have been performed to investigate the contributions of various atomic orbitals of $RFeO_3$ to the valence and conduction bands near Fermi level (E_F). Figure 5.4 (a)-(d) shows the calculated DOS of $RFeO_3$ samples. It is important to note here that the detailed analysis of DOS suggests that the states near E_F are dominated by the O-2p and Fe-3d orbitals.

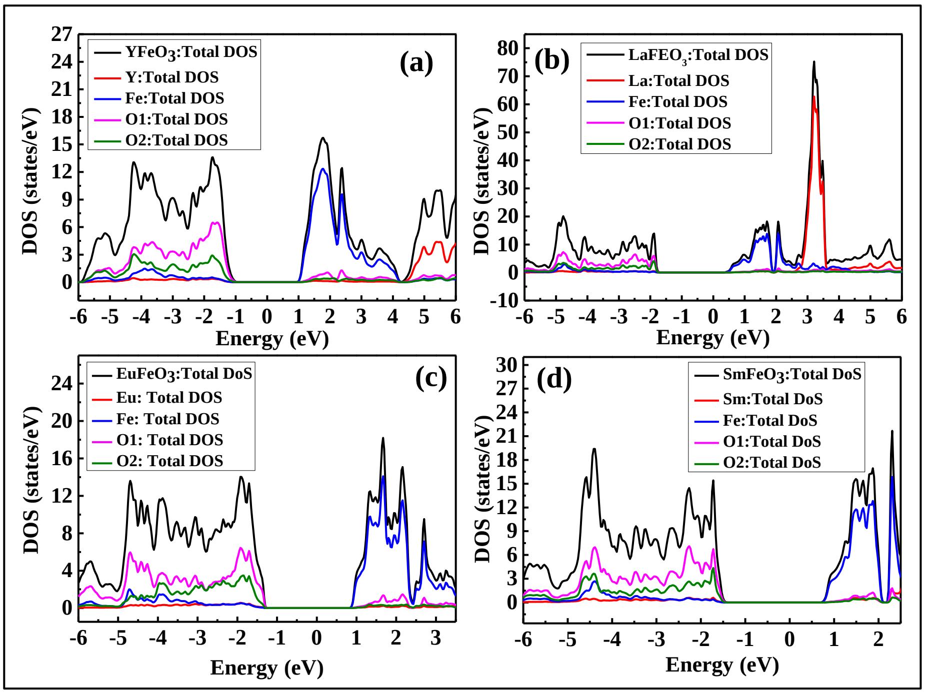

Figure 5.4: *(a) - (d) total and partial density of states for* $RFeO_3$ *samples.*

At this juncture, it is important to note that in the case of $RFeO_3$ the structural parameters such as lattice constants, R-O bond lengths etc. changes systematically with the radius of R site cation, whereas the Fe-O bond length i.e. Fe-O orbital overlap almost remains constant. Further, experimental optical absorption spectroscopy and first principle calculations suggest that the optical band gap of these samples almost remains constant. The detailed analysis of the first principle studies (Figure 5.4(a)-(d)) suggest that the states near Fermi level i.e. valence band maximum and conduction band minimum are dominated by Fe-3d and O-2p orbitals, hence it appears that the constant value of Fe-O bond length (orbital overlap and hence hybridization) may be responsible for the constant value of the band gap. This indicates that the value of bond length or the extent of Fe-3d and O-2p overlap changes the band gap. This means, if the bond length is changed, the bandgap will also change. It is important here to note that the position of the Fermi level is close to unoccupied states i.e. shifted towards conduction band this suggests the different value of electron and hole effective masses in these samples[182].

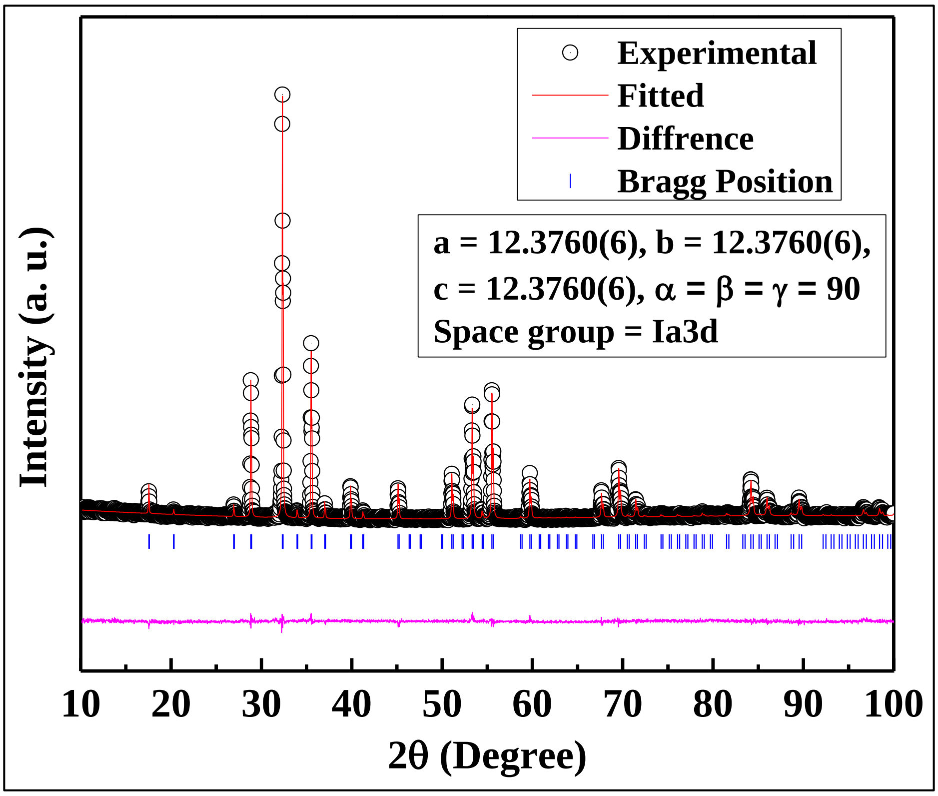

Figure 5.5: *Rietveld refinements of $Y_3Fe_5O_{12}$.*

In order to confirm the role of Fe-O bond length on the optical bandgap, the $Y_3Fe_5O_{12}$ sample has been prepared and its optical and first principle electronic properties have been studied. $Y_3Fe_5O_{12}$ is different from $RFeO_3$ type perovskite, however, it is also a rare-earth based ferric oxide system, where the value of Fe-O bond length is ~1.824(6)Å which is different from that in $RFeO_3$ samples as calculated from refinements of XRD data. The experimental and fitted curve has been shown in Figure 5.5 and in the inset structural information of the sample has been provided.

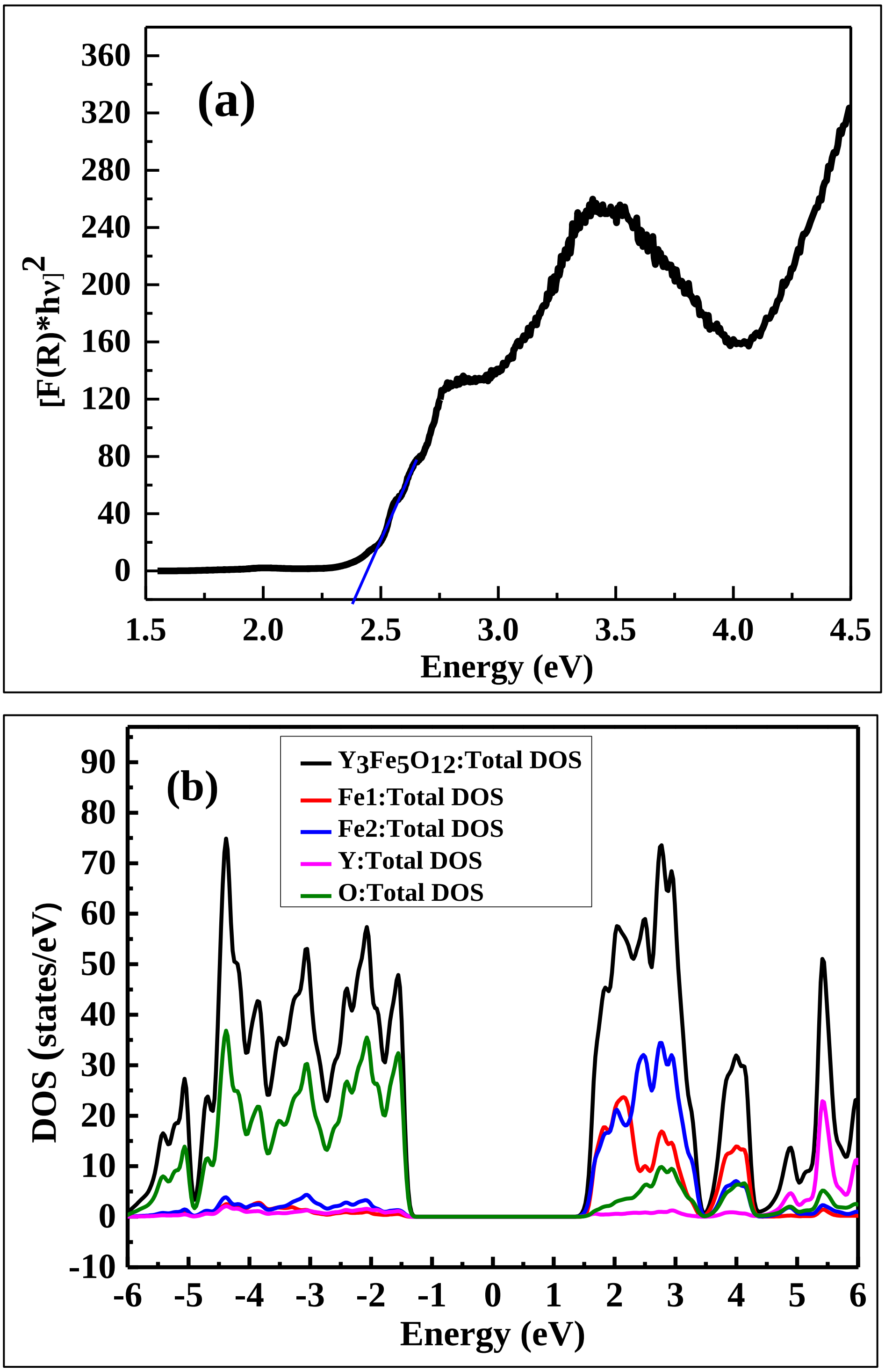

Figure 5.6: *(a) Diffused reflectance spectra as a function of energy derived by using Kubelka-Munk equation., (b)Represents the total and partial density of states for* $Y_3Fe_5O_{12}$ *samples.*

The band gap of $Y_3Fe_5O_{12}$ obtained from its experimental absorption spectra, shown in Figure 5.6 (a) is found to be 2.42 eV, which matches well with the earlier report [183]. Importantly, the density of states near the Fermi level in $Y_3Fe_5O_{12}$ is also found to be dominated by Fe-3d and O-2p orbitals as shown in Figure 5.6 (b).

This suggests that the value of the band gap in $Y_3Fe_5O_{12}$ is essentially detected by the orbital overlap or Fe-O bond length. Hence it may be interpreted that different value of Fe-O bond length in $Y_3Fe_5O_{12}$ may be responsible for the different value of band gap (when compared to that of $RFeO_3$). This is found to be consistent with earlier reports which suggest that band gap changes with modification in the bond length [161, 171-173].

The first principle studies suggest that the states near Fermi level i.e. states near valence band maximum (VBM) and conduction band minimum (CBM) are dominated by Fe-3d and O-2p orbitals and the band gap is essentially controlled by the extent of overlap between the Fe-3d and O-2p orbitals and corresponding hybridization. Thus; it appears that the almost constant value of Fe-O bond lengths (e.g. the constant value of overlap between O-2p and Fe-3d orbitals) associated with FeO_6 octahedra may be responsible for almost the constant value of E_g in the samples explored in the present study.

5.3.3 Electronic and Magnetic Properties

As discussed above in the introduction of this chapter, $RFeO_3$ samples have well-known antiferromagnetic ground states, but the results of M~H measurements shown in Figure 5.1 suggests these samples be ferromagnetic at room temperature. First principle calculations using spin-polarized DFT have been done on pure and self-doped $YFeO_3$ sample in order to understand the ground state magnetic properties of $RFeO_3$.

To investigate the effect of self-doping on magnetic properties of $RFeO_3$, we have calculated and compared the total energy of $YFeO_3$ compound considering both FM and AFM phases[174] and found FM phases of $YFeO_3$ have higher total energies than the AFM phases by 0.343 eV (i.e., $\Delta E_{FM\text{-}AFM}$ = 0.343 eV) per formula unit. Thus, our calculations suggest that the AFM phase of $YFeO_3$ is energetically more favorable than the FM phase. These results are consistent with those reported earlier [83, 174, 184]. Here it is crucial to note that some experimental reports confirm the net magnetic moment for $YFeO_3$ [42, 86, 177, 185, 186] possibly due to canting of spins[176, 177, 187].

As discussed in the introduction of this chapter, the samples prepared by solid-state reaction route and sol-gel methods may give rise to point defects (self-doping) at Y, Fe and O sites, in $YFeO_3$. Hence, in order to explore the possible effect of above mention point defects on the magnetic ground state of $YFeO_3$ first principle calculations were carried out. For this purpose, we have first calculated the Y, Fe and O defect formation energy using equation (5.6). To calculate the formation energies of these defects, the chemical potential energy of Yttrium (μ_Y), Iron (μ_{Fe}) and O (μ_O) were calculated from their most stable crystal structure, such as Y in hexagonal closed packed (hcp) structure with space group $P6_3/mmc$, Fe in body-centered cubic (bcc) with space group Im-3m and an FCC unit cell for O_2. The similar approach has been used earlier by various research groups [188, 189].

Table 5.1 represents the total energy for pure and self-doped $YFeO_3$ system, suggesting that the oxygen defect is most stable amongst all defects studied. These results are found to be consistent with earlier reports [190, 191].

Table 5.1: *Defect models and corresponding total energy.*

Sample	**$YFeO_3$**	**Y-defect $YFeO_3$**	**Fe-defect $YFeO_3$**	**O-defect $YFeO_3$**
Total Energy/Unit Cell (Ry)	**-39075.4177**	**-36818.0023**	**-38226.8284**	**-39025.1697**

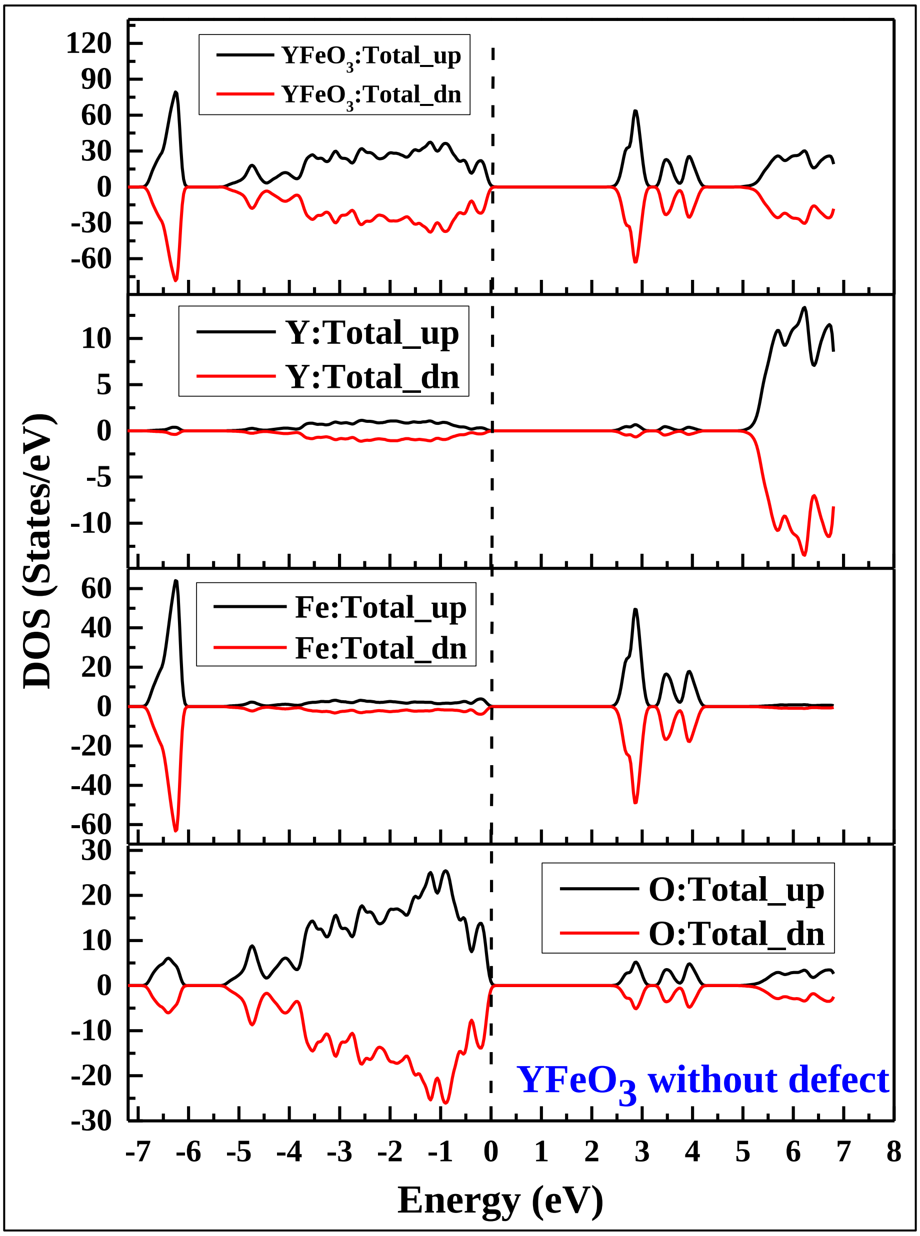

Figure 5.7: *Partial and total density of States of pure or stoichiometric $YFeO_3$ samples.*

Figure 5.7 shows the total and partial DOS for pure $YFeO_3$. From Figure 5.7 it is clear that for defect-free $YFeO_3$ spin up and down bands are exactly symmetrical thus canceling each other to give rise to a net zero magnetic moment. This is consistent with earlier reports[192]. Thus, pure $YFeO_3$ favors AFM ground state which is consistent with the total energy argument as discussed above.

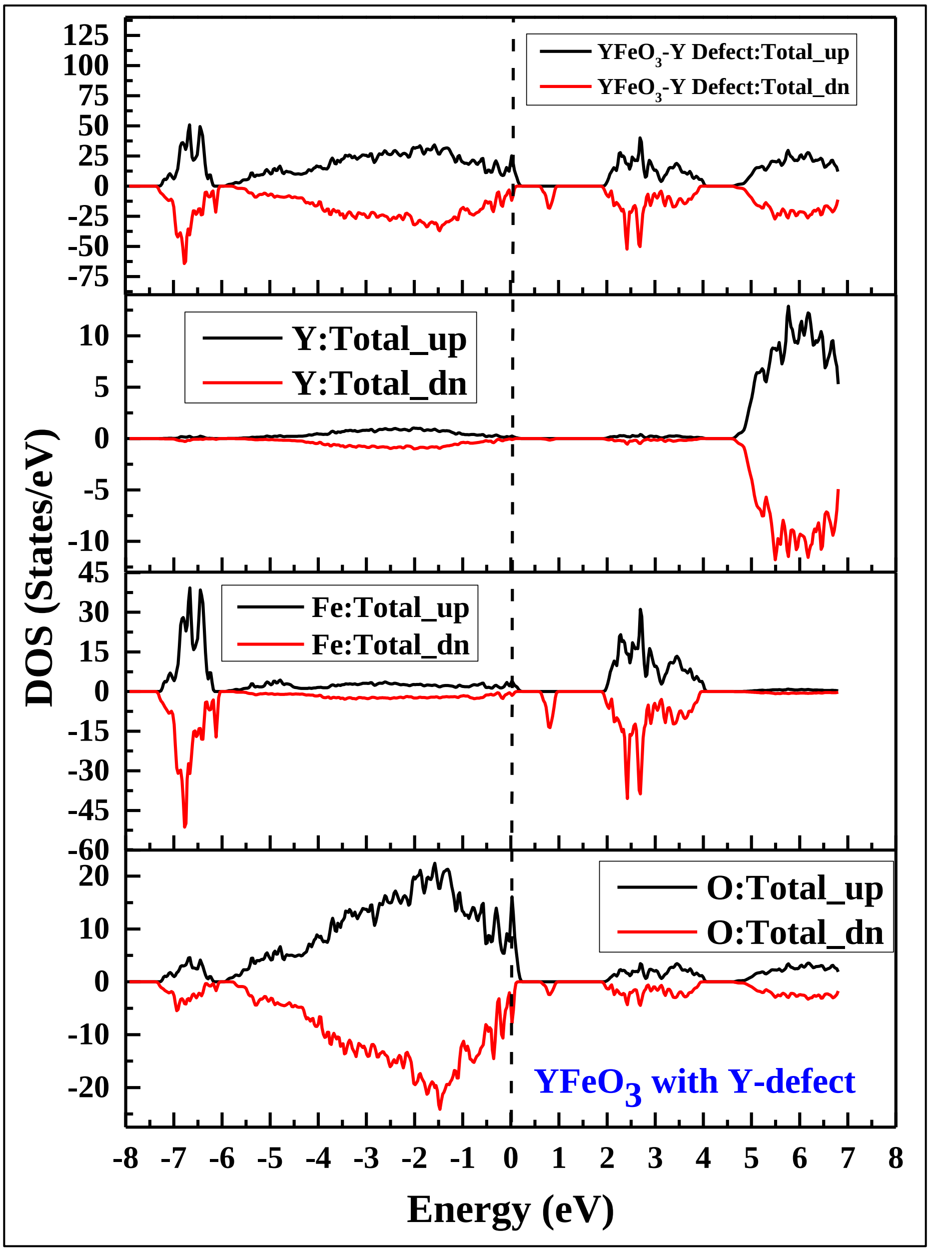

Figure 5.8: *Partial and total density of States of Y-defect YFeO$_3$ sample.*

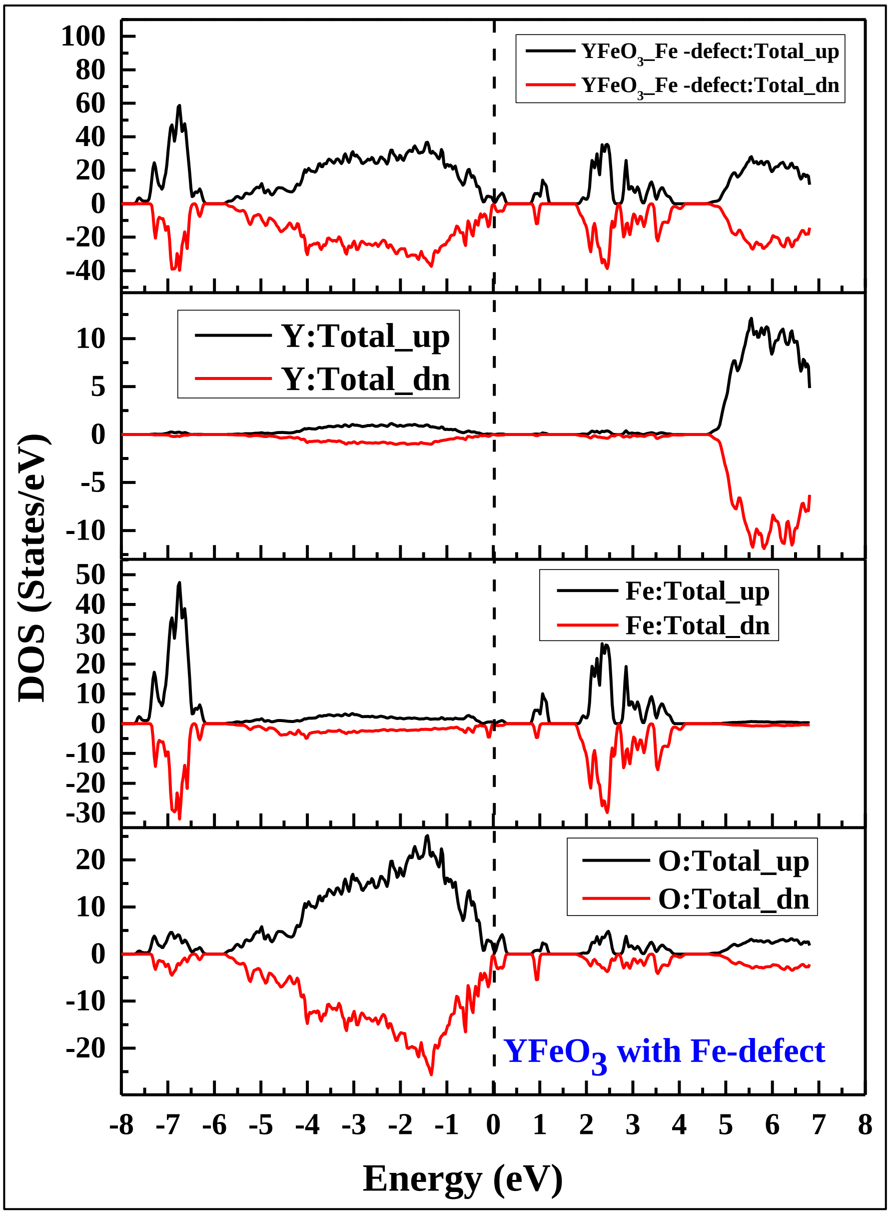

Figure 5.9: *Partial and total density of States of Fe-defect* $YFeO_3$ *samples.*

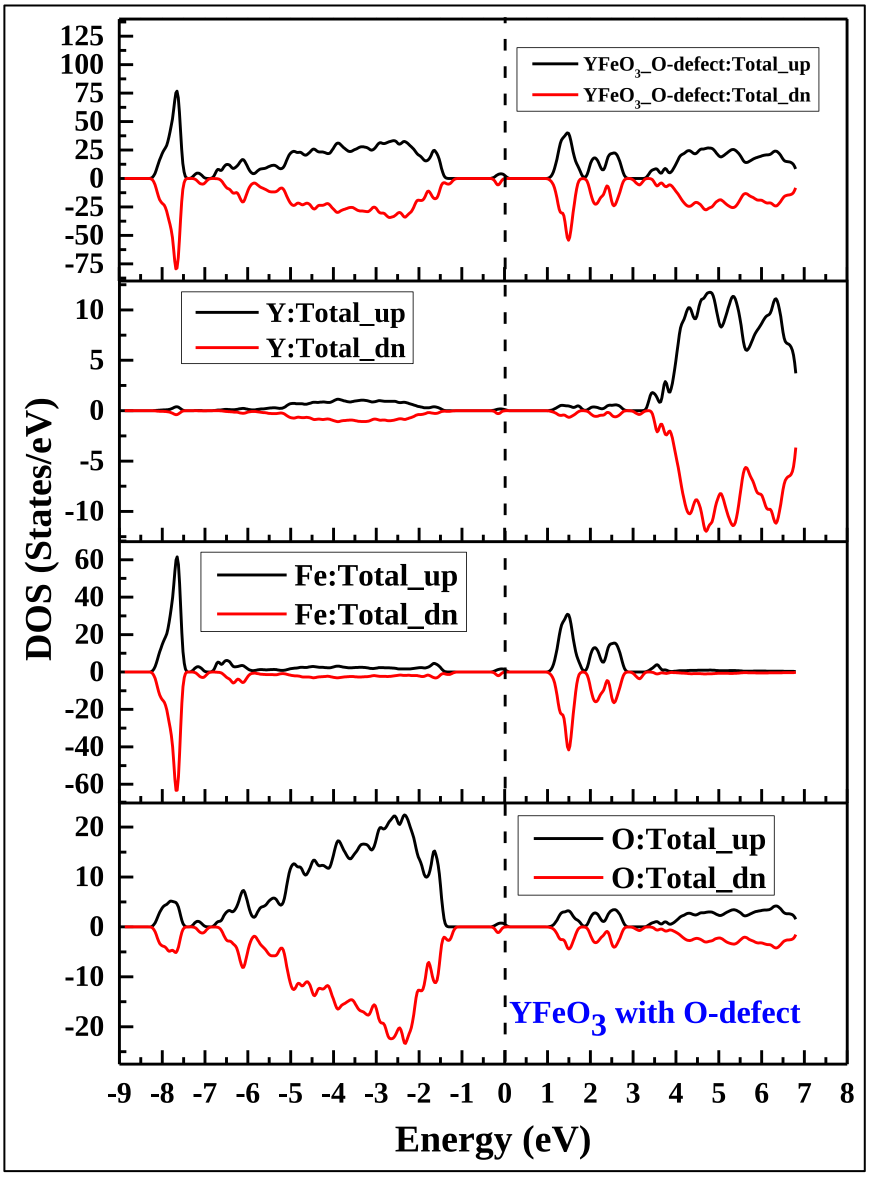

Figure 5.10: *Partial and total density of States of O-defect* $YFeO_3$ *samples.*

Figures 5.8-5.10 show the total and partial DOS for Y, Fe and O deficient $YFeO_3$ for a spin up and down states respectively. From these figures, it is clear that there exists a net magnetization in Y, Fe, and O deficient $YFeO_3$ and these results are in agreement with earlier reports on a similar system, for example, $BiFeO_3$[193]. Thus, it appears that self-doping (i.e. point defects) may also result in net magnetization other than canting of spins. The corresponding values of net magnetic moment per unit cell are given in Table 5.2. Further, from the DOS plots, it is clear that in case of the defect at Y and Fe-site the maximum contribution to the magnetism is essentially coming from Fe orbitals.

Table 5.2: D*efect models and corresponding net magnetic moments*

Sample	**$YFeO_3$**	**Y-defect $YFeO_3$**	**Fe-defect $YFeO_3$**	**O-defect $YFeO_3$**
Magnetic Moments (μ_B)	**0.000**	**1.0352**	**5.9991**	**0.0001**

At this juncture, it is important to note that the occurrence of ferromagnetism demands mixed valence of Fe ions according to Zener-double exchange mechanism[194] or the virtual electron transfer from a half-filled to an empty orbital or from a filled to a half-filled orbital, as per Goodenough Kanamori rule [195, 196]. Hence, in order to search for the possible mechanism for the observed magnetic moment, we have investigated the effect of point defects on the charge states (Bader charges) of Y, Fe and O ions using AIM theory with Critic2 code [60].

Table 5.3 shows the atomic charges and corresponding magnetic moments for pure and defected $YFeO_3$ systems. It reveals that with the defect at Y, Fe, and O-site there is a change in the charge/valence state of Fe ions. Further, it is clear that the magnetic moments of Fe near the defect site (as indicated by colors) show significant variation suggesting that maximum contribution to the magnetic moment is due to Fe ions. For Y and Fe deficient $YFeO_3$, the oxidation state of Fe appears to increase whereas, for oxygen deficient sample the oxidation state of Fe appears to decrease. Further, for Y and Fe deficient $YFeO_3$ decrease in the oxidation state of oxygen anions has been observed. This decrease in the oxidation state of oxygen anions suggests the possibility of O-2p ligand hole at oxygen site. The presence of this ligand hole at oxygen site is known to results into the extreme valency of Fe i.e. in Fe in +4 states. The evidence of O-2p ligand hole is experimentally observed earlier[197-200]. This suggests that due to self-doping there is a change in the valency of Fe ions especially near the defect sites (as indicated by colors). This may result in the ferromagnetism due to Zener double exchange mechanism[194].

Table 5.3: *Bader charge analysis and magnetic moments of individual atoms of pure and various defect of* $YFeO_3$ *samples. The change in charge and magnetic moments of atom associated with various defect have been marked in color and bold fonts.*

No.	**Atom**	**No defect**		**Y-defect**		**Fe-defect**		**O - defect**	
		Charge |e|	**Magnetic Moments (μ_B)**	**Charge |e|**	**Magnetic Moments (μ_B)**	**Charge |e|**	**Magnetic Moments (μ_B)**	**Charge |e|**	**Magnetic Moments (μ_B)**
1	Y 1	2.17	0	2.19	0.00013	2.18	0.00118	2.17	0.00021
2	Y 2	2.17	0	2.17	0.00209	2.18	0.0001	2.18	0.00001
3	Y 3	2.17	0	2.16	0.00124	2.17	-0.00112	2.17	0.00003
4	Y 4	2.17	0	2.17	0.00273	2.17	0.00227	2.17	0.00002
5	Y 5	2.17	0	2.17	0.00005	2.19	-0.00266	**2.11**	0.00731
6	Y 6	2.17	0	**Defect**		**2.19**	**0.00679**	2.18	-0.00039
7	Y 7	2.17	0	2.17	-0.00001	**2.19**	**-0.00246**	**2.10**	-0.01337
8	Y 8	2.17	0	2.17	0.00016	**2.19**	**-0.00237**	**2.13**	-0.00189
9	Y 9	2.17	0	2.17	0.00066	2.18	0.0003	2.18	-0.00001
10	Y 10	2.17	0	2.17	-0.00004	**2.18**	**-0.00413**	2.17	0.00025
11	Y 11	2.17	0	2.18	0.00022	2.17	-0.00007	2.18	-0.00041
12	Y 12	2.17	0	2.18	0.0006	2.18	0.00003	2.18	0.00016
13	Fe1	1.84	4.06956	1.67	3.52223	1.84	4.11985	1.81	4.10164
14	Fe2	1.84	-4.06956	1.83	-4.07197	1.84	-4.09684	1.82	-4.10136
15	Fe3	1.84	4.06956	**1.84**	**4.03531**	1.84	4.11834	1.82	4.10151
16	Fe4	1.84	-4.06956	1.82	-4.07919	1.84	-4.12017	1.81	-4.10152
17	Fe5	1.84	4.06956	1.84	4.00233	1.817	3.92261	1.81	4.10247
18	Fe6	1.84	-4.06956	1.86	-4.05762	**Defect**		**1.35**	-3.78576
19	Fe7	1.84	4.06956	**1.86**	**4.05258**	**1.66**	**-3.16815**	1.81	4.09887
20	Fe8	1.84	-4.06956	**1.84**	**-3.98924**	1.84	4.10501	1.81	-4.10064
21	Fe9	1.84	4.06956	1.84	4.09588	1.81	-3.91823	**1.27**	3.79825
22	Fe10	1.84	-4.06956	1.83	-4.08395	1.84	4.12311	1.81	-4.10103
23	Fe11	1.84	4.06956	1.84	4.09678	1.84	-4.11997	1.82	4.10109
24	Fe12	1.84	-4.06956	1.83	-4.09653	1.83	4.08179	1.81	-4.10046
25	O 1	-1.34	0.01873	-1.30	-0.02687	-1.30	-0.03019	-1.33	0.01746
26	O 2	-1.34	0.01873	-1.25	0.02454	-1.34	0.02181	-1.33	0.01754
27	O 3	-1.34	-0.01873	-1.20	-0.09823	**-1.32**	**-0.02659**	-1.33	-0.01894
28	O 4	-1.34	-0.01873	-1.29	0.02753	-1.33	-0.01847	-1.33	-0.01905
29	O 5	-1.34	0.01873	-1.32	-0.02632	-1.34	0.02079	-1.33	0.01907
30	O 6	-1.34	0.01873	**-1.21**	**-0.07237**	-1.34	0.17145	-1.33	0.01705
31	O 7	-1.34	-0.01873	-1.33	-0.03009	-1.34	-0.021	-1.33	-0.01759
32	O 8	-1.34	-0.01873	**-1.31**	**0.01704**	-1.34	0.15897	-1.33	-0.01969
33	O 9	-1.34	0.01873	-1.33	0.0374	-1.07	0.17463	**Defect**	
34	O 10	-1.34	0.01873	**-1.19**	**-0.04954**	**-1.07**	**-0.16321**	-1.34	0.06033
35	O 11	-1.34	-0.01873	-1.33	0.00308	**-1.10**	**0.09217**	-1.35	-0.01384
36	O 12	-1.34	-0.01873	**-1.032**	**0.3059**	-1.13	0.02493	**-1.35**	0.00586
37	O 13	-1.34	0.01873	-1.03	-0.30784	-1.26	0.00371	-1.33	0.01981
38	O 14	-1.34	0.01873	-1.33	-0.00274	-1.26	-0.00378	-1.33	0.01803
39	O 15	-1.34	-0.01873	-1.18	0.04957	-1.28	0.01749	-1.33	-0.01786
40	O 16	-1.34	-0.01873	-1.33	-0.03621	-1.29	-0.00013	**-1.35**	**-0.01634**
41	O 17	-1.34	0.01873	-1.28	0.02615	-1.35	0.16721	-1.33	0.02085
42	O 18	-1.34	0.01873	-1.34	0.01127	-1.30	0.03944	-1.34	-0.02058
43	O 19	-1.34	-0.01873	-1.30	0.01258	-1.34	0.16831	-1.33	-0.01754
44	O 20	-1.34	-0.01873	-1.33	-0.02438	-1.32	0.04664	-1.35	-0.02395
45	O 21	-1.34	0.01873	-1.34	0.02372	-1.34	-0.02669	-1.33	0.01542
46	O 22	-1.34	0.01873	-1.34	0.01517	-1.35	-0.16404	-1.33	0.01854
47	O 23	-1.34	-0.01873	-1.34	-0.01321	-1.34	0.01238	-1.33	-0.02247
48	O 24	-1.34	-0.01873	-1.34	-0.01782	-1.35	-0.16515	-1.33	-0.01829
49	O 25	-1.33	0	-1.27	0.00389	-1.33	0.0009	-1.32	-0.00026
50	O 26	-1.33	0	**-1.11**	**-0.04618**	-1.31	0.13233	-1.32	-0.00090
51	O 27	-1.33	0	-1.32	-0.00396	-1.33	0.00428	-1.32	0.00027
52	O 28	-1.33	0	**-1.06**	**-0.2365**	-1.33	0.00381	-1.32	0.00022
53	O 29	-1.33	0	-1.27	0.00671	-1.30	0.13292	-1.32	-0.00069
54	O 30	-1.33	0	-1.33	-0.00007	-1.31	0.00285	**-1.33**	**-0.02590**
55	O 31	-1.33	0	-1.30	-0.0008	**-1.05**	**-0.02315**	**-1.33**	0.03272
56	O 32	-1.33	0	**-1.28**	**-0.00001**	-1.05	-0.07444	**-1.34**	**0.02179**
57	O 33	-1.33	0	-1.33	-0.0001	-1.32	0.00122	**-1.33**	**-0.02992**
58	O 34	-1.33	0	-1.27	0.0049	-1.33	0.00049	-1.32	-0.00030
59	O 35	-1.33	0	-1.32	-0.00153	-1.33	0.00205	-1.32	0.00185
60	O 36	-1.33	0	-1.33	0.00126	-1.33	0.00635	-1.32	0.00112

5.4 Summary

The structural distortion-parameters of $RFeO_3$ samples obtained from refinement and compared with the results extracted from modern Bond valance sum model (SPuDS) and with density functional theory (DFT) using WIEN2k package and found to be consistent with experimental results. The first-principle study suggests that the optical band gap in $RFeO_3$ appears to be independent of structural parameters such as lattice constants and R-O bond length whereas, it seems to be controlled by Fe-O bond length i.e. the overlap between Fe-3d and O-2p orbitals in $RFeO_3$ samples. The density functional theory also has been used to demonstrate the possible origin of ferromagnetism in $YFeO_3$. The study reveals that Y and Fe site vacancy (point defects) may lead to the net magnetic moments in the $YFeO_3$ system. Bader charge analysis suggests the mixed valence state of Fe in Y, Fe, and Oxygen deficient system which may be responsible for Zener double exchange mechanism leading to the ferromagnetism.

Chapter 6

Possible Origin of d-d Transitions in $RFeO_3$ ($3d^5$) Systems: Experiments and Theory

Present chapter deals with the possible origin of d-d transitions in the optical absorption spectra of $RFeO_3$ samples. It has been observed that the presence of peak due to d-d transition is associated with the annealing temperatures driven defects present in these samples. Our experimental and theoretical analysis suggests that the non-stoichiometry present in samples is the main origin of d-d transitions peak in the optical spectra of $RFeO_3$ samples and so does in d^5 systems[4].

6.1 Introduction

ABO_3 type perovskites with B as a transition metal ion witness of the splitting of d orbitals into two sub-orbitals t_{2g} (d_{xz}, d_{yz}, d_{xy}) and e_g (d_{z2}, d_{x2-y2}) due to crystal fields of BO_6 octahedra known as crystal field splitting. The transition of electrons from t_{2g} to e_g orbitals is termed as d-d transitions. The signature of the above said d-d transition is generally visible in optical absorption spectroscopy as in most of the cases the values of the crystal field splitting is around 1.0eV to 2eV. Generally, it is observed that in the case of the optical absorption spectroscopy the strength of the d-d transitions for the d^5 system is nearly thousand times

---

[4] ***M Kamal Warshi et al.,*** Possible Origin of d-d Transitions in $RFeO_3$ ($3d^5$) Systems: Experiments and Theory. **(Under Review)**

weaker than that of the main excitonic peak i.e. dipole-allowed p-d transitions (O-2p and Fe-3d)[90]. At this moment, it is important to note that in $RFeO_3$ systems, Fe ion occupy 3+ oxidation state i.e. $RFeO_3$ is a Fe^{3+} (d^5) system and d^5 orbital splits into t_{2g} and e_g sub-orbitals due to crystal field of FeO_6 octahedra. Interestingly, in d^5 systems, d-d transitions are forbidden not only according to electric dipole selection rule ($\Delta l = \pm 1$) but also according to spin selection rule ($\Delta S = 0$), in this way one may easily understand the absence of d-d transitions in optical spectra of d^5 systems. The presence of strong spin-orbit coupling may relax these relaxation rule but, in this case, also the intensity of d-d transition is very week i.e. ~ 10^3 times weaker than the main excitonic peak. In recent years optical absorption spectroscopy has been widely used to probe the electronic structure of various transition metal oxides[91] and it is also known to probe both the band gap as well as the d-d transitions in transition metal oxide complexes including d^5 systems [170, 201, 202]. The optical spectra of $RFeO_3$ samples have been found to be dominated by the exchange interaction of Fe-3d and O-2p orbitals (p-d transitions) as well as the crystal field splitting of Fe 3d orbitals [203]. Thus, in this chapter, we have investigated the possible origin of the signature of d-d transitions in optical absorption spectra of d^5 systems. It has been observed that the presence of non-stoichiometry as a most prominent origin of d-d transitions in optical absorption spectra of d^5 systems like $RFeO_3$. In strong support of our experimental claim, the theoretical investigations have been carried out on the $YFeO_3$ system as a case study. The results are further supported with the x-ray absorption near edge structure (XANES) at Fe K-edge, and soft x-ray absorption spectroscopy (SXAS) at Fe $L_{2,3}$-edges spectra of polycrystalline pure and self-doped $YFeO_3$ powders synthesized at a different temperature. DRS spectra of $Y_{0.97}FeO_3$ (Y-defect $YFeO_3$), $YFe_{0.97}O_3$ (Fe-defect $YFeO_3$) synthesized using the sol-gel method and of a nearly defect-free polycrystalline $YFeO_3$ powders prepared using hydrothermal synthesis method have also been acquired. Simultaneously, theoretical optical absorption spectra considering various defects in the $YFeO_3$ system (such as Y, Fe, and O-defects) have been generated using density functional theory (DFT) implemented in WIEN2k package [122, 204].

6.2 Experimental Details

Polycrystalline samples of $YFeO_3$ were prepared *via* sol-gel synthesis method, the detail of synthesis methodology is already reported elsewhere [203] and discussed in chapter 2 of this thesis. In order to investigate the effect of annealing temperature on the intensity of d-d transition the samples prepared by sol-gel method i.e. the gel obtained at the end of sol-gel synthesis was dried at 400 ^oC to get the precursors of $YFeO_3$ sample. The precursors obtained have been annealed at different temperatures such as 600 ^oC, 700 ^oC, 800 ^oC, 1000 ^oC, 1200 ^oC and 1300 ^oC; let's call these as YFO_600, YFO_700, YFO_800, YFO_1000, YFO_1200 and YFO_1300 respectively. In order to investigate the effect of self-doping $Y_{0.97}FeO_3$ and $YFe_{0.97}O_3$ samples have also been prepared using sol-gel synthesis method and these samples have been annealed at 800 ^oC. The obtained results have been also verified on the samples prepared by solid-state reactions method [205] were used to synthesize the polycrystalline samples of $YFeO_3$; for this Y_2O_3 (99.998%) and Fe_3O_4 (99.999%) have been taken as starting materials. Y_2O_3 were preheated at 400 ^oC before weighing as it is a hygroscopic material. The stoichiometric amount of starting materials was mixed and ground in propanol medium to get a homogeneous mixer. Then it calcined at 900 ^oC, 1250 ^oC, for 24 h and finally sintered at 1350 ^oC for 24 h in air. From hereafter we call $YFeO_3$ as YFO_SSR.

Furthermore, a nearly defect-free $YFeO_3$ sample was prepared using the hydrothermal synthesis method [60]. In this method, Yttrium nitrate hexahydrate $Y(NO_3)_3$. $6H_2O$ (99.99 %, Alfa Assar) and Iron nitrate nonahydrate $Fe(NO_3)_3$. $9H_2O$ (99.95 %, Aldrich) and Potassium hydroxide were taken as starting materials. $Y(NO_3)_3$. $6H_2O$ and $Fe(NO_3)_3$. $9H_2O$ were dissolved in 15 mL deionized in such an amount that each reaches to a molar concentration of 0.4M. These solutions were mixed at room temperature, and KOH pallets were added into the mixer and stirred on magnetic stirrer to get the concentration of 20M. The final mixer was transferred to an autoclave containing 50mL Teflon-liner for crystallization under autogenous pressure at 220 ^{o}C for 12 h. Then it was naturally cooled to room temperature and the solid precipitate was obtained and filtered. The powder was then washed with deionized water and dried in air at 100 ^{o}C to get the final $YFeO_3$ compound. Let's name it YFO_H as it has been synthesized *via* a hydrothermal synthesis method.

The powder x-ray diffraction (XRD) experiments have been carried out using Bruker D8 advanced diffractometer equipped with Cu K_{α} to examine the structural phase purity of the prepared samples. The soft X-ray absorption spectroscopy (SXAS) at Fe $L_{2,3}$-edges and x-ray absorption near edge structure (XANES) at Fe K-edge measurements have been done on beamline (BL)-1 and BL-12 respectively of synchrotron radiation Centre, Indus-II, Raja Ramanna Centre for Advanced Technology Indore, India. Defused Reflectance Spectra (DRS) of prepared $RFeO_3$ samples were collected in the spectroscopic range of 800-200 nm using a high precision spectrophotometer Carry 60 UV-Vis (Agilent). A diffuse reflectance probe (Harrick Video-Barrelino) attached to the spectrophotometer was used to acquire the data.

6.3 Theoretical Details

The first principle calculations have been carried out using the full-potential linearized augmented plane wave (FP-LAPW) method within the density-functional theory (DFT)[116, 118]. The generalized gradient approximation (Predew-Burke-Ernzerhof) (GGA-PBE)[123] has been used as an exchange-correlation potential as implemented in WIEN2k package[122], all the technical detail about the calculation such as size of supercell, defect models created, and calculations of formation energies have been reported[120] and also discussed in chapter 2, section 2.3. One step ahead of these details we have used the optic calculation[204] as implemented in WIEN2k package to generate the optical absorption spectra of $YFeO_3$ and its various defect models.

6.4 Results and Discussions

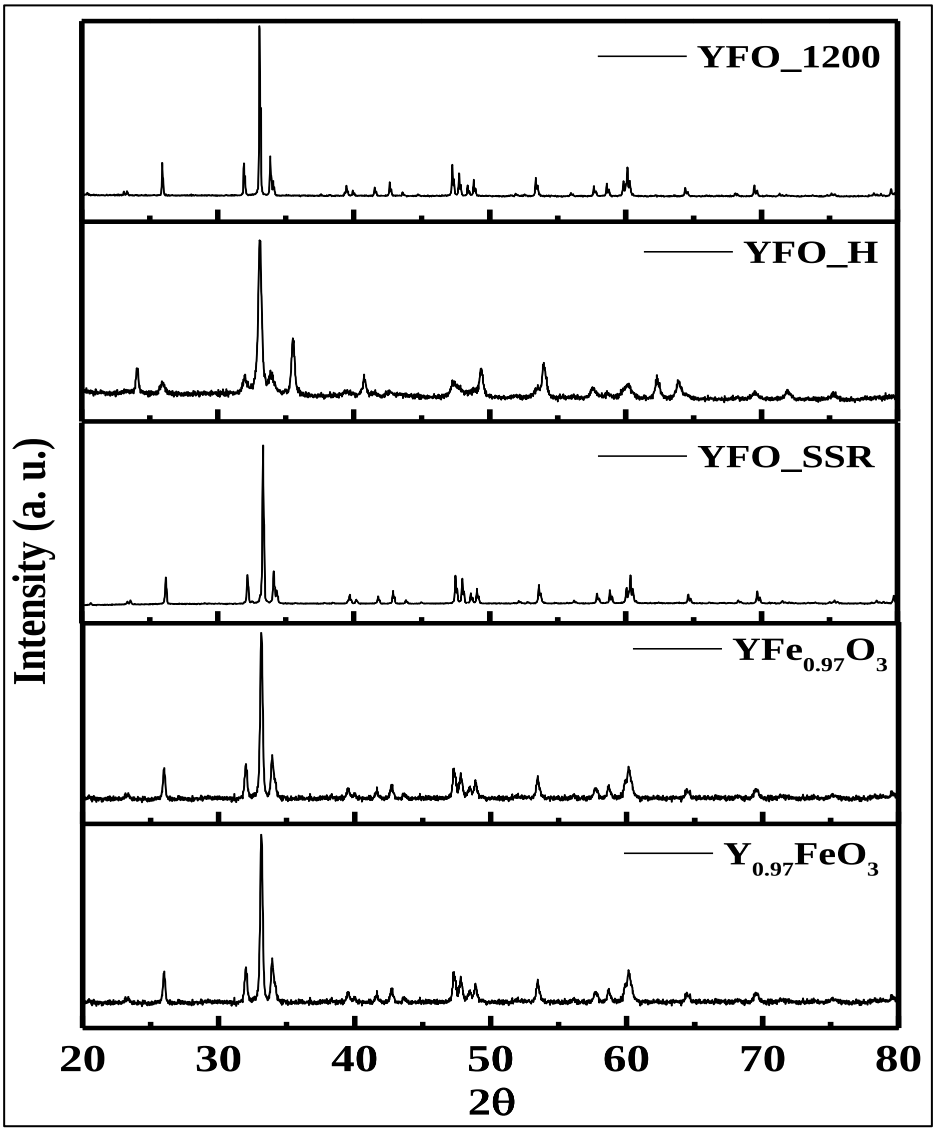

Figure 6.1: *X-ray diffraction pattern as prepared $YFeO_3$ samples. YFO_1200, YFO_H, YFO_SSR represent the XRD patterns of a representative of $YFeO_3$ samples prepared via sol-gel method and annealed at different temperatures, Hydrothermal, and solid-state reaction methods respectively, while the bottom two signifies the XRD patterns of self-doped samples.*

Figure 6.1 shows the XRD pattern of all $YFeO_3$ samples prepared *via* different methods. YFO_1200, YFO_H, and YFO_SSR are presented as a representative of XRD patterns of $YFeO_3$ samples prepared using sol-gel method annealed at different temperatures, solid-state reaction and hydrothermal methods respectively. $Y_{0.97}FeO_3$ and $YFe_{0.97}O_3$ represent XRD patterns of self-doped $YFeO_3$ samples i. e. of

Y and Fe defects. It is clear from the figures that no impurities were present in the prepared samples. All prepared samples hold an orthorhombic crystal structure with space group Pbnm[203].

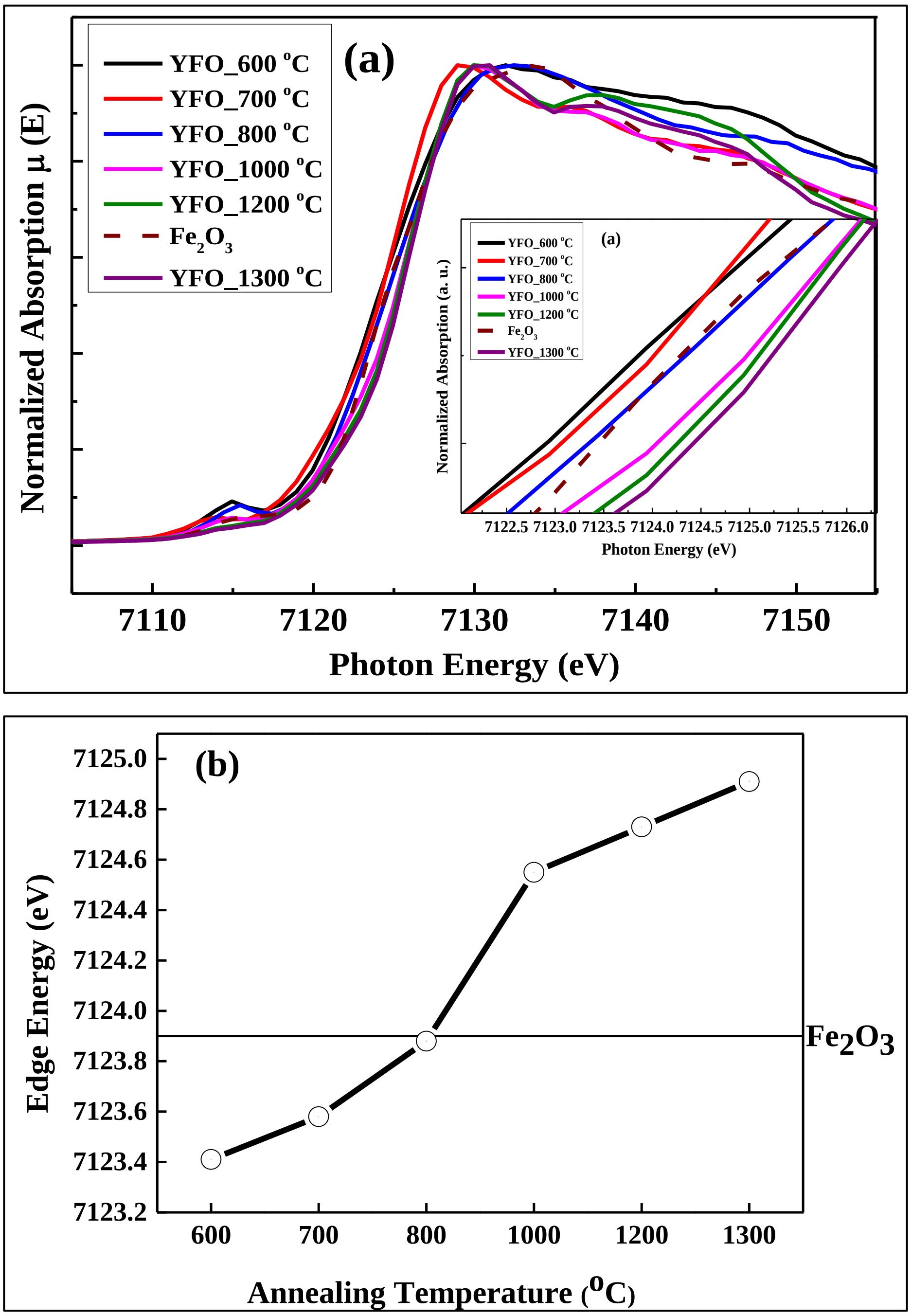

Figure 6.2: *(a) XANES spectra of $YFeO_3$ samples annealed at different temperatures along with Fe_2O_3 as a standard, (b) shift of edge energies as a function of annealing temperatures.*

In Figure 6.2 (a), the Fe K-edge XANES spectra of $YFeO_3$ samples annealed at different temperatures along with XANES spectra of Fe_2O_3 as a standard of Fe^{3+} have been shown. From Figure 6.2 (a) it has been observed that the energy edges in XANES spectra of $YFeO_3$ samples annealed at 600 ^oC, 700 ^oC are lower in energy than that of edge energy of Fe in Fe_2O_3 XANES spectra which suggest that in these sample Fe are in mixed oxidation states of Fe^{2+} and Fe^{3+}. Likewise, the oxidation state of Fe in $YFeO_3$ sample annealed at 800 ^oC have been found very close to standard Fe^{3+} and the oxidation states of Fe in $YFeO_3$ samples annealed at temperatures higher than 800 ^oC, i.e. at 1000 ^oC, 1200 ^oC and 1300 ^oC have been found in the mixed valence state of Fe^{3+} and Fe^{4+}. The inset of Figure 6.2 (a) shows the zoomed section of XANES spectra in order to visualize the shift in edge energy with increasing annealing temperatures.

The variation of edge energies of Fe in $YFeO_3$ samples as a function of annealing temperatures along with edge energy of Fe in Fe_2O_3 have been shown in Figure 6.2 (b). The Fe edge energy of sample annealed at 800 ^oC has been found very close to that of Fe_2O_3 so that the oxidation state of Fe in YFO_800 could be considered very close to 3+. It has been also observed that below the annealing temperature 800 ^oC Fe in $YFeO_3$ samples remains in the mixed oxidation state of 2+ and 3+ and above the annealing temperature 800 ^oC, $YFeO_3$ samples contain Fe as a mixed oxidation state of 3+ and 4+. The oxidation states of Fe in $YFeO_3$ samples increases with increasing annealing temperature as edge energies have been found to be shifted towards higher energies with increasing annealing temperatures, i. e. $YFeO_3$ samples contain a different percentage of Fe^{2+}, Fe^{3+} and Fe^{4+} species for different annealing temperatures. Thus, there is a significant effect of annealing temperatures on the oxidation state of Fe ions have been found and so does the valency of Fe in $YFeO_3$ samples is highly dependent on sintering temperatures. It is important here to note that as the XANES standard for Fe^{4+} is not available hence in the present case we have not attempted to calculate the exact concentration of Fe^{3+} versus Fe^{4+}.

The Fourier transform of diffuse reflectance spectra of $YFeO_3$ samples annealed at different temperatures, its various defects, and prepared *via* different methods as a function of wavelengths have been shown in Figures 6.3, 6.4, and 6.5 respectively. The obtained spectra were converted into absorption spectra using Kubelka-Munk equation [107, 108] as demonstrated in our earlier reports[165, 166, 203], $[F(R_\infty)*h\nu]^{0.5}$ versus photon energy (E) plot of the recorded diffused reflectance spectra of $YFeO_3$ samples annealed at different temperatures have been shown in Figure 6.6. In Figure 6.3, an appearance of intense band feature around 600-700 nm in DRS spectra of $YFeO_3$ samples has been assigned to a strong dipole forbidden d-d transition, which is well-known for orthoferrites [206, 207]. Another possibility for the emergence of this peak is due to localized defect states between conduction and valence band, this aspect needs detail experimental and theoretical investigations.

Further, for the case of Fe^{3+} ions or d^5 systems ($RFeO_3$), the d-d transition should be forbidden according to dipole selection rule ($\Delta\ell = \pm1$) as well according to spin selection rule ($\Delta S = 0$)[90]. However, spin selection rule may be relaxed due to the spin-orbit coupling for the case of $RFeO_3$ systems [208, 209], but most importantly the intensity of the spin-forbidden d-d transition is expected to be much weaker than that of spin allowed transition [90]. Whereas; the intensity of d-d transitions observed for the present case of $YFeO_3$ (see Figure 6.3) is clearly visible and much higher than expected [90] which suggests the occurrence of a forbidden d-d transition in presently prepared $YFeO_3$ samples. In the inset of Figure 6.3, the variation of d-d transitions with increasing annealing temperatures of $YFeO_3$ samples have been shown. For the samples YFO_600, YFO_700, and YFO_800 an absence of d-d transition was observed, at the same time for samples YFO_1000, YFO_1200, and YFO_1300, d-d transitions have been observed and it is found to have stronger in intensity and broader in width with increasing annealing temperatures. It is important to note here that the analysis of Fe-K edges XANES spectra of $YFeO_3$ samples annealed at different temperatures reveals the increase in the percentage of 4+ oxidation state of Fe ions as we increase the annealing temperature. Thus, the non-stoichiometry present in the sample in terms of Fe^{4+}/ Fe^{3+} might be the possible origin of d-d transition in the present case ($RFeO_3$) systems allowed *via* the spin-selection rule.

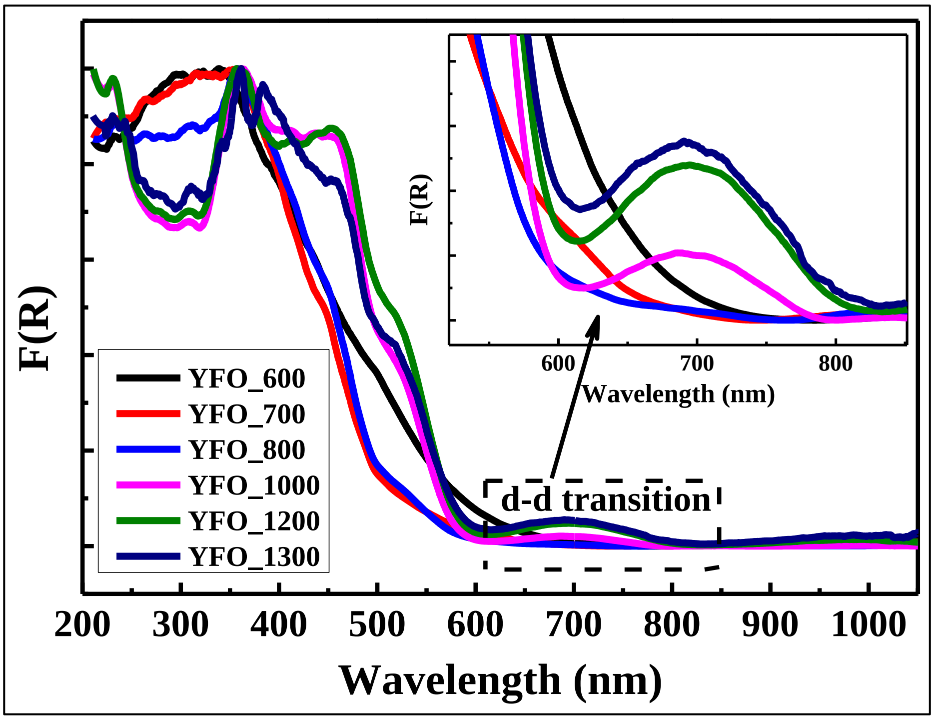

Figure 6.3: *Diffuse reflectance spectra from $YFeO_3$ samples annealed at different temperatures.*

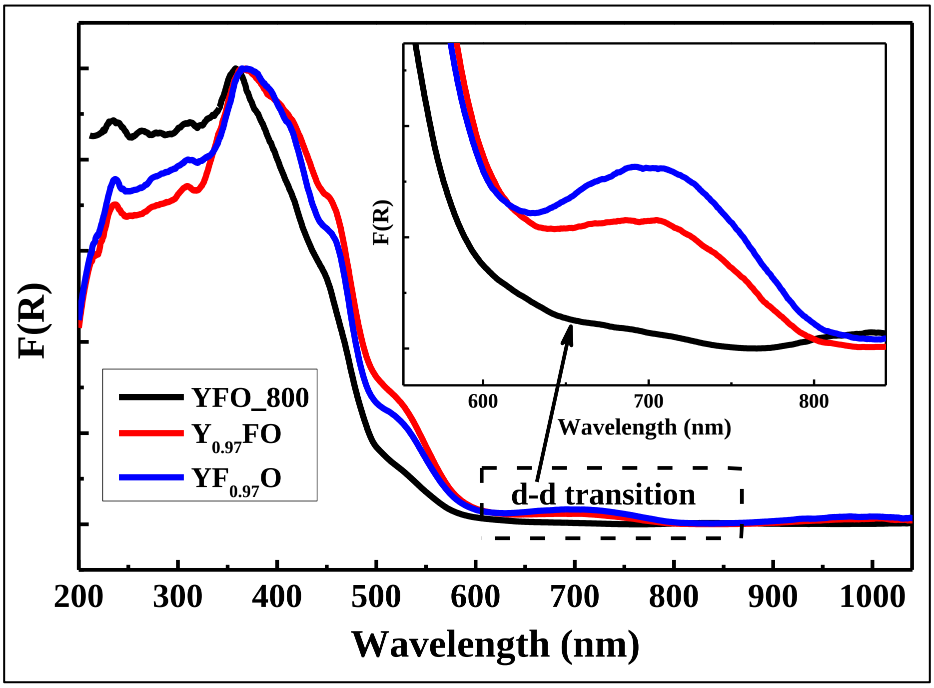

Figure 6.4: *Diffuse reflectance spectra from Y-defect, and Fe-defect along with pure $YFeO_3$ samples annealed at 800 °C.*

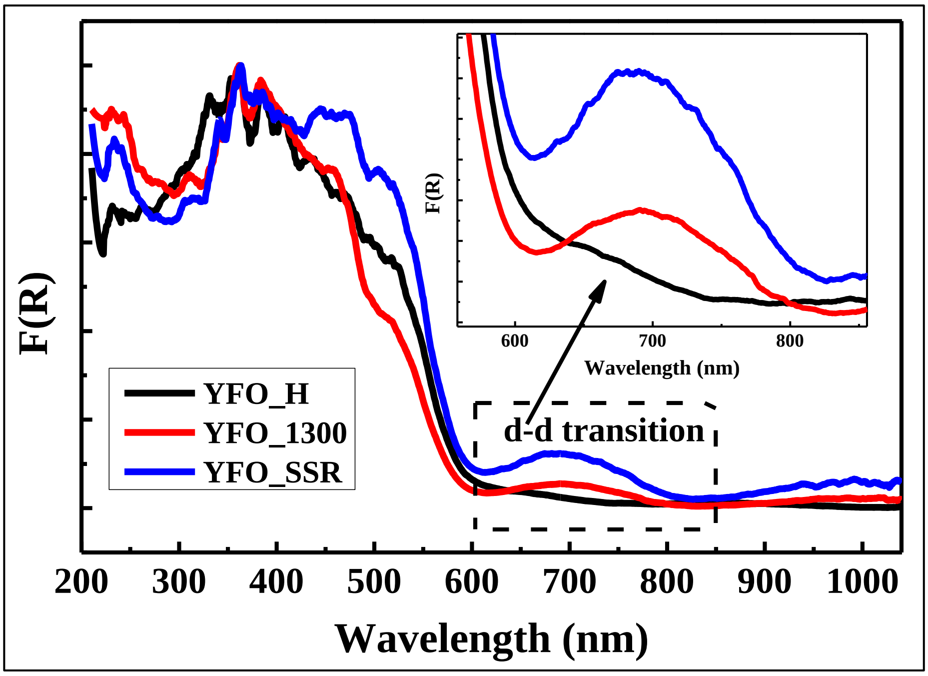

Figure 6.5: *Diffuse reflectance spectra from YFeO$_3$ samples prepared through different synthesis methods such as solid-state reaction, sol-gel, and Hydrothermal synthesis.*

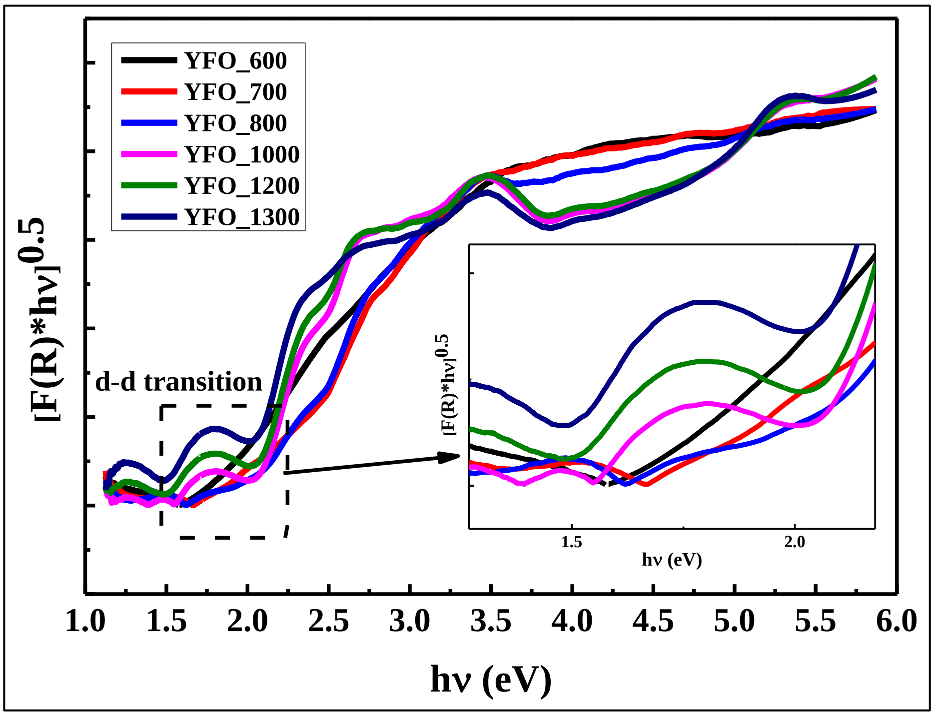

Figure 6.6: *Optical absorption spectra derived from diffused reflectance spectra by using the Kubelka-Munk equation of YFeO$_3$ samples annealed at different temperatures.*

To further confirm the role of the non-stoichiometry present in the sample and to understand the nature of d-d transition discussed above, we synthesized another set of samples with defects at the various site. In this way, $Y_{0.97}FeO_3$ and $YFe_{0.97}O_3$ were prepared *via* sol-gel synthesis method as a representative of Y-defect and Fe-defect $YFeO_3$ samples. To avoid the presence of non-stoichiometry (excess/defect) in terms Oxygen, these samples finally sintered at 800 ^oC as we have discussed above higher sintering temperature results in mixed valency of Fe ions (Fe^{3+}/Fe^{4+}). We have acquired the diffuse reflectance spectra of these samples and shown in Figure 6.4 together with the diffuse reflectance spectra of YFO_800 sample as a function of wavelengths. From this figure, it is very clear that the intensity of d-d transition of $YFeO_3$ sample either absent or negligible as compared to that of self-doped $Y_{0.97}FeO_3$, and $YFe_{0.97}O_3$ samples which is expected because we hoped $YFeO_3$ as a d^5 system. Thus, the analysis of diffuse reflectance spectra in Figure 6.4 reveals that there is a prominent strength of d-d transition in self-doped samples as compared to pure $YFeO_3$ samples annealed at 800 ^oC. Thus, by this attempt, we are able to conclude that the non-stoichiometry present in samples affects the strength of d-d transitions. Further, we have made another attempt in which hydrothermal synthesis method was used to synthesize nearly stoichiometry sample of $YFeO_3$ sample. As the hydrothermal synthesis method is a low-temperature synthesis process, it is expected to maintain more stoichiometry than the other two methods with relatively high-temperature synthesis process as described above. The diffuse reflectance spectra have been acquired and shown in Figure 6.5 along with the so-called prepared stoichiometry samples via solid-state reaction and sol-gel methods. From Figure 6.5, almost an absence of d-d transition could be observed in the sample synthesized *via* hydrothermal synthesis method as compared to the other two samples. Thus, again one can say that the non- stoichiometry present in the sample (in the form of various defect or excess) is the most possible origin of d-d transition in d^5 systems like $RFeO_3$.

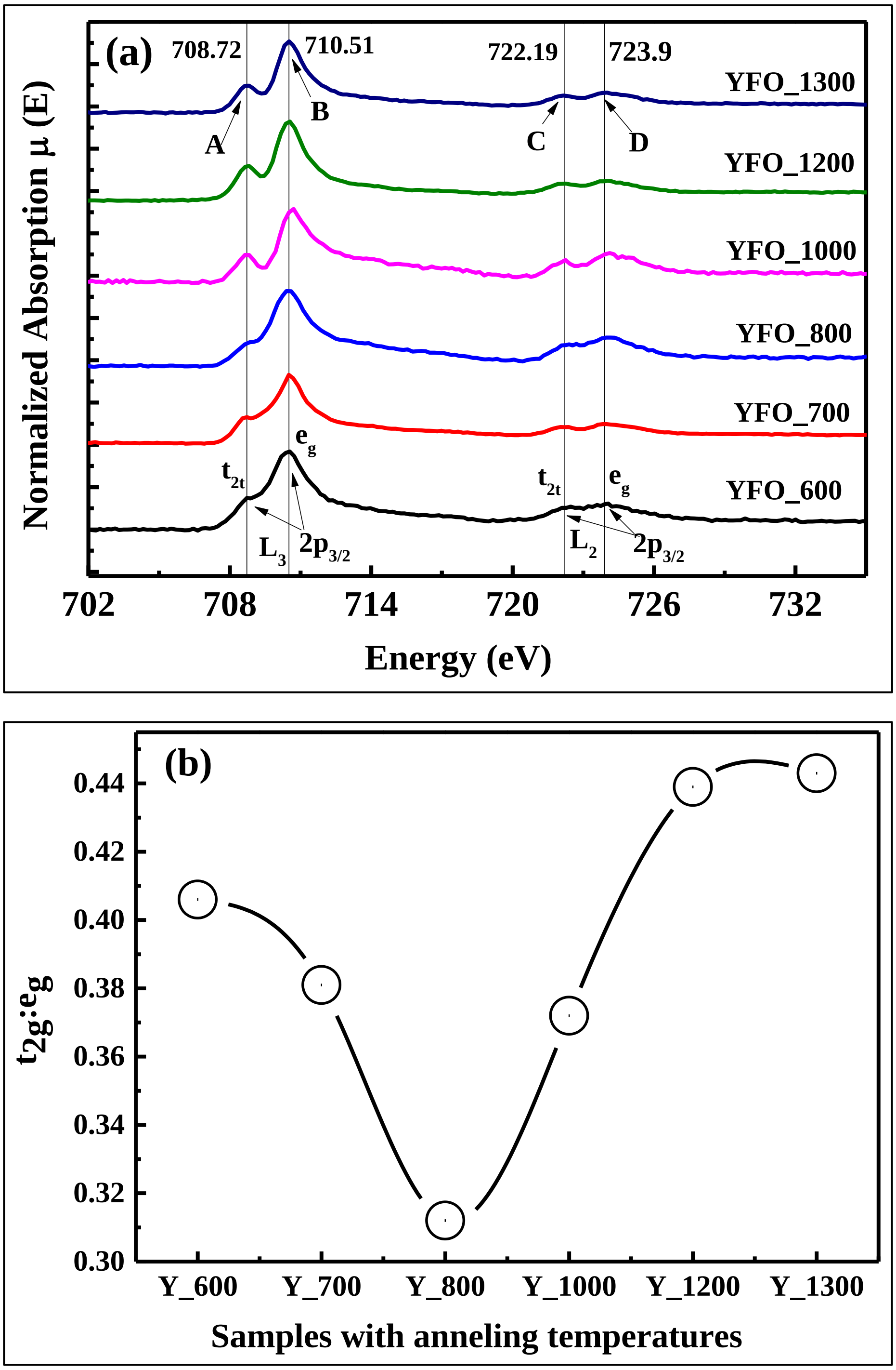

Figure 6.7: *(a) SXAS spectra of* $YFeO_3$ *samples annealed at different temperatures, (a)* t_{2g}/e_g *intensity ratios of these samples.*

Moreover, the Fe $L_{2,3}$-edge SXAS spectra of the $YFeO_3$ samples annealed at different temperature have been acquired to probe the d-d transition more insight and accurate; shown in Figure 6.7(a). These spectra essentially signify the transition from Fe $2p_{3/2}$ and $2p_{1/2}$ to Fe 3d orbitals and assigned as L_3 and L_2 respectively and their centroids are found to be separated by around 13 eV due to spin-orbit coupling. The octahedral crystal field splitting and multiplet effects further split L_3 into A and B and L_2 splits into C, D. The peak A at 708.72eV and peak B at 710.51eV assigned to arise from transitions $2p_{3/2}$ to Fe 3d (t_{2g}) and Fe 3d (e_g) orbitals respectively [202]. The L_2 edge transition further split into C at 722.19 eV and D at 723.9 eV and have been assigned to transition from $2p_{1/2}$ to Fe 3d (t_{2g}) and $2p_{1/2}$ to Fe 3d (e_g) respectively.

We have estimated the t_{2g}/e_g (A/B) intensities ratios using $L_{2,3}$ SXAS spectra of $YFeO_3$ samples and shown in Figure 6.7(b). The intensity ratio of $YFeO_3$ samples observed to be varied according to parabola keeping YFO_800 at the center. This signifies that the intensity of d-d transitions will be strong no matters either Fe is in the mixed oxidation state of 3+/2+ or in 3+/4+. The absence of the d-d transition in diffuse reflectance spectra of samples YFO_600 and YFO_700 in which Fe ions are in mixed oxidation states of 3+/2+ (see Figure 6.2(a)), might be due to insufficient energy region of spectrophotometer we have, and this may be the subject of further investigation.

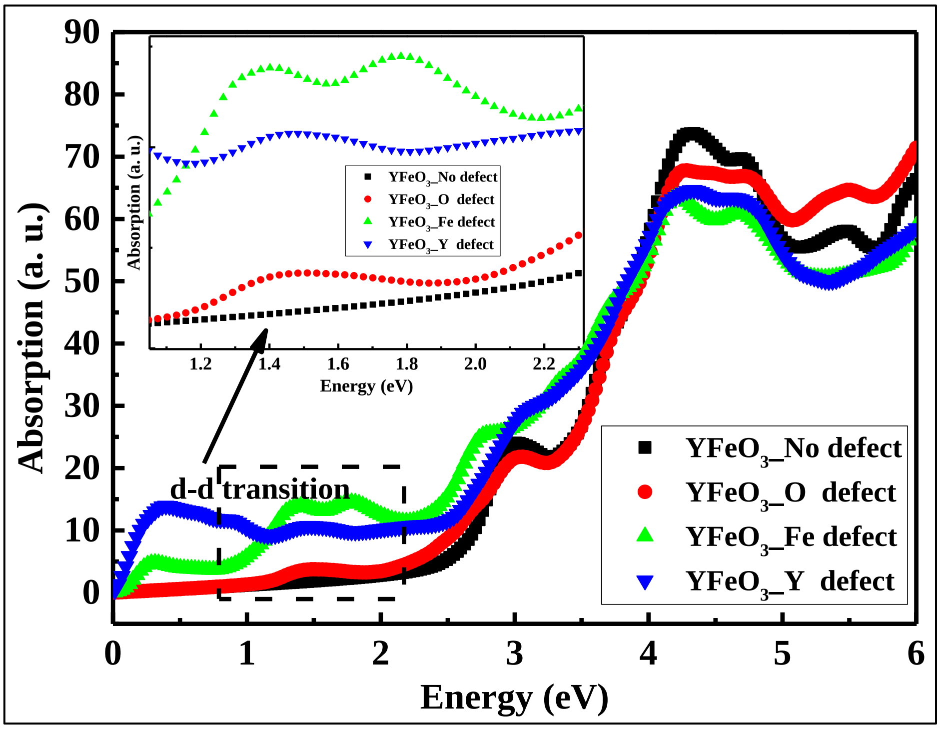

Figure 6.8: *Theoretically generated optical absorption spectra of* $YFeO_3$ *samples and considering its various defects.*

Furthermore, in order to understand the effect of non-stoichiometry on d-d transition, a first principle investigations have been carried out using ground-state density functional theory (DFT) as implemented in the WIEN2k package. This has been done to investigate the contribution of various defects of $YFeO_3$ samples to the so-called d-d transitions. Figure 6.8 shows the theoretically generated absorption spectra of $YFeO_3$ and its various defects. The energy range of the d-d transition of theoretically generated defect samples lies in the energy range of experimental spectra shown in Figure 6.6. Also, the theoretical absorption spectra of pure $YFeO_3$ sample matches well with the diffuse reflectance spectra of the hydrothermally synthesized $YFeO_3$ sample. Thus again, it very clear from the analysis of theoretically generated spectra together with experimental one that the defects or non-stoichiometry present in the samples are responsible for d-d transitions in d^5 systems.

In our earlier report [120] and also in chapter 5, we have shown that the defects at Y, Fe, and O site or self-doping leads to the mixed valency of Fe ions into the system, which forced d^5 systems to result into the mixed orbitals in terms of d^5/d^6 or d^5/d^4 depending on type of valency (i. e. $Fe^{2+}(d^6)$ or $Fe^{4+}(d^6)$). Thus; due to defect or excess, d^5 system actually not retains its pure d^5 orbital but results in mixed orbital states of d^5/d^6 or d^5/d^4. This may be the possible origin of observed d-d transition in d^5 systems.

6.5 Summary

Nearly stoichiometry and non-stoichiometry (self-doped) polycrystalline samples of $YFeO_3$ using various synthesis methods such as sol-gel synthesis, solid-state reaction and hydrothermal methods have been prepared. A detail investigation of d-d transition in $YFeO_3$ samples (considering a representative of d^5 system) have been done. The effect of annealing temperatures and various defects on the strength of d-d transitions in optical absorption spectra has been observed. The density functional theory investigation together with experimental optical absorption spectra reveal that the non-stoichiometry present in samples is one of the possible origins of d-d transitions in $YFeO_3$ and so does in $RFeO_3$ or d^5 systems. Another important conclusion may be drawn from this study that the hydrothermal synthesis or low-temperature sol-gel synthesis is the most suitable method for synthesizing nearly stoichiometry sample involving Fe complexes.

Chapter 7

Conclusion and Future Perspectives

This chapter includes the overall conclusions of this work which are listed below. Also, the possible future scopes of the work that can be carried out for further development in this field are discussed.

7.1 Conclusion

- In the present work, we studied a series of rare-earth orthoferrites $RFeO_3$ which is basically a perovskite-type oxide crystallizes in most common space group Pbnm. A detailed structural study of $RFeO_3$ was presented. The structural characteristics of eleven rare-earth orthoferrites (La, Pr, Sm, Nd, Eu, Tb, Dy, Ho, Y, Er, Yb) were investigated using synchrotron powder x-ray diffraction (SPXRD) and density functional theory. Structural distortions of $RFeO_3$ samples studied in terms of FeO_6 octahedra tilts, Fe-O/R-O bond length and Fe-O-Fe bond angles. Structural optimizations of $RFeO_3$ were performed using modern bond valance sum (SPuDS) and density functional theory (DFT) and found consistent with experimental results. These results confirm the validity of bond valence sum calculations to predict the structure of $RFeO_3$ type oxides.
- The electronic and optical properties of $RFeO_3$ samples investigated using diffuse reflectance spectroscopy. The optical bandgap of $RFeO_3$ samples was estimated and its correlation with structural parameters was established. The optical bandgap of $RFeO_3$ found independent of structural parameters such as lattice constants, Fe-O-Fe bond angles, and R-O bond length whereas, it seems to be controlled by Fe-O bond length i.e. the overlap between O-2p and Fe-3d orbitals in $RFeO_3$ samples. This

result was further confirmed using density functional theory.

- Further, the origin of unusual high net magnetic moments in antiferromagnetic $RFeO_3$ systems has been investigated considering various site defects using density functional theory. The study reveals that R and Fe site defects lead to the net magnetic moments in the $RFeO_3$ system. Bader charge analysis suggests the mixed valence states of Fe in Y, Fe and O defect systems responsible for Zener double exchange mechanism leads $RFeO_3$ systems to the ferromagnetism. These analyses provide us a basic understanding of the multiferroic coupling phenomena in $RFeO_3$ systems.
- In the last part of this work, a detailed experimental and theoretical investigations on the doubly forbidden d-d transitions in the d^5 system (considering $YFeO_3$ as a representative) have been done. The experimental optical absorption spectra and density functional theory investigation reveal that the non-stoichiometry present in samples is one of the possible origins of d-d transitions in $RFeO_3$ or d^5 systems.

7.2 Future Perspectives

- In this work, the structural, optical, and defect-induced magnetic and optical properties $RFeO_3$ have been studied. The influence of defect on magneto-dielectric and magneto-optical properties still remains to be examined. Field dependent experiment and field dependent density functional calculations on pure and self-doped samples may be useful in this regard.
- As a future scope, the fundamental works such as temperature dependent spin dynamics, neutron diffraction studies in order to understand the origin of magnetic phases exhibited by these materials should be explored.

- The process of spin reorientations under an external magnetic or electric field could be investigated in order to trigger a potential structural phase transition.
- It would be interesting to grow thin films of $RFeO_3$ systems to explore their structural, electronic, optical, and magnetic properties and compare to results of this work such as presence high net magnetic moment, nature of d-d transitions, and variation of bandgap as a function of rare-earth ionic radius and other structural parameters.

Appendix A

Design and Development of a Fully Automated Experimental Setup for In-situ Temperature Dependent Magneto-Dielectric Measurements

This section of the thesis provides the detail about the fabrication of a low cost and fully automated in-situ temperature dependent magneto-dielectric experimental setup has been reported. The setup has been fabricated to measure the effect of magnetic field on the dielectric constant of the material as a function of frequency and temperature. Measurements can be carried out over a temperature range from 120 K to 350 K, frequency range from 20 Hz to 10 MHz, and maximum magnetic field up to 2.2 Tesla. To monitor the measurement online a computer controlled Graphical User Interface (GUI) has also been developed based on QT C++ creator, an open source platform. The Magneto-dielectric effect has been demonstrated in $LaFe_{0.3}Ga_{0.7}O_3$ ***and*** $YFeO_3$ ***samples. The developed magneto-dielectric measurement setup will provide us a platform to understand the physics of dielectric constant of multiferroic materials under the influence of the magnetic field at different frequencies and temperatures[5].***

A.1 Introduction

The multiferroics are the most studied materials for last few decades and these materials have been attracting a great deal of attention owing to the

---

[5] ***Kamal Warshi et al.,*** Design and Development of a Low-Cost and fully Automated Experimental Setup for Temperature dependent Magneto-dielectric Measurements. **(Under Review)**

interesting electrical and magnetic properties they exhibit [9, 10, 210-213]. One of the most appealing aspects of multiferroics is their magneto-dielectric (MD) coupling i.e. effect of magnetic field on dielectric permittivity[214-217]. Recently, magneto-dielectric materials are explored as of very high research interest[212, 216, 218-223] due to their possible application in magnetic data storage and spintronic devices[224-227]. It may also be used to fabricate the micro-electronic random access memory (ME-RAM) that can enormously improve the storage efficiency and simultaneously it can reduce the time and power consumption required for the reading and writing operation of data[228]. Thus, it is very important to develop a cost-effective instrumentation technique that will facilitate the analysis of magneto-dielectric coupling in multiferroic materials as a function of both frequencies and temperatures.

In the present work, a low-temperature attachment to the already existing instruments such as Impedance Analyzer (Wayne Kerr 6500) and CTC 100 (cryogenic temperature controller from SRS) has been designed and fabricated to measure and analyze the dielectric properties of the materials under the in-situ influence of magnetic field and temperature. The instrumentations have been done considering the demand to control the temperature and explore the effect on the dielectric constant of materials under the influence of an applied magnetic field. The salient features of this setup are low-cost, automated, in-situ temperature dependent magneto-dielectric measurements and existing instruments in the lab.

In this report, an indirect method has been used to measure the dielectric constant of materials, that is to measure the dielectric constant we first measure the capacitance. We keep the sample in parallel plate geometry as shown in Figure A.1 and measure the capacitance (C) of a parallel plate capacitor filled with dielectric material, then we calculate dielectric constant of it using the equation below

$$\mathrm{C} = \varepsilon_0 \varepsilon' \frac{\mathrm{A}}{\mathrm{d}}, \tag{A.1}$$

where ε_0 is the dielectric permittivity of free space, ε' is the dielectric permittivity or dielectric constant of the material filled between the electrodes, d is the thickness of material, and A is the area of the contact plates. A solid cylindrical shaped sample coated with conducting silver paint on both the faces (work as electrodes) have been used for measurement.

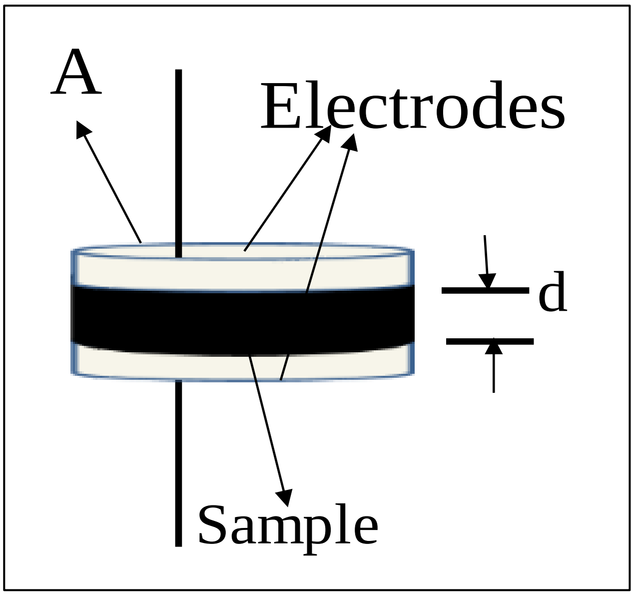

Figure A.1: *Parallel plate arrangement used to measure the dielectric constant of the material.*

In the magneto-dielectric measurement, we measure the dielectric constant of materials over a range of frequencies at a constant temperature under the influence of magnetic fields and we estimate the magneto-dielectric coupling percentage (MC %) by using the formula given by the equation below

$$MC\ (\%) = \frac{\varepsilon'(H\ T) - \varepsilon'(0\ T)}{\varepsilon'(0\ T)} \times 100, \qquad \text{(A.2)}$$

here $\varepsilon'(0\ T)$ and $\varepsilon'(H\ T)$ is the dielectric constants of material measured at 0 and at finite magnetic field 'H' tesla respectively.

A.2 Design and Fabrication of the Magneto-dielectric Probe

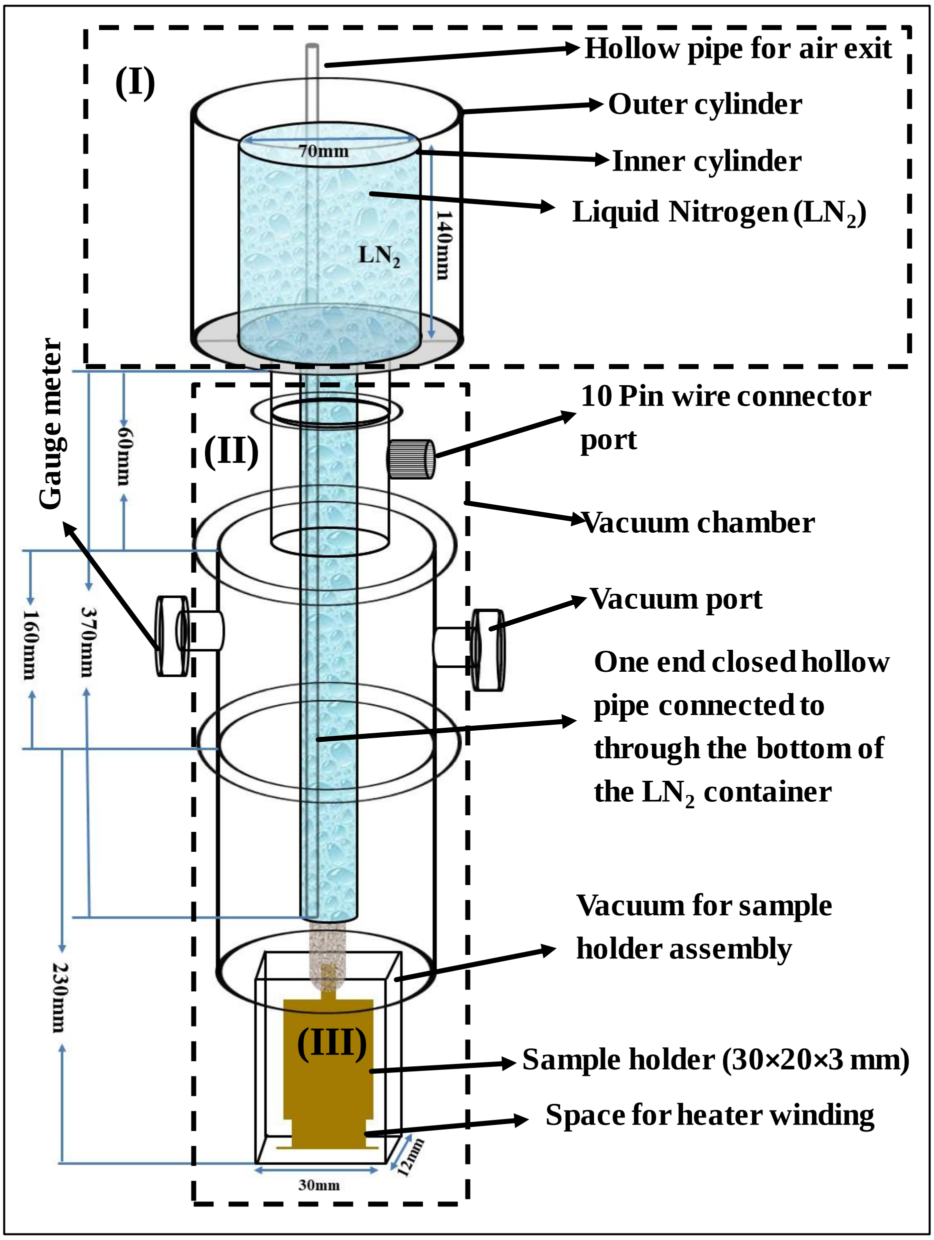

Figure A.2: *Schematic diagram showing the design of the experimental setup used for the magneto-dielectric measurement, describing the design of its various components.*

The schematic of the design used to fabricate the low-temperature magneto-dielectric probe with the dimension of each part of the setup has been shown in Figure A.2. The complete system has been designed in such a way that sample, sensor, and heater always remain in vacuum during the measurement and cooling of the sample will take place through the conduction of heat. The design of the magneto-dielectric probe has been done in three crucial sections. In the first section, a double-walled LN_2 container with a narrow pipe at the bottom connecting to the sample holder was designed in order to cool the sample, in Figure A.2 it is shown in the dashed rectangular box and marked as (I). The second (marked as (II) in Figure A.2) was devoted to designing the vacuum system; the dimension of the vacuum system has been kept in such a way that the distance between the poles of the electromagnet can be minimized in order to put the maximum magnetic field across the sample. The third section consists the design of the sample holder shown as (III) in Figure A.2; the sample holder has been designed in such a manner that the sample, temperature sensor, and heater could be placed very close to each other in order to minimize the temperature difference between sample and sensor. The photograph of developed magneto-dielectric setup in the laboratory shown in Figure A.3(a) and the description each component of the setup has been given below.

A.3 Experimental Setup and its Various Components

Impedance Analyzer

A high precision impedance analyzer 6500B model from Wayne Kerr shown in Figure A.3(b), was used to perform dielectric and magneto-dielectric measurements with an accuracy of ±0.05%. With the low-temperature attachment, we can measure dielectric constant and related material parameters such as dielectric loss, conductance, inductance, etc. from 20 Hz to 10 MHz.

Temperature Controller

CTC100 a cryogenic temperature controller from Stanford Research Systems (SRS) marked as Figure A.3(c), was used to control the temperature of the sample under investigation in the cryogenic environment. It has an accuracy of ±0.001K.

Electromagnet

An electromagnet is shown in Figure A.3(d), capable to deliver a maximum magnetic field of 2.2 Tesla at a pole separation of 1.2 cm to measure the magneto-dielectric coupling of the test sample. Regulated power supply up to 5A and a gauss meter are equipped to produce and measure the magnetic field during measurement, shown in Figure A.3(d) and (e) respectively. The gauss meter is equipped with a Hall probe, which is used as a sensor to measure the strength of the magnetic field of measurement. A Hall probe contains an indium compound semiconductor crystal mounted on an aluminum backing plate and encapsulated in the probe head.

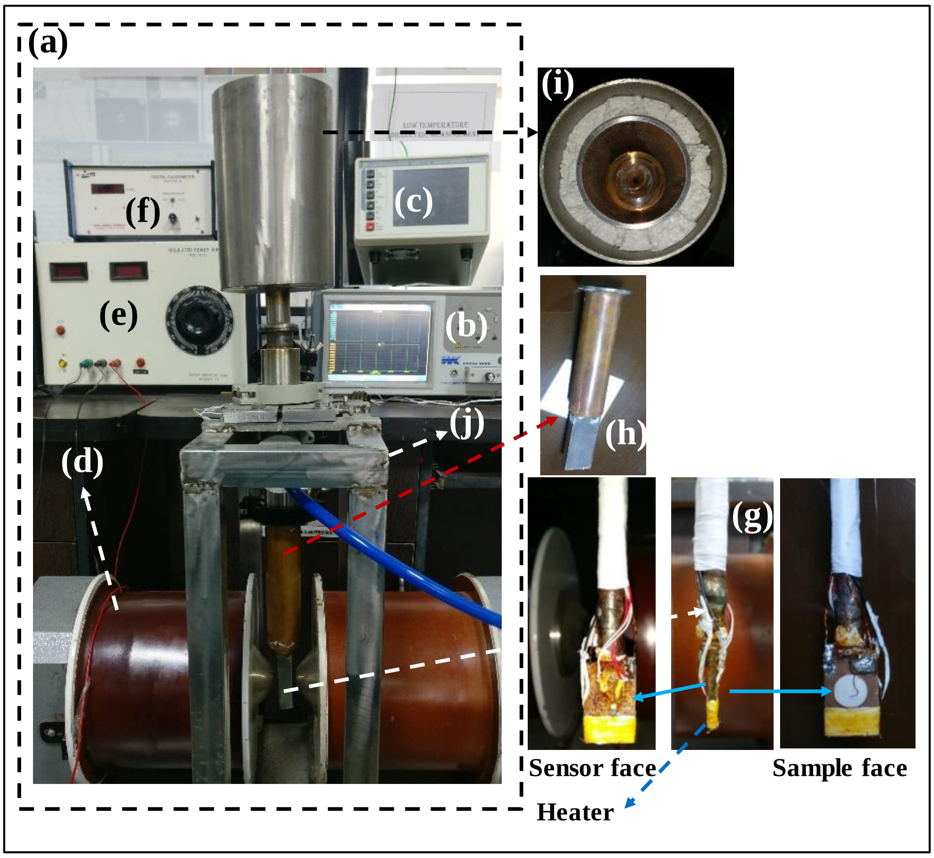

Figure A.3: *(a) Complete Experimental setup, (b) Impedance Analyzer, (c) Temperature Controller, (d) Electromagnet, (e) Power supply for electromagnet, (f) Gauss meter, (g) Sample, heater, and Temperature sensor assembly, (h) Vacuum Chamber designed for sample holder, (i) Top view of* LN_2 *container, (j)Stand designed to hold the complete setup.*

Sample holder: Sample, Heater, and Sensor Assembly

The sample holder design is shown in Figure A.3(g) which is basically an assembly of three major and important components of the entire setup, i. e. sample mounting space, temperature sensor, and heater. Each component has been placed very close to each other so that there is a minimum difference between sample and sensor temperatures. The sample holder design and developed in such a way that the maximum width of the whole assembly including the vacuum system around sample holder restricted within 1.2 cm in order to employ maximum magnetic field across the sample. A rectangular slab of Copper of width 3 mm has been chosen to fabricate the sample holder, as we know Copper has very high thermal conductivity. It has been designed in such a way that a sample with maximum thickness 3 mm and with diameter 10-13 mm on one side and on the other side just opposite to the sample a pt-100 resistance temperature sensor can be mount. An inductive less heater with resistance 45 Ohm was wounded at the lower portion of the sample holder in such a way that the rate of heat transfer will be equal for the sample as well as for the sensor. The sample holder assembly was kept inside stainless steel (SS) hollow rectangular box as shown in Figure A.3(h) to create the vacuum around the sample. The sample is mounted by using silver paint on one side of the rectangular Cu slab (See Figure A.3(g)). A cylindrical hollow rod mounted at the bottom of the double cylindrical wall container made of stainless steel (SS) connecting directly to the sample holder was used to provide the pathway for the cooling agent (liquid N_2 for the present study) to the sample holder. The top cross-sectional view of double wall LN_2 container shown in Figure A.3(i), the gap between the walls used to fill with thermally insulating materials to avoid the loss of LN_2. The system could achieve a measurement temperature range from 120 K to 350 K with a vacuum of 10^{-3} mbar with a turbo vacuum pump. The length of the sample holder including vacuum and cooling systems, have been arranged in such a way that when it is placed on the stand (see Figure A.3(j)), the sample automatically reaches exactly in between the center of two poles of the electromagnet as shown in Figure A.3(a).

A.4 Automation: Graphical User Interface

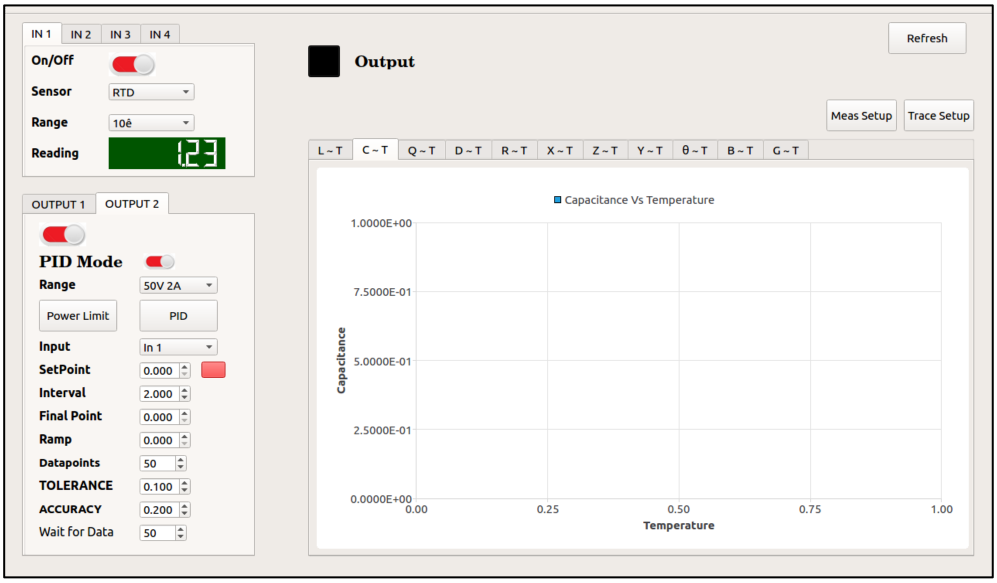

On/Off
Sensor RTD
Range 10ê
Reading 1.23

PID Mode
Range 50V 2A
Input In 1
SetPoint 0.000
Interval 2.000
Final Point 0.000
Ramp 0.000
Datapoints 50
TOLERANCE 0.100
ACCURACY 0.200
Wait for Data 50

Figure A.4: *Photo of User Interface for magneto-dielectric measurements developed on QT C++ creator.*

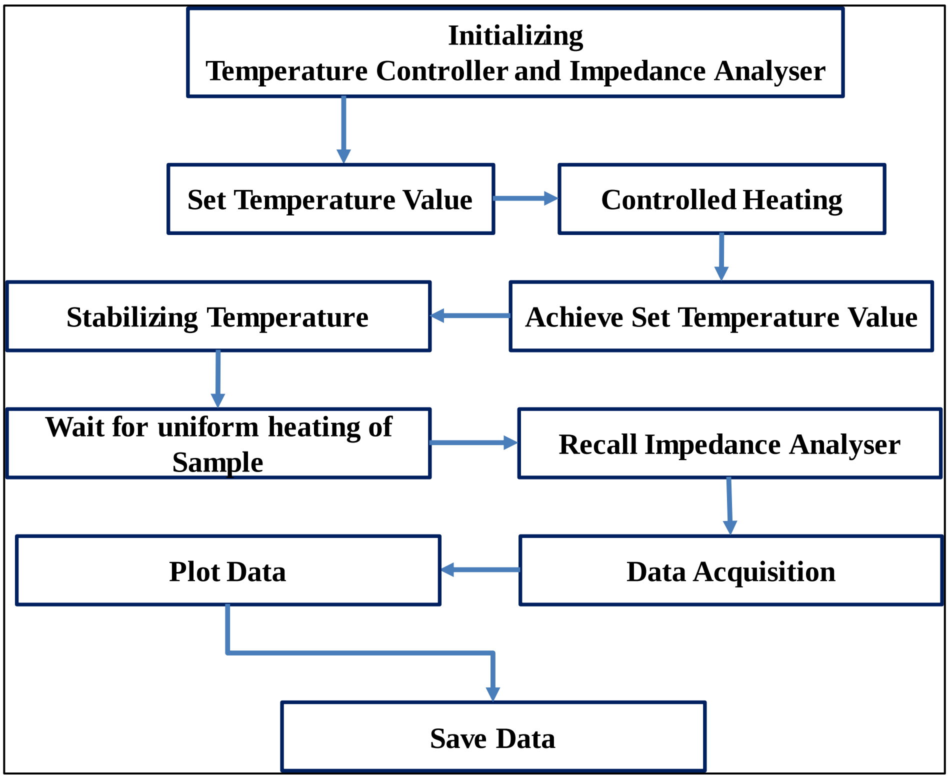

Figure A.5: *Flow diagram of logic used during programming*

A fully automated graphical user interface (GUI) has been developed in open source QT C++ creator to control the measurement online. The photograph of developed GUI has been shown in Figure A.4. The automation of the experimental setup has been achieved for the simultaneous measurement of dielectric constant and other related parameters such as dielectric loss, inductance, conductance, resistance, etc. as a function of temperature as well as of frequency at a particular magnetic field. The working of the GUI depicted in the flowchart as shown in Figure A.5.

A.5 Results and Discussion

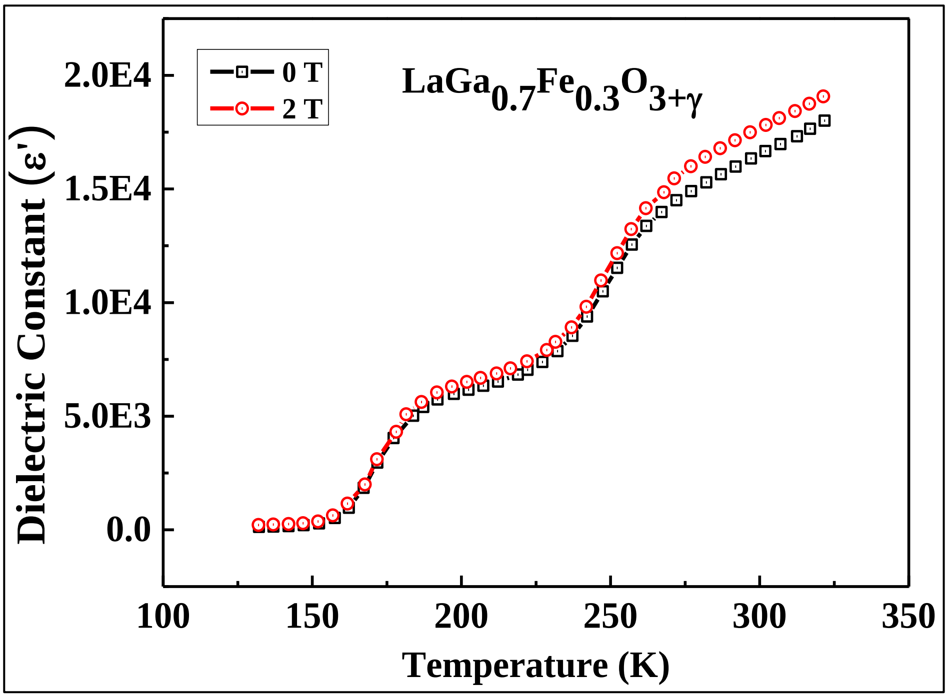

Figure A.6: *The observed magneto-dielectric effect at 100 Hz for* $LaGa_{0.7}Fe_{0.3}O_{3+\delta}$ *sample.*

The reproducibility of the data with a certain level of accuracy is very important in order to verify the performance of any instrument. Thus, the developed magneto-dielectric measurement setup was tested to reproduce the results of several materials. The magneto-dielectric measurements were done for $LaGa_{0.7}Fe_{0.3}O_{3+\delta}$ sample and the results of these measurements have been successfully reported elsewhere[191]. Figure A.6 shows the magneto-dielectric coupling in $LaGa_{0.7}Fe_{0.3}O_{3+\delta}$

due to non-stoichiometry present in the sample arises due to access of Oxygen. The formal oxidation states of Fe ions in $LaGa_{0.7}Fe_{0.3}O_3$ is 3+ but due to high processing temperature, the oxidation state changes to 4+.

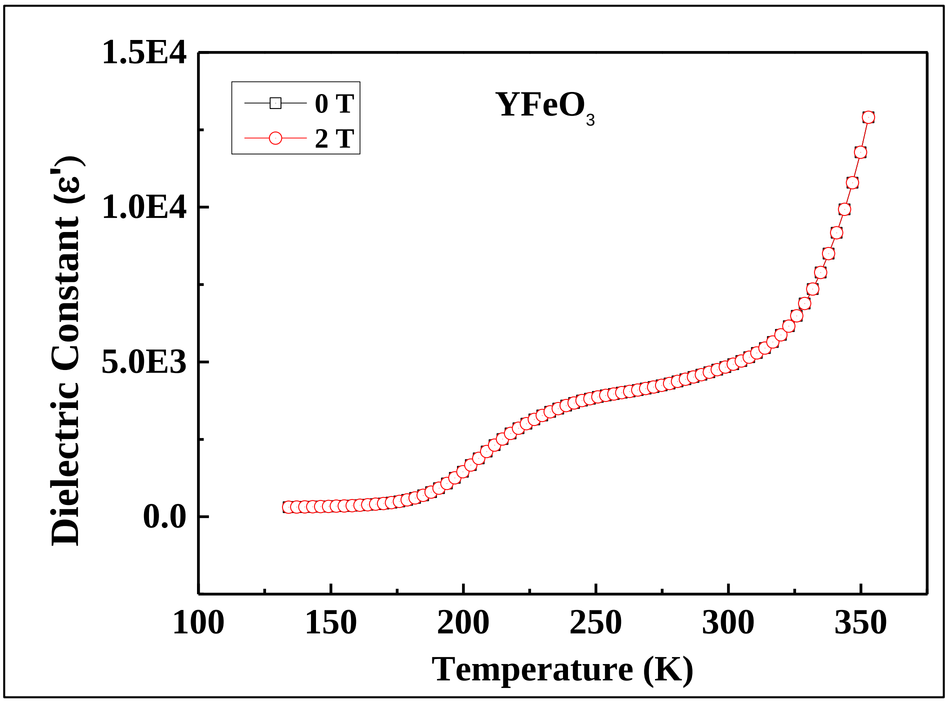

Figure A.7: *The magneto-dielectric effect observed at 100 Hz for* $YFeO_3$ *sample synthesized with low-temperature sol-gel synthesis method.*

In order to validate the accuracy of the developed experimental setup, we have repeated the experiment on sol-gel synthesized $YFeO_3$ sample processed at low temperature for example at 800 °C. The idea is to synthesize the sample as possible as stoichiometric with respect to Oxygen access or defect. The magneto-dielectric measurements results have been shown in Figure A.7 and as expected, we find that data acquired at 0Tesla and at 2Tesla tracing exactly each other.

A.6 Summary

A cost-effective and fully automated temperature dependent experimental setup for magneto-dielectric measurement has been designed and developed. The setup covers a large range of temperatures from 120 to 350 K, frequency range from 20 Hz to 10 MHz, and magnetic field up to 2.2 Tesla. The setup has been validated on Ga doped $LaFeO_3$ and $YFeO_3$ samples. This experimental setup might be a significant tool to investigate the properties of multiferroic materials as this provides an opportunity to study the influence of magnetic field on the dielectric constant of materials as a function of temperature as well as the frequency in a very simple way.

References

1. Bordkin, J. *Why Facebook thinks Blu-ray dics are perfect for the center ?* 2014; Available from: http://arstechnica.com/information-technology/2014/01/why-facebook-thinks-blu-ray-discs-are-perfect-for-the-data-center.
2. Seagate. *The Demand for Storage Devices in a Connected World of Data*. 2016; Available from: https://www.seagate.com/in/en/tech-insights/demand-for-storage-devices-in-connected-world-master-ti/.
3. Peter Hormann, L.C., *Data Storage Energy Efficiency in the Zettabyte Era.* Journal of Telecommunications and the Digital Economy, 2014. **2**(3): p. 51.
4. TechTarget. *Companies try green storage strategies to reduce power consumption.* 2017; Available from: https://searchstorage.techtarget.com/feature/Companies-try-green-storage-strategies-to-reduce-power-consumption.
5. Kovalenko, M.V., L. Protesescu, and M.I. Bodnarchuk, *Properties and potential optoelectronic applications of lead halide perovskite nanocrystals.* Science, 2017. **358**(6364): p. 745.
6. Kubicek, M., A.H. Bork, and J.L.M. Rupp, *Perovskite oxides – a review on a versatile material class for solar-to-fuel conversion processes.* Journal of Materials Chemistry A, 2017. **5**(24): p. 11983-12000.
7. Dogan, F., et al., *Focus on properties and applications of perovskites.* Science and Technology of Advanced Materials, 2015. **16**(2): p. 020301.
8. Labhasetwar, N., et al., *Perovskite-type catalytic materials for environmental applications.* Science and Technology of Advanced Materials, 2015. **16**(3): p. 036002.
9. Kimura, T., *Magnetocapacitance effect in multiferroic BiMnO3 (2003) Phys.* Rev. B. **67**: p. 180401.
10. Kimura, T., et al., *Magnetic control of ferroelectric polarization.* Nature, 2003. **426**: p. 55.

11. Markovich, V., et al., *Magnetic, electric and electron magnetic resonance properties of orthorhombic self-doped La $_{1-x}$ MnO$_3$ single crystals.* Journal of Physics: Condensed Matter, 2003. **15**(23): p. 3985.
12. Mostovoy, M., *Ferroelectricity in Spiral Magnets.* Physical Review Letters, 2006. **96**(6): p. 067601.
13. Han, H., et al., *Switchable ferroelectric photovoltaic effects in epitaxial h-RFeO3 thin films.* Nanoscale, 2018. **10**(27): p. 13261-13269.
14. Han, H., et al., *Enhanced Switchable Ferroelectric Photovoltaic Effects in Hexagonal Ferrite Thin Films via Strain Engineering.* ACS Applied Materials & Interfaces, 2018. **10**(2): p. 1846-1853.
15. Ruddlesden, S.N. and P. Popper, *The compound Sr3Ti2O7 and its structure.* Acta Crystallographica, 1958. **11**(1): p. 54-55.
16. Chakhmouradian, A.R. and P.M. Woodward, *Celebrating 175 years of perovskite research: a tribute to Roger H. Mitchell.* Physics and Chemistry of Minerals, 2014. **41**(6): p. 387-391.
17. Mitchell, R.H., *Perovskites : modern and ancient*. 2002, Thunder Bay, Ont.: Almaz Press.
18. Goldschmidt, V.M., *Die Gesetze der Krystallochemie.* Naturwissenschaften, 1926. **14**(21): p. 477-485.
19. Li, Z., et al., *Stabilizing Perovskite Structures by Tuning Tolerance Factor: Formation of Formamidinium and Cesium Lead Iodide Solid-State Alloys.* Chemistry of Materials, 2016. **28**(1): p. 284-292.
20. Travis, W., et al., *On the application of the tolerance factor to inorganic and hybrid halide perovskites: a revised system.* Chemical Science, 2016. **7**(7): p. 4548-4556.
21. Geller, S., *Crystal Structure of Gadolinium Orthoferrite, GdFeO3.* The Journal of Chemical Physics, 1956. **24**(6): p. 1236-1239.
22. Dixon, C.A.L., et al., *Thermal evolution of the crystal structure of the orthorhombic perovskite LaFeO3.* Journal of Solid State Chemistry, 2015. **230**: p. 337-342.

23. Katayama, T., et al., *Ferrimagnetism and Ferroelectricity in Cr-Substituted GaFeO3 Epitaxial Films.* Chemistry of Materials, 2018. **30**(4): p. 1436-1441.
24. Rivero, P., V. Meunier, and W. Shelton, *Electronic, structural, and magnetic properties of ${\mathrm{LaMnO}}_{3}$ phase transition at high temperature.* Physical Review B, 2016. **93**(2): p. 024111.
25. Hirai, K., et al., *Strain-induced significant increase in metal-insulator transition temperature in oxygen-deficient Fe oxide epitaxial thin films.* Scientific Reports, 2015. **5**: p. 7894.
26. Sclauzero, G., K. Dymkowski, and C. Ederer, *Tuning the metal-insulator transition in ${d}^{1}$ and ${d}^{2}$ perovskites by epitaxial strain: A first-principles-based study.* Physical Review B, 2016. **94**(24): p. 245109.
27. Burton, J.D. and E.Y. Tsymbal, *Tunneling anisotropic magnetoresistance in a magnetic tunnel junction with half-metallic electrodes.* Physical Review B, 2016. **93**(2): p. 024419.
28. Song, Y.-Q., et al., *Multiferroic properties in terbium orthoferrite.* Chinese Physics B, 2014. **23**(7): p. 077505.
29. Yokota, H., et al., *Ferroelectricity and weak ferromagnetism of hexagonal $ErFeO_3$ thin films.* Physical Review B, 2015. **92**(5): p. 054101.
30. Hur, N., et al., *Electric polarization reversal and memory in a multiferroic material induced by magnetic fields.* Nature, 2004. **429**: p. 392.
31. Nair, V.G., et al., *Magnetic structure and magnetodielectric effect of YFe0.5Cr0.5O3.* Journal of Applied Physics, 2013. **113**(21): p. 213907.
32. Pavlov, V.V., et al., *Optical properties and electronic structure of multiferroic hexagonal orthoferrites RFeO3 (R = Ho, Er, Lu).* Journal of Applied Physics, 2012. **111**(5): p. 056105.
33. Herklotz, A., et al., *Controlling Octahedral Rotations in a Perovskite via Strain Doping.* Scientific Reports, 2016. **6**: p. 26491.

34. Vailionis, A., et al., *Misfit strain accommodation in epitaxial $AB{\mathrm{O}}_{3}$ perovskites: Lattice rotations and lattice modulations.* Physical Review B, 2011. **83**(6): p. 064101.
35. Mulder, A.T., et al., *Turning ABO3 Antiferroelectrics into Ferroelectrics: Design Rules for Practical Rotation-Driven Ferroelectricity in Double Perovskites and A3B2O7 Ruddlesden-Popper Compounds.* Advanced Functional Materials, 2013. **23**(38): p. 4810-4820.
36. Maryško, M., et al., *Magnetic susceptibility of multiferroics and chemical ordering.* AIP Advances, 2017. **7**(5): p. 056409.
37. Kumar, M.V., et al., *Microstructure and Magnetic Properties of Metastable RFeO3 (R: Rare-earth element) Formed from Undercooled Melt.* Journal of the American Ceramic Society, 2013. **96**(3): p. 995-1002.
38. Xu, X. and W. Wang, *Multiferroic hexagonal ferrites (h-RFeO3, R = Y, Dy-Lu): a brief experimental review.* Modern Physics Letters B, 2014. **28**(21): p. 1430008.
39. Kang, J., et al., *Spin-reorientation magnetic transitions in Mn-doped SmFeO3.* IUCrJ, 2017. **4**(5): p. 598-603.
40. Zhao, H.J., et al., *Improper electric polarization in simple perovskite oxides with two magnetic sublattices.* Nature Communications, 2017. **8**: p. 14025.
41. Mandal, P., et al., *Spin-Reorientation, Ferroelectricity, and Magnetodielectric Effect in $YFe_{1-x}MnxO_3$ (00.1 $\leq x \leq$ 0.40).* Physical Review Letters, 2011. **107**(13): p. 137202.
42. Shang, M., et al., *The multiferroic perovskite $YFeO_3$.* Applied Physics Letters, 2013. **102**(6): p. 062903.
43. Singh, A., et al., *Optimal multiferroic properties and enhanced magnetoelectric coupling in $SmFeO_3$–$PbTiO_3$ solid solutions.* Journal of Applied Physics, 2010. **107**(8): p. 084106.
44. Schmool, D.S., et al., *Magnetic and magneto-optic properties of orthoferrite thin films grown by pulsed-laser deposition.* Journal of Applied Physics, 1999. **86**(10): p. 5712-5717.

45. Singh, N., J. Yull Rhee, and S. Auluck, *Electronic and Magneto-Optical Properties of Rare-Earth Orthoferrites RFeO3 (R = Y, Sm, Eu, Gd and Lu)*. Vol. 53. 2008.
46. Kahn, F.J., P.S. Pershan, and J.P. Remeika, *Ultraviolet Magneto-Optical Properties of Single-Crystal Orthoferrites, Garnets, and Other Ferric Oxide Compounds*. Physical Review, 1969. **186**(3): p. 891-918.
47. Dzyaloshinsky, I., *A thermodynamic theory of "weak" ferromagnetism of antiferromagnetics*. Journal of Physics and Chemistry of Solids, 1958. **4**(4): p. 241-255.
48. Moriya, T., *Anisotropic Superexchange Interaction and Weak Ferromagnetism*. Physical Review, 1960. **120**(1): p. 91-98.
49. Pomiro, F., et al., *Spin reorientation, magnetization reversal, and negative thermal expansion observed in* $RFe_{0.5}Cr_{0.5}O_3$ *perovskites (R=Lu,Yb,Tm)*. Physical Review B, 2016. **94**(13): p. 134402.
50. Scola, J., et al., *Spin reorientation induced by a very high magnetic field in domain-structured* $YFeO_3$ *films: Emergence of perpendicular anisotropy*. Physical Review B, 2010. **81**(17): p. 174409.
51. Song, G., et al., *Spin reorientation transition process in single crystal* $NdFeO_3$. Solid State Communications, 2015. **211**: p. 47-51.
52. Yuan, S., et al., *Magnetic properties of* $NdFeO_3$ *single crystal in the spin reorientation region*. Journal of Applied Physics, 2011. **109**(7): p. 07E141.
53. Jiang, J., et al., *Dynamical spin reorientation transition in NdFeO3 single crystal observed with polarized terahertz time domain spectroscopy*. Applied Physics Letters, 2013. **103**(6): p. 062403.
54. Zhou, R., et al., *Terahertz magnetic field induced coherent spin precession in* $YFeO_3$. Applied Physics Letters, 2012. **100**(6): p. 061102.
55. Cao, S., et al., *Temperature induced Spin Switching in* $SmFeO_3$ *Single Crystal*. Scientific Reports, 2014. **4**: p. 5960.
56. Tokunaga, Y., et al., *Magnetic-Field-Induced Ferroelectric State in* $DyFeO_3$. Physical Review Letters, 2008. **101**(9): p. 097205.

57. Mochizuki, M. and N. Furukawa, *Theory of Magnetic Switching of Ferroelectricity in Spiral Magnets.* Physical Review Letters, 2010. **105**(18): p. 187601.
58. Marezio, M. and P.D. Dernier, *The bond lengths in* $LaFeO_3$. Materials Research Bulletin, 1971. **6**(1): p. 23-29.
59. Marezio, M., J.P. Remeika, and P.D. Dernier, *The crystal chemistry of the rare earth orthoferrites.* Acta Crystallographica Section B, 1970. **26**(12): p. 2008-2022.
60. Zhou, Z., et al., *Hydrothermal synthesis and magnetic properties of multiferroic rare-earth orthoferrites.* Journal of Alloys and Compounds, 2014. **583**: p. 21-31.
61. Weber, M.C., et al., *Raman spectroscopy of rare-earth orthoferrites* $RFeO_3$ *(R=La, Sm, Eu, Gd, Tb, Dy).* Physical Review B, 2016. **94**(21): p. 214103.
62. Shapiro, S.M., J.D. Axe, and J.P. Remeika, *Neutron-scattering studies of spin waves in rare-earth orthoferrites.* Physical Review B, 1974. **10**(5): p. 2014-2021.
63. Hahn, S.E., et al., *Inelastic neutron scattering studies of ${\text{YFeO}}_{3}$.* Physical Review B, 2014. **89**(1): p. 014420.
64. Mandal, P., et al., *Spin reorientation and magnetization reversal in the perovskite oxides, YFe1−xMnxO3 (0≤x≤0.45): A neutron diffraction study.* Journal of Solid State Chemistry, 2013. **197**: p. 408-413.
65. Bartolomé, J., et al., *Single-crystal neutron diffraction study of Nd magnetic ordering in ${\mathrm{NdFeO}}_{3}$ at low temperature.* Physical Review B, 1997. **55**(17): p. 11432-11441.
66. Sławiński, W., et al., *Spin reorientation and structural changes in NdFeO 3.* Journal of Physics: Condensed Matter, 2005. **17**(29): p. 4605.
67. Akbashev, A.R., et al., *Weak ferromagnetism in hexagonal orthoferrites RFeO3 (R = Lu, Er-Tb).* Applied Physics Letters, 2011. **99**(12): p. 122502.

68. Zhu, W., et al., *Anisotropy and extremely high coercivity in weak ferromagnetic LuFeO3.* Applied Physics Letters, 2012. **100**(5): p. 052407.
69. Yokota, H., et al., *Ferroelectricity and weak ferromagnetism of hexagonal $\mathrm{ErFe}{\mathrm{O}}_{3}$ thin films.* Physical Review B, 2015. **92**(5): p. 054101.
70. Keffer, F., *Moriya Interaction and the Problem of the Spin Arrangements in $\ensuremath{\beta}\mathrm{MnS}$.* Physical Review, 1962. **126**(3): p. 896-900.
71. Sergienko, I.A. and E. Dagotto, *Role of the Dzyaloshinskii-Moriya interaction in multiferroic perovskites.* Physical Review B, 2006. **73**(9): p. 094434.
72. Cheong, S.-W. and M. Mostovoy, *Multiferroics: a magnetic twist for ferroelectricity.* Nature Materials, 2007. **6**: p. 13.
73. Siwach, P.K., H.K. Singh, and O.N. Srivastava, *Low field magnetotransport in manganites.* Journal of Physics: Condensed Matter, 2008. **20**(27): p. 273201.
74. Kumaresavanji, M., et al., *Reinforcement of double-exchange ferromagnetic coupling by Ru in La1.24Sr1.76Mn2-yRuyO7 manganite system.* Materials Research Bulletin, 2014. **51**: p. 92-96.
75. Zener, C., *Interaction between the d-Shells in the Transition Metals. II. Ferromagnetic Compounds of Manganese with Perovskite Structure.* Physical Review, 1951. **82**(3): p. 403-405.
76. Zener, C., *Interaction Between the d Shells in the Transition Metals.* Physical Review, 1951. **81**(3): p. 440-444.
77. Gleitzer, C. and J.B. Goodenough. *Mixed-valence iron oxides*. in *Cation Ordering and Electron Transfer*. 1985. Berlin, Heidelberg: Springer Berlin Heidelberg.
78. Sultan, K., M. Ikram, and K. Asokan, *Structural, optical and dielectric study of Mn doped PrFeO3 ceramics.* Vacuum, 2014. **99**: p. 251-258.
79. Chmaissem, O., et al., *Relationship between structural parameters and the N'eel temperature in* $Sr_{1-x}Ca_xMnO_3$ *(0<~x<~1) and* $Sr_{1-y}Ba_yMnO_3$ *(y<~0.2).* Physical Review B, 2001. **64**(13): p. 134412.

80. Hong Jian, Z., et al., *Creating multiferroics with large tunable electrical polarization from paraelectric rare-earth orthoferrites.* Journal of Physics: Condensed Matter, 2014. **26**(47): p. 472201.
81. Chowdhury, U., et al., *Room temperature multiferroicity in orthorhombic LuFeO3.* Applied Physics Letters, 2014. **105**(5): p. 052911.
82. Ma, Y., X.M. Chen, and Y.Q. Lin, *Relaxorlike dielectric behavior and weak ferromagnetism in YFeO3 ceramics.* Journal of Applied Physics, 2008. **103**(12): p. 124111.
83. Stoeffler, D. and Z. Chaker, *First principles study of the electronic structure and magnetic properties of* $YFeO_3$ *oxide.* Journal of Magnetism and Magnetic Materials, 2017. **442**: p. 255-264.
84. Coutinho, P.V., F. Cunha, and P. Barrozo, *Structural, vibrational and magnetic properties of the orthoferrites LaFeO3 and YFeO3: A comparative study.* Solid State Communications, 2017. **252**: p. 59-63.
85. Lima, E., et al., *Numerical simulation of magnetic interactions in polycrystalline YFeO3.* Journal of Magnetism and Magnetic Materials, 2008. **320**(5): p. 622-629.
86. Maiti, R., S. Basu, and D. Chakravorty, *Synthesis of nanocrystalline YFeO3 and its magnetic properties.* Journal of Magnetism and Magnetic Materials, 2009. **321**(19): p. 3274-3277.
87. Mathur, S., et al., *Molecule Derived Synthesis of Nanocrystalline YFeO3 and Investigations on Its Weak Ferromagnetic Behavior.* Chemistry of Materials, 2004. **16**(10): p. 1906-1913.
88. Kimizuka, N. and T. Katsura, *Standard free energy of formation of* $YFeO_3$*,* $Y3Fe_5O_{12}$*, and a new compound* YFe_2O_4 *in the* $Fe\text{-}Fe_2O_3\text{-}Y_2O_3$ *system at 1200°C.* Journal of Solid State Chemistry, 1975. **13**(3): p. 176-181.
89. Warshi, M.K., et al., *Structural, optical and electronic properties of* $RFeO_3$*.* Ceramics International, 2018.
90. Moskvin, A.S., et al., *Interplay of p-d and d-d charge transfer transitions in rare-earth perovskite manganites.* Physical Review B, 2010. **82**(3): p. 035106.

91. Mark, D.S., et al., *Band structure and optical transitions in $LaFeO_3$: theory and experiment.* Journal of Physics: Condensed Matter, 2014. **26**(50): p. 505502.
92. Rao, B.G., D. Mukherjee, and B.M. Reddy, *Chapter 1 - Novel approaches for preparation of nanoparticles,* in *Nanostructures for Novel Therapy,* D. Ficai and A.M. Grumezescu, Editors. 2017, Elsevier. p. 1-36.
93. Danks, A.E., S.R. Hall, and Z. Schnepp, *The evolution of 'sol-gel' chemistry as a technique for materials synthesis.* Materials Horizons, 2016. **3**(2): p. 91-112.
94. Feng, S.H. and G.H. Li, *Chapter 4 - Hydrothermal and Solvothermal Syntheses,* in *Modern Inorganic Synthetic Chemistry (Second Edition)*, R. Xu and Y. Xu, Editors. 2017, Elsevier: Amsterdam. p. 73-104.
95. Cullity, B.D. and S.R. Stock, *Elements of X-ray diffraction*. 3rd ed. ed. 2001: Upper Saddle River.
96. Kittel, C., *Introduction to Solid State Physics*, ed. 8. 2004: Wiley.
97. Ying, S., et al., *Negative Thermal Expansion and Correlated Magnetic and Electrical Properties of Si-Doped Mn3GaN Compounds.* Journal of the American Ceramic Society, 2010. **93**(3): p. 650-653.
98. Zu, L., et al., *A first-order antiferromagnetic-paramagnetic transition induced by structural transition in GeNCr3.* Applied Physics Letters, 2016. **108**(3): p. 031906.
99. Kortum, G., *Reflectance spectroscopy. Principles, methods, applications*. 1969: Berlin: J. Springer, 1969.
100. Lambert, J.H. and D.L. DiLaura, *Photometry: Or, on the Measure and Gradations of Light, Colors, and Shade*. 2001: IESNA Publications Department.
101. Fuller, M.P. and P.R. Griffiths, *Diffuse reflectance measurements by infrared Fourier transform spectrometry.* Analytical Chemistry, 1978. **50**(13): p. 1906-1910.
102. Wetzel, D.L., *Near-infrared reflectance analysis.* Analytical Chemistry, 1983. **55**(12): p. 1165A-1176A.

103. Alexander, K. and H. Ian, *Some analytical approximations to radiative transfer theory and their application for the analysis of reflectance data.* Journal of Optics A: Pure and Applied Optics, 2008. **10**(3): p. 035001.
104. Burger, T., et al., *Diffuse Reflectance and Transmittance Spectroscopy for the Quantitative Determination of Scattering and Absorption Coefficients in Quantitative Powder Analysis.* Applied Spectroscopy, 1997. **51**(9): p. 1323-1329.
105. Zhang, Q., Z. Zhang, and Z. Zhou, *Probe into the reflection from GaP nanoparticles via different solutions of radiative transfer equation.* Applied Physics B, 2008. **93**(2): p. 589.
106. Mishchenko, M.I., et al., *Bidirectional reflectance of flat, optically thick particulate layers: an efficient radiative transfer solution and applications to snow and soil surfaces.* Journal of Quantitative Spectroscopy and Radiative Transfer, 1999. **63**(2): p. 409-432.
107. Kubelka, P., *New Contributions to the Optics of Intensely Light-Scattering Materials. Part I.* Journal of the Optical Society of America, 1948. **38**(5): p. 448-457.
108. Yang, L. and B. Kruse, *Revised Kubelka–Munk theory. I. Theory and application.* Journal of the Optical Society of America A, 2004. **21**(10): p. 1933-1941.
109. Myrick, M.L., et al., *The Kubelka-Munk Diffuse Reflectance Formula Revisited.* Applied Spectroscopy Reviews, 2011. **46**(2): p. 140-165.
110. De Groot, F. and A. Kotani, *Core level spectroscopy of solids. CRC Press, Boca Raton*. 2008.
111. *Introduction*, in *Introduction to XAFS: A Practical Guide to X-ray Absorption Fine Structure Spectroscopy*, G. Bunker, Editor. 2010, Cambridge University Press: Cambridge. p. 1-7.
112. de Groot, F., *High-Resolution X-ray Emission and X-ray Absorption Spectroscopy.* Chemical Reviews, 2001. **101**(6): p. 1779-1808.

113. Sagdeo, A., et al., *Large dielectric permittivity and possible correlation between magnetic and dielectric properties in bulk BaFeO3−δ.* Applied Physics Letters, 2014. **105**(4): p. 042906.

114. Westre, T.E., et al., *A Multiplet Analysis of Fe K-Edge 1s → 3d Pre-Edge Features of Iron Complexes.* Journal of the American Chemical Society, 1997. **119**(27): p. 6297-6314.

115. de Groot, F.M.F., et al., *Oxygen 1s x-ray-absorption edges of transition-metal oxides.* Physical Review B, 1989. **40**(8): p. 5715-5723.

116. Hohenberg, P. and W. Kohn, *Inhomogeneous Electron Gas.* Physical Review, 1964. **136**(3B): p. B864-B871.

117. Kohn, W., *Nobel Lecture: Electronic structure of matter---wave functions and density functionals.* Reviews of Modern Physics, 1999. **71**(5): p. 1253-1266.

118. Kohn, W. and L.J. Sham, *Self-Consistent Equations Including Exchange and Correlation Effects.* Physical Review, 1965. **140**(4A): p. A1133-A1138.

119. Tavares, S.R., et al., *DFT calculations for structural prediction and applications of intercalated lamellar compounds.* Dalton Transactions, 2018. **47**(9): p. 2852-2866.

120. Warshi, M.K., et al., *Possible origin of ferromagnetism in antiferromagnetic orthorhombic-YFeO3: A first-principles study.* Ceramics International, 2018. **44**(12): p. 13507-13512.

121. Sham, L.J. and W. Kohn, *One-Particle Properties of an Inhomogeneous Interacting Electron Gas.* Physical Review, 1966. **145**(2): p. 561-567.

122. K. S. Blaha, P., et al., *WIEN2k: An Augmented Plane Wave plus Local Orbitals Program for Calculating Crystal Properties*. 2001.

123. Perdew, J.P., K. Burke, and M. Ernzerhof, *Generalized Gradient Approximation Made Simple.* Physical Review Letters, 1996. **77**(18): p. 3865-3868.

124. Anisimov, V.I., et al., *Density-functional theory and NiO photoemission spectra.* Physical Review B, 1993. **48**(23): p. 16929-16934.

125. Lany, S. and A. Zunger, *Assessment of correction methods for the band-gap problem and for finite-size effects in supercell defect calculations: Case studies for ZnO and GaAs.* Physical Review B, 2008. **78**(23): p. 235104.

126. Walle, C.G.V.d. and J. Neugebauer, *First-principles calculations for defects and impurities: Applications to III-nitrides.* Journal of Applied Physics, 2004. **95**(8): p. 3851-3879.

127. Li, Y., W.G. Schmidt, and S. Sanna, *Defect complexes in congruent $LiNbO_3$ and their optical signatures.* Physical Review B, 2015. **91**(17): p. 174106.

128. Otero-de-la-Roza, A., et al., *Critic: a new program for the topological analysis of solid-state electron densities.* Computer Physics Communications, 2009. **180**(1): p. 157-166.

129. Otero-de-la-Roza, A., E.R. Johnson, and V. Luaña, *Critic2: A program for real-space analysis of quantum chemical interactions in solids.* Computer Physics Communications, 2014. **185**(3): p. 1007-1018.

130. Otero-de-la-Roza, A. and V. Luaña, *A fast and accurate algorithm for QTAIM integration in solids.* Journal of Computational Chemistry, 2011. **32**(2): p. 291-305.

131. Bader, R.F., *Atoms in Molecules -A Quantum Theory*. 1990, New York: Oxford university Press.

132. Altermatt, D. and I.D. Brown, *The automatic searching for chemical bonds in inorganic crystal structures.* Acta Crystallographica Section B, 1985. **41**(4): p. 240-244.

133. Lufaso, M.W. and P.M. Woodward, *Using Bond Valences to Model the Structures of Ternary and Quaternary Oxides,* in *Bond Valences,* I.D. Brown and K.R. Poeppelmeier, Editors. 2014, Springer Berlin Heidelberg: Berlin, Heidelberg. p. 59-90.

134. Lufaso, M.W. and P.M. Woodward, *Prediction of the crystal structures of perovskites using the software program SPuDS.* Acta Crystallographica Section B, 2001. **57**(6): p. 725-738.

135. Brown, I.D., *Bond valences-a simple structural model for inorganic chemistry.* Chemical Society Reviews, 1978. **7**(3): p. 359-376.

136. White, R.L., *Review of Recent Work on the Magnetic and Spectroscopic Properties of the Rare-Earth Orthoferrites.* Journal of Applied Physics, 1969. **40**(3): p. 1061-1069.

137. White, R.M., R.J. Nemanich, and C. Herring, *Light scattering from magnetic excitations in orthoferrites.* Physical Review B, 1982. **25**(3): p. 1822-1836.

138. Herrmann, G.F., *Magnetic Resonances and Susceptibility in Orthoferrites.* Physical Review, 1964. **133**(5A): p. A1334-A1344.

139. Yamaguchi, T. and K. Tsushima, *Magnetic Symmetry of Rare-Earth Orthochromites and Orthoferrites.* Physical Review B, 1973. **8**(11): p. 5187-5198.

140. Maris, G., V. Volotchaev, and T.T.M. Palstra, *Effect of ionic size on the orbital ordering transition in* $RMnO_{3+\delta}$. New Journal of Physics, 2004. **6**(1): p. 153.

141. Qinzhuang, L., et al., *Structure and band gap tuning of transparent* $(Ba_{1-x}Sr_x)SnO_3$ *thin films epitaxially grown on MgO substrates.* EPL (Europhysics Letters), 2012. **98**(4): p. 47010.

142. Radaelli, P.G., et al., *Structural effects on the magnetic and transport properties of perovskite* $A_{1-x}A'_xMnO_3$ *(x=0.25, 0.30).* Physical Review B, 1997. **56**(13): p. 8265-8276.

143. Torrance, J.B., et al., *Systematic study of insulator-metal transitions in perovskites* $RNiO_3$ *(R=Pr,Nd,Sm,Eu) due to closing of charge-transfer gap.* Physical Review B, 1992. **45**(14): p. 8209-8212.

144. Zhao, Y., et al., *Thermal expansion and structural distortion of perovskite — data for* $NaMgF_3$ *perovskite. Part I.* Physics of the Earth and Planetary Interiors, 1993. **76**(1): p. 1-16.

145. Zhao, Y., et al., *Critical phenomena and phase transition of perovskite — data for* $NaMgF_3$ *perovskite. Part II.* Physics of the Earth and Planetary Interiors, 1993. **76**(1): p. 17-34.

146. Sinha, A.K., et al., *Angle Dispersive X-ray Diffraction Beamline on Indus-2 Synchrotron Radiation Source: Commissioning and First Results.* Journal of Physics: Conference Series, 2013. **425**(7): p. 072017.
147. Wiles, D.B. and R.A. Young, *A new computer program for Rietveld analysis of X-ray powder diffraction patterns.* Journal of Applied Crystallography, 1981. **14**(2): p. 149-151.
148. Momma, K. and F. Izumi, *VESTA 3 for three-dimensional visualization of crystal, volumetric and morphology data.* Journal of Applied Crystallography, 2011. **44**(6): p. 1272-1276.
149. Glazer, A., *The classification of tilted octahedra in perovskites.* Acta Crystallographica Section B, 1972. **28**(11): p. 3384-3392.
150. Late, R., et al., *Probing structural distortions in rare earth chromites using Indian synchrotron radiation source.* Indian Journal of Physics, 2016. **90**(12): p. 1347-1354.
151. Parida, S.C., S.K. Rakshit, and Z. Singh, *Heat capacities, order–disorder transitions, and thermodynamic properties of rare-earth orthoferrites and rare-earth iron garnets.* Journal of Solid State Chemistry, 2008. **181**(1): p. 101-121.
152. Zhou, Z., et al., *Hydrothermal synthesis and magnetic properties of multiferroic rare-earth orthoferrites.* Journal of Alloys and Compounds, 2014. **583**(Supplement C): p. 21-31.
153. Weckhuysen, B.M. and R.A. Schoonheydt, *Recent progress in diffuse reflectance spectroscopy of supported metal oxide catalysts.* Catalysis Today, 1999. **49**(4): p. 441-451.
154. Singh, P., et al., *Fe doped* $LaGaO_3$*: good white light emitters.* RSC Advances, 2016. **6**(102): p. 100230-100238.
155. Burke, K., *The ABC of DFT*. 2007, Department of Chemistry, University of California.
156. Zhang, R.-w., et al., *Room Temperature Quantum Spin Hall Insulator in Ethynyl-Derivative Functionalized Stanene Films.* Scientific Reports, 2016. **6**: p. 18879.
157. Neil W. Ashcroft, N.D.M., *Solid State Physics*. 1976: Cengage Learning US.

158. Brédas, J.L., *Relationship between band gap and bond length alternation in organic conjugated polymers.* The Journal of Chemical Physics, 1985. **82**(8): p. 3808-3811.
159. Yang, S. and M. Kertesz, *Bond Length Alternation and Energy Band Gap of Polyyne.* The Journal of Physical Chemistry A, 2006. **110**(31): p. 9771-9774.
160. Ouyang, G., C.Q. Sun, and W.G. Zhu, *Atomistic Origin and Pressure Dependence of Band Gap Variation in Semiconductor Nanocrystals.* The Journal of Physical Chemistry C, 2009. **113**(22): p. 9516-9519.
161. Miglio, A., et al., *Local Bonding Influence on the Band Edge and Band Gap Formation in Quaternary Chalcopyrites.* Advanced Science, 2017. **4**(9).
162. Wei, S.-H. and A. Zunger, *Predicted band-gap pressure coefficients of all diamond and zinc-blende semiconductors: Chemical trends.* Physical Review B, 1999. **60**(8): p. 5404-5411.
163. Yang, L., et al., *Band-gap change of carbon nanotubes: Effect of small uniaxial and torsional strain.* Physical Review B, 1999. **60**(19): p. 13874-13878.
164. Singh, S.D., et al., *Determination of the optical gap bowing parameter for ternary* $Ni_{1-x}Zn_xO$ *cubic rocksalt solid solutions.* Dalton Transactions, 2015. **44**(33): p. 14793-14798.
165. Mishra, V., et al., *Electronic and optical properties of* $BaTiO_3$ *across tetragonal to cubic phase transition: An experimental and theoretical investigation.* Journal of Applied Physics, 2017. **122**(6): p. 065105.
166. Kumar, A., et al., *Strain control of Urbach energy in Cr-doped* $PrFeO_3$*.* Applied Physics A, 2017. **123**(9): p. 576.
167. Butler, M.A., D.S. Ginley, and M. Eibschutz, *Photoelectrolysis with* $YFeO_3$ *electrodes.* Journal of Applied Physics, 1977. **48**(7): p. 3070-3072.
168. Shen, T., et al., *Theoretical investigation of magnetic, electronic and optical properties of orthorhombic* $YFeO_3$*: A first-principle*

study. Materials Science in Semiconductor Processing, 2015. **34**(Supplement C): p. 114-120.

169. Mark, D.S., et al., *Band structure and optical transitions in LaFeO 3 : theory and experiment.* Journal of Physics: Condensed Matter, 2014. **26**(50): p. 505502.
170. Holinsworth, B.S., et al., *Direct band gaps in multiferroic h-LuFeO3.* Applied Physics Letters, 2015. **106**(8): p. 082902.
171. Jaffe, J.E. and A. Zunger, *Theory of the band-gap anomaly in* ABC_2 *chalcopyrite semiconductors.* Physical Review B, 1984. **29**(4): p. 1882-1906.
172. Chien, J.C.W., F.E. Karasz, and K. Shimamura, *An estimate of bond length alternation in trans-polyacetylene.* Die Makromolekulare Chemie, Rapid Communications, 1982. **3**(10): p. 655-659.
173. Brisset, H., et al., *Bandgap control through reduction of bond length alternation in bridged poly(diethienylethylene)s.* Chemical Communications, 1997(6): p. 569-570.
174. Shen, T., et al., *Theoretical investigation of magnetic, electronic and optical properties of orthorhombic YFeO3: A first-principle study.* Materials Science in Semiconductor Processing, 2015. **34**: p. 114-120.
175. Archna, S., et al., *Origin of step-like behavior in the Co/Si system.* Journal of Physics: Condensed Matter, 2011. **23**(24): p. 246004.
176. Georgiev, D.G., K.A. Krezhov, and V.V. Nietz, *Weak antiferromagnetism in YFeO3 and HoFeO3.* Solid State Communications, 1995. **96**(8): p. 535-537.
177. Hahn, S.E., et al., *Inelastic neutron scattering studies of* $YFeO_3$*.* Physical Review B, 2014. **89**(1): p. 014420.
178. Zahi, S., A.R. Daud, and M. Hashim, *A comparative study of nickel–zinc ferrites by sol–gel route and solid-state reaction.* Materials Chemistry and Physics, 2007. **106**(2): p. 452-456.
179. Wang, J.A., et al., *Quantitative Determination of Titanium Lattice Defects and Solid-State Reaction Mechanism in Iron-Doped TiO2*

Photocatalysts. The Journal of Physical Chemistry B, 2001. **105**(40): p. 9692-9698.

180. Fita, I.M., et al., *Evolution of ferromagnetic order in* $LaMnO_{3.05}$ *single crystals: Common origin of both pressure and self-doping effects.* Physical Review B, 2003. **68**(1): p. 014436.
181. Markovich, V., et al., *Vacancies at Mn-sites in* $LaMn_{1-x}O_3$ *manganites: Interplay between ferromagnetic interactions and hydrostatic pressure.* Journal of Applied Physics, 2004. **95**(11): p. 7112-7114.
182. Streetman, B.G. and S. Banerjee, *Solid State Electronic Devices*. 2006: Pearson Prentice Hall.
183. Vidyasagar, R., et al., *Giant Zeeman shifts in the optical transitions of yttrium iron garnet thin films.* Applied Physics Letters, 2016. **109**(12): p. 122402.
184. Derras, M. and N. Hamdad, *New approach for the spin effect on the ground state properties of the cubic and hexagonal YFeO3 perovskite oxide: GGA+U based on the DFT+U description.* Results in Physics, 2013. **3**: p. 61-69.
185. Yuan, X.-p., et al., *Structure and magnetic properties of* $Y_{1-x}Lu_xFeO3$ *(*$0 \le x \le 1$*) ceramics.* Journal of Applied Physics, 2012. **111**(5): p. 053911.
186. Jin, Z., et al., *Single-pulse terahertz coherent control of spin resonance in the canted antiferromagnet* $YFeO_3$*, mediated by dielectric anisotropy.* Physical Review B, 2013. **87**(9): p. 094422.
187. Lütgemeier, H., H.G. Bohn, and M. Brajczewska, *NMR observation of the spin structure and field induced spin reorientation in YFeO3.* Journal of Magnetism and Magnetic Materials, 1980. **21**(3): p. 289-296.
188. Kumar, M., et al., *Barium disilicide as a promising thin-film photovoltaic absorber: structural, electronic, and defect properties.* Journal of Materials Chemistry A, 2017. **5**(48): p. 25293-25302.
189. Muhammad Alay-e-Abbas, S., S. Nazir, and A. Shaukat, *Formation energies and electronic structure of intrinsic vacancy*

defects and oxygen vacancy clustering in BaZrO3. Physical Chemistry Chemical Physics, 2016. **18**(34): p. 23737-23745.

190. Vikash, M., et al., *Effect of electron irradiation on the optical properties of SrTiO3: An experimental and theoretical investigations.* Materials Research Express, 2018.
191. Rai, H.M., et al., *Room-Temperature Magneto-dielectric Effect in* $LaGa_{0.7}Fe_{0.3}O_{3+\gamma}$*; Origin and Impact of Excess Oxygen.* Inorganic Chemistry, 2017. **56**(7): p. 3809-3819.
192. Eibschütz, M., S. Shtrikman, and D. Treves, *Mossbauer Studies of Fe57 in Orthoferrites.* Physical Review, 1967. **156**(2): p. 562-577.
193. Paudel, T.R., S.S. Jaswal, and E.Y. Tsymbal, *Intrinsic defects in multiferroic* $BiFeO_3$ *and their effect on magnetism.* Physical Review B, 2012. **85**(10): p. 104409.
194. Zener, C., *Interaction between the d-Shells in the Transition Metals. II. Ferromagnetic Compounds of Manganese with Perovskite Structure.* Physical Review, 1951. **82**(3): p. 403-405.
195. Goodenough, J.B., *Theory of the Role of Covalence in the Perovskite-Type Manganites [La, M(II)]*MnO_3*.* Physical Review, 1955. **100**(2): p. 564-573.
196. Kanamori, J., *Superexchange interaction and symmetry properties of electron orbitals.* Journal of Physics and Chemistry of Solids, 1959. **10**(2): p. 87-98.
197. Braun, A., et al., *Pre-edges in oxygen (1s) x-ray absorption spectra: A spectral indicator for electron hole depletion and transport blocking in iron perovskites.* Applied Physics Letters, 2009. **94**(20): p. 202102.
198. Braun, A., et al., *Electronic Origin of Conductivity Changes and Isothermal Expansion of Ta- and Ti-Substituted* $La_{1/2}Sr_{1/2}$*Fe-Oxide in Oxidative and Reducing Atmosphere.* Chemistry of Materials, 2012. **24**(8): p. 1529-1535.
199. Karvonen, L., et al., *O-K and Co-L XANES Study on Oxygen Intercalation in Perovskite* $SrCoO_{3-\delta}$*.* Chemistry of Materials, 2010. **22**(1): p. 70-76.

200. Chen, W.-T., et al., *Ligand-hole localization in oxides with unusual valence Fe.* Scientific Reports, 2012. **2**: p. 449.

201. Singh, S.D., et al., *Determination of the optical gap bowing parameter for ternary Ni1−xZnxO cubic rocksalt solid solutions.* Dalton Transactions, 2015. **44**(33): p. 14793-14798.

202. Wang, W., et al., *Crystal field splitting and optical bandgap of hexagonal LuFeO3 films.* Applied Physics Letters, 2012. **101**(24): p. 241907.

203. Warshi, M.K., et al., *Structural, optical and electronic properties of RFeO3.* Ceramics International, 2018. **44**(7): p. 8344-8349.

204. Ambrosch-Draxl, C. and J.O. Sofo, *Linear optical properties of solids within the full-potential linearized augmented planewave method.* Computer Physics Communications, 2006. **175**(1): p. 1-14.

205. Sagdeo, P.R., S. Anwar, and N.P. Lalla, *Powder X-ray diffraction and Rietveld analysis of La1−xCaxMnO3(0<X<1).* Powder Diffraction, 2012. **21**(1): p. 40-44.

206. Pisarev, R.V., et al., *Charge transfer transitions in multiferroic ${\text{BiFeO}}_{3}$ and related ferrite insulators.* Physical Review B, 2009. **79**(23): p. 235128.

207. Gupta, S., et al., *Temperature dependent Raman scattering and electronic transitions in rare earth SmFeO3.* Ceramics International, 2018. **44**(4): p. 4198-4203.

208. Hiraoka, N., et al., *Charge transfer and dd excitations in transition metal oxides.* The European Physical Journal B, 2009. **70**(2): p. 157-162.

209. Malakhovskii, A.V., et al., *Nature of optical properties of GdFe3(BO3)4 and GdFe2.1Ga0.9(BO3)4 crystals and other 3d5 antiferromagnets.* The European Physical Journal B, 2012. **85**(2): p. 80.

210. Huang, Z.J., et al., *Coupling between the ferroelectric and antiferromagnetic orders in ${\mathrm{YMnO}}_{3}$.* Physical Review B, 1997. **56**(5): p. 2623-2626.

211. Iwata, N. and K. Kohn, *Dielectric Anomalies at Magnetic Transitions of Hexagonal Rare Earth Manganese Oxides RMnO 3.* Journal of the Physical Society of Japan, 1998. **67**(9): p. 3318-3319.
212. Fiebig, M., et al., *Observation of coupled magnetic and electric domains.* Nature, 2002. **419**: p. 818.
213. Wang, J., et al., *Epitaxial BiFeO₃ Multiferroic Thin Film Heterostructures.* Science, 2003. **299**(5613): p. 1719-1722.
214. Eerenstein, W., N.D. Mathur, and J.F. Scott, *Multiferroic and magnetoelectric materials.* Nature, 2006. **442**: p. 759.
215. Hemberger, J., et al., *Relaxor ferroelectricity and colossal magnetocapacitive coupling in ferromagnetic CdCr2S4.* Nature, 2005. **434**: p. 364.
216. Catalan, G., *Magnetocapacitance without magnetoelectric coupling.* Applied Physics Letters, 2006. **88**(10): p. 102902.
217. Ma, J., et al., *Recent Progress in Multiferroic Magnetoelectric Composites: from Bulk to Thin Films.* Advanced Materials, 2011. **23**(9): p. 1062-1087.
218. Eiichi, H., H. Katsumi, and T. Yukito, *Clamping of ferroelectric and antiferromagnetic order parameters of YMnO 3.* Journal of Physics: Condensed Matter, 2003. **15**(3): p. L103.
219. Khomskii, D.I., *Multiferroics: Different ways to combine magnetism and ferroelectricity*. Journal of Magnetism and Magnetic Materials, 2006. **306**(1): p. 1-8.
220. Wu, H., et al., *Magnetic and magnetodielectric properties of Y3−xLaxFe5O12 ceramics.* Journal of Applied Physics, 2015. **117**(14): p. 144101.
221. Hur, N., et al., *Low-field magnetodielectric effect in terbium iron garnets.* Applied Physics Letters, 2005. **87**(4): p. 042901.
222. Jang, H.M., et al., *Magnetoelectric coupling susceptibility from magnetodielectric effect.* Applied Physics Letters, 2008. **93**(25): p. 252904.

223. Pradhan, D.K., et al., *Studies on magnetoelectric coupling in PFN-NZFO composite at room temperature.* Journal of Applied Physics, 2014. **115**(19): p. 194105.
224. Hill, N.A., *Why Are There so Few Magnetic Ferroelectrics?* The Journal of Physical Chemistry B, 2000. **104**(29): p. 6694-6709.
225. Schmid, H., *Guest editorial.* Ferroelectrics, 1994. **162**(1): p. xix-xxv.
226. Wood, V.E. and A. Austin, *Possible applications for magnetoelectric materials.* Int. J. Magn, 1974. **5**(4): p. 303-315.
227. Ortega, N., et al., *Multifunctional magnetoelectric materials for device applications.* Journal of Physics: Condensed Matter, 2015. **27**(50): p. 504002.
228. Wang, K.F., J.M. Liu, and Z.F. Ren, *Multiferroicity: the coupling between magnetic and polarization orders.* Advances in Physics, 2009. **58**(4): p. 321-448.